

Transport geometry of the restricted three-body problem

Joshua T. Fitzgerald

Dissertation submitted to the Faculty of the
Virginia Polytechnic Institute and State University
in partial fulfillment of the requirements for the degree of

Doctor of Philosophy
in
Engineering Mechanics

Shane D. Ross, Chair

Jonathan T. Black

Stefano Campagnola

John P. Domann

Kevin K. Schroeder

April 28, 2023

Blacksburg, Virginia

Keywords: Three-body problem, Phase space transit, Astrodynamics, Invariant manifolds

Copyright 2023, Joshua T. Fitzgerald

Transport geometry of the restricted three-body problem

Joshua T. Fitzgerald

(ABSTRACT)

This dissertation expands across three topics the geometric theory of phase space transit in the circular restricted three-body problem (CR3BP) and its generalizations. The first topic generalizes the low energy transport theory that relies on linearizing the Lagrange points in the CR3BP to time-periodic perturbations of the CR3BP, such as the bicircular problem (BCP) and the elliptic restricted three-body problem (ER3BP). The Lagrange points are no longer invariant under perturbation and are replaced by periodic orbits, which we call Lagrange periodic orbits. Calculating the monodromy matrix of the Lagrange periodic orbit and transforming into eigenbasis coordinates reveals that the transport geometry is a discrete analogue of the continuous transport geometry in the unperturbed problem. The second topic extends the theory of low energy phase space transit in periodically perturbed models using a nonlinear analysis of the geometry. This nonlinear analysis relies on calculating the monodromy tensors, which generalize monodromy matrices in order to encode higher order behavior, about the Lagrange periodic orbit. A nonlinear approximate map can be obtained which can be used to iterate initial conditions within the linear eigenbasis, providing a computationally efficient means of distinguishing transit and nontransit orbits that improves upon the predictions of the linear framework. The third topic demonstrates that the recently-discovered “arches of chaos” that stretch through the solar system, causing substantial phase space divergence for high energy particles, may be identified with the stable and unstable manifolds to the singularities of the CR3BP. We also study the arches in terms of particle

orbital elements and demonstrate that the arches correspond to gravity assists in the two-body limit.

Transport geometry of the restricted three-body problem

Joshua T. Fitzgerald

(GENERAL AUDIENCE ABSTRACT)

Suppose that we have a spacecraft and we want to model its motion under gravity. Depending upon what trade-offs we are willing to make between accuracy and complexity, we have several options at our disposal. For example, the restricted three-body problem (R3BP) and its generalizations prove useful in many real-world situations and are rich in theoretical power despite seeming mathematically simple. The simplest restricted three-body problem is the circular restricted three-body problem (CR3BP). In the CR3BP, two masses (like a star and a planet or a planet and a moon) orbit their common center of gravity in circular orbits, while a much smaller body (like a spacecraft) moves freely, influenced by the gravitational fields that the two masses create. If we add in an extra force that acts on the spacecraft in a periodic, cycling way, the regular CR3BP becomes a periodically-perturbed CR3BP. Examples of periodically-perturbed CR3BP's include the bicircular problem (BCP), which adds in a third mass that appears to orbit the center of the system from a distance, and the elliptic restricted three-body problem (ER3BP), which allows the two masses to orbit more realistically as ellipses rather than circles. The purpose of this dissertation is to determine how to select trajectories that move spacecraft between places of interest in restricted three-body models. We generalize existing theories of CR3BP spacecraft motion to periodically-perturbed CR3BP's in the first two topics, and then we investigate some new areas of research in the unperturbed CR3BP in the third topic. We utilize numerical computations and mathematical methods to perform these analyses.

Dedication

To Dee Sizemore, who taught me how to love mathematics.

Acknowledgments

Many people contributed to the actualization of this dissertation.

To our collaborators and colleagues: Thank you for rendering assistance in theoretical and computational matters. It enabled this research.

To my dissertation committee: Thank you for investing your valuable time in order to serve in this capacity.

To Shane Ross: you have been an exemplary advisor, and I feel honored to have been your student. You have taught me not only about technical matters but also about the proper mindset of a scholar. I feel considerable gratitude for your mentorship.

To the Ross Dynamics Lab: I will miss you all very much. I will recall our days together with the utmost happiness.

To Greensboro College: Thank you for taking a risk and admitting me. It is unequivocally true that “my thoughts of thee will always be among my fondest memories.”

To my friends: Thank you all so much for the emotional support over these last four years. You don’t know how much you mean to me.

To my parents: I will always be grateful for your unconditional love. I love you.

Contents

List of Figures	xiii
1 Introduction	1
1.1 Review of the transit geometry of the circular restricted three-body problem	2
1.1.1 The circular restricted three-body problem	2
1.1.2 Energy cases and realms	7
1.1.3 The Lagrange points	11
1.1.4 Linearization about the Lagrange points	13
1.1.5 Geometry of the linearized dynamics in the eigenbasis	17
1.1.6 Geometry of the linearized dynamics in standard coordinates	22
1.2 Selected historical applications of manifold-based transit geometry	24
1.3 The periodically-perturbed circular restricted three-body problem	27
1.4 Review of recent developments in the restricted three-body literature	29
1.5 Research overview	32
2 Geometry of low-energy transit orbits in the periodically-perturbed restricted three-body problem	34
2.1 Introduction	35

2.2	Classification of orbits in the circular restricted three-body problem	38
2.2.1	Equations of motion	38
2.2.2	The Lagrange points	39
2.2.3	The Hill's region and the Hamiltonian energy	40
2.2.4	Linearization about L_1 and L_2	42
2.2.5	Geometry of the linearized equilibrium region	42
2.3	Lagrange manifolds in periodically-perturbed systems	44
2.3.1	Periodically-perturbed systems	44
2.3.2	Flow maps	45
2.3.3	State transition and monodromy matrices	46
2.3.4	Lagrange periodic orbits replace Lagrange points	46
2.4	Linear 4D symplectic map near elliptic-hyperbolic point	47
2.4.1	Definitions	47
2.4.2	The effective quadratic Hamiltonian	48
2.4.3	Geometry of the linear map	49
2.4.4	Topology of the equilibrium region of the map	50
2.4.5	Connection with Lagrange periodic orbits	53
2.5	Transit orbits in the bicircular problem	53
2.5.1	Equations of motion of the BCP	53
2.5.2	The instantaneous Lagrange points	54

2.5.3	Dynamics near the Sun-perturbed Earth-Moon BCP L_1 Lagrange periodic orbit	56
2.6	Transit orbits in elliptic restricted three-body problem	59
2.6.1	Equations of motion in the ER3BP	59
2.6.2	Dynamics near the Earth-Moon ER3BP L_1 Lagrange periodic orbit	60
2.7	Discussion and conclusion	62
3	State transition tensors and the nonlinear transit geometry of the periodically-perturbed restricted three-body problem	66
3.1	Introduction	67
3.2	Periodically-perturbed systems and state transition tensors	69
3.2.1	Periodically-perturbed systems	69
3.2.2	Flow maps	69
3.2.3	State transition tensors	70
3.3	Linear transit geometry of the periodically perturbed three-body problem	71
3.3.1	Hierarchy of models	71
3.3.2	The Lagrange periodic orbits	75
3.3.3	Geometry of the linear map	77
3.4	Quadratic transit geometry of the periodically perturbed three-body problem	81
3.4.1	The quadratic map	81
3.4.2	Notes regarding the effective Hamiltonian	81

3.4.3	The nonlinear transit / nontransit prediction method	82
3.5	Transit orbits in the bicircular problem	86
3.6	Transit orbits in the elliptic restricted three-body problem	88
3.7	Discussion and Conclusion	89
4	Geometry Associated with the CR3BP Singularities	91
4.1	Introduction	91
4.2	Introduction to the Arches of Chaos	92
4.2.1	The Fast Lyapunov Indicator	92
4.2.2	The Arches of Chaos	93
4.3	The regularization of the circular restricted three-body problem	95
4.3.1	The CR3BP	95
4.3.2	The Lagrange Points and High Energies	96
4.3.3	Introduction to the Levi-Civita regularization	98
4.3.4	The Levi-Civita regularization and numerical integration	100
4.4	Preliminary Numerical Experiments on the Stable and Unstable Manifolds to the Secondary Singularity	101
4.4.1	Global geometry of the stable and unstable manifolds	101
4.4.2	Quantifying the consequences of close encounters	103
4.4.3	Close encounters and patched conics	106
4.5	Numerically Linking the Arches of Chaos and the Stable and Unstable Manifolds	111

4.6	Discussion and Conclusion	111
5	Assorted Results	115
5.1	Attribution	115
5.2	CMDS	115
5.2.1	Introduction	115
5.2.2	Architecture	116
5.2.3	Functionality	117
5.2.4	Examples	119
5.2.5	Dependencies and compatibilities	120
5.3	Computing quadratic Hamiltonians for linear symplectic maps	120
5.3.1	Introduction	120
5.3.2	Mathematical preliminaries	121
5.3.3	2D example of method	122
5.3.4	Application to the elliptic-hyperbolic map	124
6	Conclusions	127
6.1	Summary and discussion	127
6.2	Engineering applications	128
6.3	Future Work	129
	Appendices	147

Appendix A	GitHub repositories	148
Appendix B	Initial conditions	149
Appendix C	Proof of Proposition 2.1	150
Appendix D	Continuation visualization for the ER3BP L_1 Lagrange periodic orbit	152

List of Figures

1.1	A schematic of the inertial and rotating frames of the planar circular restricted three-body problem, viewed in the inertial frame.	3
1.2	A schematic of the PCR3BP viewed in the rotating frame.	4
1.3	The five energy cases plotted for $\mu = 0.3$. Black lines are zero-velocity curves. The gray regions comprise the forbidden realm. Figure edited from [3].	9
1.4	The locations of the five Lagrange points in the CR3BP for $\mu = 0.3$. Figure edited from [3].	12
1.5	The projection of the neck region \mathcal{R} onto the canonical planes. In the saddle projection, the dot at the center represents the Lagrange point and its center manifold, and the orange lines represent the stable (arrows pointing towards the origin) and unstable (arrows pointing away from the origin) manifolds. Blue trajectories enter and leave \mathcal{R} from the same bounding sphere, whereas red trajectories enter and leave \mathcal{R} from different bounding spheres. These two cases correspond to orbits which do not transit between the realms and orbits which do transit between the realms, respectively. Figure edited from [3].	20

1.6	The projection of the neck region \mathcal{R} onto position space. The dot at the center represents a Lagrange point, which is surrounded by the black Lyapunov orbit corresponding to the chosen energy. The orange trajectory is on the stable manifold to the Lyapunov orbit. The blue trajectories fail to transit, whereas the red trajectories transit. The gray triangles represent the wedges of velocity for which transit is possible at the chosen position space point. Figure edited from [3].	23
1.7	The CR3BP bifurcates to the BCP or the ER3BP, depending on the periodic perturbation introduced into the system.	27
2.1	Schematic illustrating how the Lagrange manifold bifurcates as astrodynamical models go from simplest and least accurate at the bottom, increasing in fidelity to the real ephemeris. The bifurcation discussed in this paper is the transition from the equilibrium point to the periodic orbit.	36
2.2	The models considered, viewed in the m_1 - m_2 barycentered average rotating frame.	39
2.3	(a) The Lagrange points of the CR3BP for $\mu = 0.3$. (b) The five cases of the energetically accessible regions (i.e., Hill's region) by CR3BP Hamiltonian energy.	41
2.4	The two canonical planes of the dynamics in the symplectic eigenbasis in the neighborhood of a collinear Lagrange point; orbits labeled T transit from one realm to another, while those labeled NT do not.	43

2.5	The two canonical planes of the dynamics under the mapping $\mathbf{x} \mapsto \Lambda\mathbf{x}$; the orbits here are discrete solutions of a map (represented as large dots in one of the transit curves) as compared to continuous orbits in Figure 2.4.	49
2.6	Construction of a hemisphere bounding the equilibrium region of the map, along an energy manifold of energy h : each point along the bounding line \overline{AB} in the saddle projection corresponds to the circle of initial conditions in the center projection of the same color, shrinking to a point at B.	51
2.7	The McGehee representation of the discrete dynamics in the equilibrium region of the map on a fixed energy shell is obtained by rotating this diagram one revolution about the ω axis. The red lines correspond to iterates of the transit conditions under the stroboscopic map P_0 ; the blue lines correspond to iterates of the non-transit conditions; the orange lines correspond to the stable and unstable manifolds under the quadratic Hamiltonian. The black point corresponds to an invariant circle of the map of energy h , analogous to a Lyapunov orbit of energy h in the unperturbed case.	52
2.8	The BCP Earth-Moon L_1 periodic orbit (black) compared with the path (in blue) traced by the instantaneous zero, or stagnation point, of the BCP vector field. The former is a trajectory; the latter is not. Both have doubly-looping structures over a single period of the perturbation, but at the resolution shown, even in the inset, only the periodic orbit's two loops are visible.	55

2.9	(a) Numerically determined initial conditions for transit and non-transit orbits found by looking in the q_1 - p_1 saddle canonical plane at initial phase $\theta = 0$. $\tilde{H}_2 = 10^{-6}$ and $c = 10^{-4}$. Compare with schematic shown in Figure 2.5. (b) The initial conditions integrated in the full equations of motion showing transit and non-transit behavior. Please refer to the online version of this article relating to color.	57
2.10	The spherical cap of transit orbits, Γ_T , is mapped forwards and backwards in the bicircular model and then projected into x - y - p_x space.	58
2.11	The ER3BP Earth-Moon L_1 periodic orbit (large, dark green) and the BCP L_1 periodic orbit (black) in the position space (average rotating frame, CR3BP coordinates). The ER3BP L_1 periodic orbit is singly-looping, not doubly-looping as in the BCP.	61
2.12	(a) Initial conditions for transit and non-transit orbits found by looking in the q_1 - p_1 saddle canonical plane in the symplectic eigenbasis. $\tilde{H}_2 = 10^{-8}$ and $c = 4 \times 10^{-5}$. (b) The initial conditions integrated backwards and forwards in the full equations of motion, as shown, starting at phase (mean anomaly) $\theta = 0$. (c) The initial conditions from part (a) integrated backwards and forwards in the full equations of motion for $\theta = \frac{\pi}{3}$. Note that the transit theory still holds at a different phase. (d) The integrated initial conditions for $\theta = \frac{2\pi}{3}$	62
3.1	Schematic of the sequence of Lagrange manifolds that “links” the transit structure of the CR3BP with the full ephemeris. As additional perturbation forces are added to the system, the dimension and topological complexity of the Lagrange manifold correspondingly increases.	68

3.2	The models considered. The reference frame in each model rotates at the same constant rate as m_1 and m_2 in the CR3BP and has its origin at their center of mass.	72
3.3	The ER3BP Earth-Moon L_1 periodic orbit (large, dark green) and the BCP Earth-Moon-Sun L_1 periodic orbit (black) projected into position space (CR3BP rotating coordinate frame). The BCP L_1 periodic orbit has a doubly looping structure (not shown) whereas the ER3BP L_1 periodic orbit has a singly looping structure.	76
3.4	The two canonical planes of the discrete dynamics governed by $\mathbf{x} \mapsto \mathbf{\Lambda}\mathbf{x}$; the orbits here are discrete points (the large dots) that when iterated under the map “jump” along the solution curves.	79
3.5	A flowchart representing the algorithm for using the quadratic map to approximate transit in the linear eigenbasis.	83
3.6	A schematic comparison of the expected geometries of the quadratic and linear stable and unstable manifolds, viewed in the linear eigenbasis. The stable and unstable manifolds predicted by the map of order i are denoted as $W_{(i)}^S(L_1)$ and $W_{(i)}^U(L_1)$, respectively. The circles on the quadratic stable manifold exemplify how, as in Figure 3.4, this picture is only valid at a fixed phase of the perturbation. Under the stroboscopic map, trajectories will return to the manifolds in a discrete, discontinuous fashion.	85

3.7	<p>(a) The fates of orbits in the Sun-perturbed Earth-Moon BCP predicted by iterating the forward-time quadratic map over a grid of 6,000 initial conditions and classifying them depending on the linear q_1-p_1 plane quadrant to which the iterate belongs. Blue points correspond to nontransit orbits, whereas red points correspond to transit orbits. The black lines correspond to the stable and unstable manifold, which were refined using bisection; the unstable manifold also possesses a slight curvature, but it is not visible due to the extreme inequality of the axes. $h = 10^{-13}$ and each initial condition is chosen so that $q_2 = p_2 > 0$. (b) The orbits from the $p_1 > 0$ halfplane of (a) integrated in standard coordinates and projected into position space. (c) The orbits from the $p_1 < 0$ halfplane of (a) integrated in standard coordinates and projected into position space.</p>	86
3.8	<p>(a) The transit/nontransit behavior of initial conditions in backwards time where $p_2 = q_2$. (b) The transit/nontransit behavior of initial conditions in forward time where $p_2 = -q_2$ instead of $p_2 = q_2$.</p>	87
3.9	<p>(a) The fates of orbits in the Earth-Moon ER3BP predicted by iterating the forward-time quadratic map over a grid of 6,000 initial conditions and classifying them. $h = 10^{-13}$ and each initial condition is chosen so that $q_2 = p_2 > 0$. (b) The orbits from the $p_1 < 0$ halfplane of (a) integrated in standard coordinates and projected into position space. (c) The transit/nontransit behavior of initial conditions in forward time where $p_2 = -q_2$ instead of $p_2 = q_2$.</p>	88

4.1	<p>FLI maps of a grid of initial conditions with varying semi-major axes a and eccentricities e reveal a complex series of arch-like structures, the arches of chaos, in the Sun-Jupiter restricted three-body problem. Regions with lighter colors correspond to higher values of the FLI and therefore to higher trajectory divergence, which suggests the presence of stable and unstable manifolds. q_j and Q_j are Jupiter's perihelion and aphelion lines, respectively, and $T_j = 3$ is a Jupiter Tisserand curve. $W_{L_1}^S$ and $W_{L_2}^S$ are the stable manifold curves of the Sun-Jupiter L_1 and L_2 points, respectively. Figure edited from Todorović, Wu, and Rosengren [74].</p>	94
4.2	<p>A schematic of the planar circular restricted three-body problem viewed in the rotating frame.</p>	95
4.3	<p>The Hamiltonian energy can be separated into five distinct intervals based on the topologies of the forbidden realm.</p>	97
4.4	<p>The x-y plane in standard coordinates maps to the half-plane in regularized coordinates.</p>	99
4.5	<p>A projection of the portion of the stable manifold with $E = -1.3$ onto x-y-p_x space. Integration has been truncated while the trajectories are still close to the singularity in order to make the depiction of the geometry clearer. For a rotating view of the stable and unstable manifolds, see the video attached in the supplemental files to this dissertation.</p>	102
4.6	<p>A projection of the portion of the stable manifold with $E = -1.3$ onto x-y-p_x space. Integration has been truncated much further from the singularity than in Figure 4.5.</p>	103

4.7 A schematic of the numerical experiment for examining how trajectories on either side of the stable manifold to the singularity move throughout phase space. The red and dark blue trajectories are generated at an initial radius r_{ce} but have $\dot{\theta} < 0$ and $\dot{\theta} > 0$, respectively. They reflect one choice of θ_{ce} , but a whole family of trajectories for different values of θ_{ce} must be generated in order to match + and - pairs along the detection radius r_d . We integrate forwards and backwards and then match those + and - trajectories whose final position in backwards time was nearest to each other; in the schematic, the red - trajectory has been matched with a light blue + trajectory, generated in the same way as the dark blue trajectory for a different value of θ_{ce} . Observe that the matched trajectories are on either side of a stable manifold trajectory, which is depicted in green. We then compare the pre-encounter, four-dimensional phase space distance d_{pre} with the post-encounter distance d_{post} for each matched pair, parameterizing by θ_{pre}^+ , the pre-encounter angle of the + trajectory (see Figure 4.8). 104

4.8 The chosen + and - trajectories have a very small initial separation pre-encounter, but post-encounter their separation significantly increases regardless of angle along the detection circle (in this case, we use θ_{pre}^+ , the pre-encounter angle of each + trajectory, as the angle for identifying and sorting matched pairs of + and - trajectories). 106

4.9 For all computations in this figure, trajectories were generated such that $r_d = 7r_h \approx 0.4774$ and $r_{ce} = 0.1R_{\mathcal{J}}$, where $R_{\mathcal{J}}$ is the radius of Jupiter in non-dimensionalized units. (a) A comparison of the Keplerian energies of the + and - trajectories as a function of the pre-encounter angle θ_{pre}^+ . K_{pre}^{\pm} denotes the pre-encounter Keplerian energies of the + and - trajectories, which approximately coincide. K_{post}^+ and K_{post}^- denote the post-encounter Keplerian energies of the + and - trajectories, respectively. The energy values of an example pair of matched + and - trajectories are highlighted. The + trajectory has negative Keplerian energy after the encounter, which predicts that it will be a bound elliptical orbit around m_1 ; the - trajectory has positive Keplerian energy after the encounter, which predicts that it will be an unbound hyperbolic orbit. (b) The highlighted pair of + and - trajectories integrated in the rotating frame, demonstrating the predicted divergence in their post-encounter fates. (c) A comparison of the argument of periapse values of the + and - trajectories as a function of the pre-encounter angle θ_{pre}^+ . ω_{pre}^{\pm} denotes the pre-encounter argument of perigee values of the + and - trajectories, which approximately coincide. ω_{post}^+ and ω_{post}^- denote the post-encounter argument of perigee values of the + and - trajectories, respectively. The values of the example trajectories are highlighted. (d) The highlighted pair of + and - trajectories integrated in the inertial frame. 107

4.10 A comparison of selected orbital elements of the families of + and - trajectories integrated in the full PCR3BP equations with orbital elements ascertained through patched conics propagation. Both r_d and r_{ce} are small enough that close agreement is seen with the Keplerian case. 108

4.11 Similar to Figure 4.10, but r_{ce} has been increased. 109

4.12	Similar to Figure 4.10, but r_d has been increased.	110
4.13	A comparison of the maximum errors between the three-body and patched conics orbital element curves. $n = r_d/r_h$. The error is computed with respect to the corresponding patched conics curve: for example, K_{pre} for K_{pre}^\pm and K_{post} for K_{post}^\pm . (a) The Keplerian energy errors. (b) The argument of perigee errors.	110
4.14	The intersection of an approximation of the stable manifold originally consisting of 40,000 trajectories with the arches of chaos section, viewed in semi-major axis/eccentricity space. Yellow crosses represent stable manifold trajectories, which have been superimposed onto a plot of the arches of chaos in the Sun-Jupiter-Spacecraft restricted three-body problem adapted from Todorović, Wu, and Rosengren [74]. The stable manifold closely shadows the arches even though only a small percentage of the trajectories intercept the section.	112
5.1	The structure of a context object <code>c</code> before it is modified by any other functions. Context objects store data as a series of nested structs, which are usually assigned terse names so that code that accesses context objects can be written more compactly. Blue boxes represent namespaces and green boxes represent properties. Additional namespaces and properties typically need to be added to the context object after creation.	116
5.2	The process by which CMDS derives symbolic equations of motion and other useful characteristics of the dynamics from expressions for the kinetic and potential energies. CMDS also supports deriving the equations of motion directly from the Hamiltonian.	118

D.1 A family of periodic orbits for different eccentricities emanating from the unperturbed L_1 point in the ER3BP. 153

Chapter 1

Introduction

Many spacecraft missions have relied on trajectories designed using the patched conics framework, which assumes that only one mass at a time gravitationally influences a spacecraft. Famous examples include the Voyager probes and the New Horizons mission to Pluto [1, 2]. The patched conics approach is useful for high-energy, short-timescale missions. However, fuel is expensive, and considering gravitation from more than one mass at a time enables the design of more efficient missions whose trajectories more accurately account for real-world perturbations.

A simple way to introduce additional masses is via the restricted three-body problem (R3BP), in which two bodies gravitate and a third body, like a spacecraft or small asteroid, has negligible mass and gravitation. The simplest restricted three-body problem is the circular restricted three-body problem (CR3BP), in which the two masses orbit their center of gravity in circles. In a rotating reference frame that rotates with the two masses, the CR3BP equations of motion are autonomous, and so the system has been the subject of much analysis, particularly into its periodic orbits and phase space transit behavior (for an example of a comprehensive guide to the topic, see [3]).

The CR3BP, while a very useful dynamical model, makes many simplifying assumptions, and so introducing perturbations into the CR3BP is a means of increasing its fidelity. For example, periodically-perturbed circular restricted three-body problems add in a single, time-periodic force to the standard equations of motion. Examples of periodically-perturbed

problems include the bicircular problem (BCP), in which an additional, distant mass circles the origin in the rotating frame, and the elliptic restricted three-body problem (ER3BP), in which the two masses orbit each other in ellipses.

The purpose of this dissertation is to advance understanding of the geometric structure of dynamical transport in unperturbed and perturbed CR3BP models. Knowledge of the manifold structures that foliate phase space is necessary for constructing mathematically rigorous multi-body trajectory design methods, which could prove essential as humans advance further into cislunar space in coming decades.

1.1 Review of the transit geometry of the circular restricted three-body problem

In this section, we review the classical theory of low-energy dynamical transport in the circular restricted three-body problem, which serves as the theoretical foundation for the remainder of this dissertation.

1.1.1 The circular restricted three-body problem

The circular restricted three-body problem models the motion of a body m_3 under the gravitational influence of two point masses, m_1 and m_2 . We take $m_1 > m_2$, and so we call m_1 the *primary* and m_2 the *secondary*, although together the two masses are called the *primaries* [4, 3]. The primary and secondary are also sometimes called the *larger primary* and *smaller primary*, respectively [5]. m_1 and m_2 orbit their barycenter in circular orbits, which implies that the distance d between them is fixed. m_3 is free to move throughout the phase space under the primaries' gravitational fields, but it does not influence their motion

because its mass is assumed negligible. We assume for the remainder of this dissertation that m_3 only moves within the plane of motion of m_1 and m_2 , which corresponds to the *planar* circular restricted three-body problem (PCR3BP). The generalization to the spatial case is straightforward.

The system is straightforward to non-dimensionalize. Let the unit of mass be $m_1 + m_2$ and let the unit of length be d . Let the unit of time be the orbital period of the primaries divided by 2π . In these units—which we call non-dimensional or *non-dimensionalized units*, the gravitational constant becomes $G = 1$, and the only parameter of the system becomes the *mass parameter*

$$\mu = \frac{m_1}{m_1 + m_2}. \quad (1.1)$$

Because we assume $m_1 > m_2$, $\mu \in [0, \frac{1}{2}]$.

It is natural to view this problem within an inertial frame $\mathcal{I} = \{\hat{X}, \hat{Y}, \hat{X} \times \hat{Y}, O\}$, where the O is the barycenter of the primaries and \hat{X} and \hat{Y} are vectors within the primaries' orbital plane (see Figure 1.1). However, the dynamics are dramatically simpler when viewed in the *rotating* or *synodic frame* $\mathcal{R} = \{\hat{x}, \hat{y}, \hat{x} \times \hat{y}, O\}$, where \hat{x} points from O towards m_2 and \hat{y} is perpendicular to \hat{x} and points in the direction of motion of m_2 [4, 3]. The \mathcal{R} frame rotates

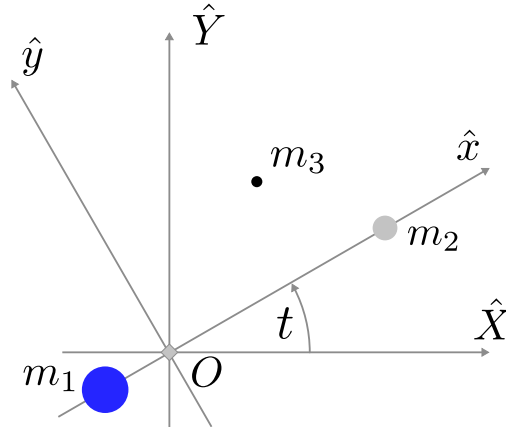


Figure 1.1: A schematic of the inertial and rotating frames of the planar circular restricted three-body problem, viewed in the inertial frame.

with m_1 and m_2 at the constant rate of their orbital motion, which is equal to unity in the non-dimensionalized units (see Figure 4.2).

We define t so that \mathcal{R} and \mathcal{I} coincide at $t = 0$. Denote a position vector by

$$\mathbf{r} = X\hat{X} + Y\hat{Y} = x\hat{x} + y\hat{y} \quad (1.2)$$

so that the inertial frame velocity coordinates are \dot{X} and \dot{Y} and the rotating frame velocity coordinates are \dot{x} and \dot{y} .

Then

$$\begin{bmatrix} X \\ Y \end{bmatrix} = A(t) \begin{bmatrix} x \\ y \end{bmatrix} \quad (1.3)$$

and (as can be shown through differentiation)

$$\begin{bmatrix} \dot{X} \\ \dot{Y} \end{bmatrix} = A(t) \begin{bmatrix} \dot{x} - y \\ \dot{y} + x \end{bmatrix} \quad (1.4)$$

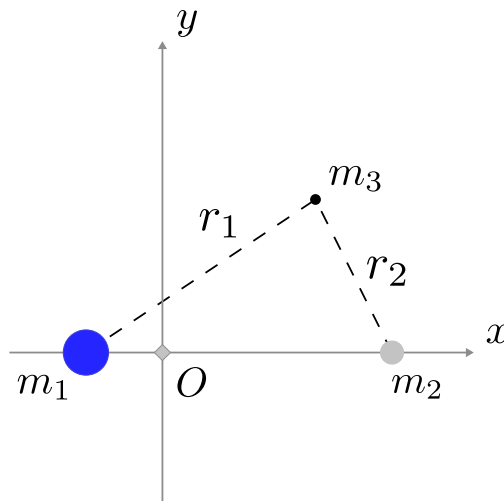


Figure 1.2: A schematic of the PCR3BP viewed in the rotating frame.

for

$$A(t) = \begin{bmatrix} \cos(t) & -\sin(t) \\ \sin(t) & \cos(t) \end{bmatrix} \quad (1.5)$$

give the transformation between rotating and inertial coordinates.

We observe the convention, standard in most modern works [3, 6, 7, 8], that the rotating frame positions of m_1 and m_2 are fixed at $(-\mu, 0)$, and $(1 - \mu, 0)$, which renders the system autonomous when written with respect to \mathcal{R} . An alternate convention, also seen in the literature but especially common among Catalan astrodynamists, positions m_1 at $(\mu, 0)$ and m_2 at $(\mu - 1, 0)$ [9, 10, 4].

The gravitational potential with respect to the rotating coordinate system (and also the inertial coordinate system) is

$$U(x, y) = -\frac{\mu_1}{r_1} - \frac{\mu_2}{r_2} - \frac{1}{2}\mu_1\mu_2 \quad (1.6)$$

where $\mu_1 = 1 - \mu$ and $\mu_2 = \mu$ are the non-dimensional masses of m_1 and m_2 , respectively, and

$$\begin{aligned} r_1 &= \sqrt{(x + \mu)^2 + y^2}, \\ r_2 &= \sqrt{(x - 1 + \mu)^2 + y^2} \end{aligned} \quad (1.7)$$

are the distances from m_1 and m_2 , respectively, to m_3 . The constant $-\frac{1}{2}\mu_1\mu_2$ term is customary and does not influence the derivation of the equations of motion [11]. Note that some works written from a celestial mechanics perspective instead define U to be positive (see, for instance, [12]).

The kinetic energy of m_3 is

$$T(\dot{X}, \dot{Y}) = \frac{1}{2} (\dot{X}^2 + \dot{Y}^2). \quad (1.8)$$

Substituting in (1.4) rewrites the kinetic energy in terms of the rotating frame variables:

$$T(\dot{x}, \dot{y}) = \frac{1}{2} ((\dot{x} - y)^2 + (\dot{y} + x)^2). \quad (1.9)$$

The Lagrangian of the system is

$$L(x, y, \dot{x}, \dot{y}) = T - U \quad (1.10)$$

which can be converted to the Hamiltonian

$$\begin{aligned} H(x, y, p_x, p_y) &= xp_x + yp_y - L(x, y, \dot{x}, \dot{y}) \\ &= \frac{1}{2} ((p_x + y)^2 + (p_y - x)^2) + \bar{U}(x, y) \end{aligned} \quad (1.11)$$

via the Legendre transformation

$$\begin{aligned} p_x &= \frac{\partial L}{\partial \dot{x}} = \dot{x} - y \\ p_y &= \frac{\partial L}{\partial \dot{y}} = \dot{y} + x \end{aligned} \quad (1.12)$$

where p_x and p_y are the conjugate momentum variables to x and y , respectively, and

$$\bar{U}(x, y) = -\frac{1}{2}(x^2 + y^2) + U(x, y) \quad (1.13)$$

is the *effective potential*. The Hamiltonian function can also be written in velocity coordinates

as

$$H(x, y, \dot{x}, \dot{y}) = \frac{1}{2} (\dot{x}^2 + \dot{y}^2) + \bar{U}(x, y). \quad (1.14)$$

The Hamiltonian equations of motion—the formulation of the equations of motion that we use throughout this dissertation—are given by

$$\begin{aligned}
 \dot{x} &= \frac{\partial H}{\partial p_x} = p_x + y, \\
 \dot{y} &= \frac{\partial H}{\partial p_y} = p_y - x, \\
 \dot{p}_x &= -\frac{\partial H}{\partial x} = p_y - x - \frac{\partial \bar{U}}{\partial x}, \\
 \dot{p}_y &= -\frac{\partial H}{\partial y} = -p_x - y - \frac{\partial \bar{U}}{\partial y}.
 \end{aligned} \tag{1.15}$$

Thus, the dynamics occur in a four-dimensional *phase space*, specifically the manifold

$$\begin{aligned}
 \mathcal{M} &= \mathbb{R}^4 - \{(n - \mu, 0, p_x, p_y) \mid n \in \{0, 1\}, p_x, p_y \in \mathbb{R}\} \\
 &= \mathbb{R}^4 - \{(n - \mu, 0, x, y) \mid n \in \{0, 1\}, \dot{x}, \dot{y} \in \mathbb{R}\}
 \end{aligned} \tag{1.16}$$

. This manifold contains all of four-dimensional Euclidean space except the *singularities at the primaries*, which result from the divergence of the Hamiltonian function as $r_1 \rightarrow 0$ or $r_2 \rightarrow 0$ and which correspond to how the primaries are modeled as point masses. It is often useful to write $\mathcal{M} = \mathcal{Q} \times \mathcal{P}$ where \mathcal{Q} is a *position space* with coordinates x and y and where \mathcal{P} is a *momentum space* with coordinates p_x and p_y .

1.1.2 Energy cases and realms

One benefit of using the Hamiltonian formulation is that trajectories conserve the Hamiltonian function H , which is a representation of the energy of the system. In fact, H is the only independent constant of motion of the system, so the PCR3BP is non-integrable. For the remainder of this dissertation, we will discuss the energy of m_3 in terms of H , but it is also common to use the *Jacobi integral* $C = -2H$, particularly among dynamical astronomers

and celestial mechanists [3]. Also, because the Legendre transformation makes conversion between position and momentum coordinates very easy, we sometimes write the Hamiltonian function using the coordinate system-agnostic notation $H(\mathbf{x})$ for $\mathbf{x} \in \mathcal{M}$.

Analyzing the structure of H is a critical starting point for understanding the global geometry of motion in the PCR3BP. Fix $H = E \in \mathbb{R}$. Then we may define a codimension-one submanifold

$$\mathcal{M}_E = \{\mathbf{x} \in \mathcal{M} \mid H(\mathbf{x}) = E\}, \quad (1.17)$$

which is called the *energy surface* [3].

The projection of \mathcal{M}_E onto \mathcal{Q} is the manifold-with-boundary

$$M_E = \{(x, y) \mid \bar{U}(x, y) \leq E\}, \quad (1.18)$$

which is sometimes called the *Hill's region* [3]. The boundary ∂M_E is called the *zero-velocity curve* because it corresponds to the case when $E = \bar{U}$, which by (1.14) implies that the velocity of m_3 is zero and also that $T(\dot{x}, \dot{y}) = 0$. Because $T(\dot{x}, \dot{y}) < 0$ is not permitted in a mechanical system, motion outside of the Hill's region is impossible at the chosen energy. The complement of M_E , in which $T(\dot{x}, \dot{y}) < 0$, is called the *forbidden realm*, which we notate by M'_E .

M_E can be loosely partitioned into the three *realms* of motion: the m_1 *realm*, which comprises the space surrounding m_1 ; the m_2 *realm*, which comprises the space surrounding m_2 ; and the *exterior realm*, which comprises the space beyond the forbidden realm that stretches out to infinity [3]. These general, energy-independent definitions are intentionally imprecise; as implied by the analysis below, it is easiest to define the boundaries of the realms when a specific energy has been selected.

Varying E induces a series of topological bifurcations in ∂M_E , and also M_E and M'_E , with important consequences for the global phase space geometry [3]. These bifurcations may be used to divide E into five different *energy cases*—energy intervals within which ∂M_E has the same topology (see Figure 1.3). Notice how ∂M_E is typically a manifold except at $E \in \{E_1, E_2, E_3\}$.

1. For $E < E_1$ (Case 1), $\partial M_E \cong S^1 \sqcup S^1 \sqcup S^1$. The particle cannot transit between any of the three realms, as they are all separated by M'_E .
2. For $E_1 < E < E_2$ (Case 2), $\partial M_E \cong S^1 \sqcup S^1$ and M'_E is a connected space. A *neck region*

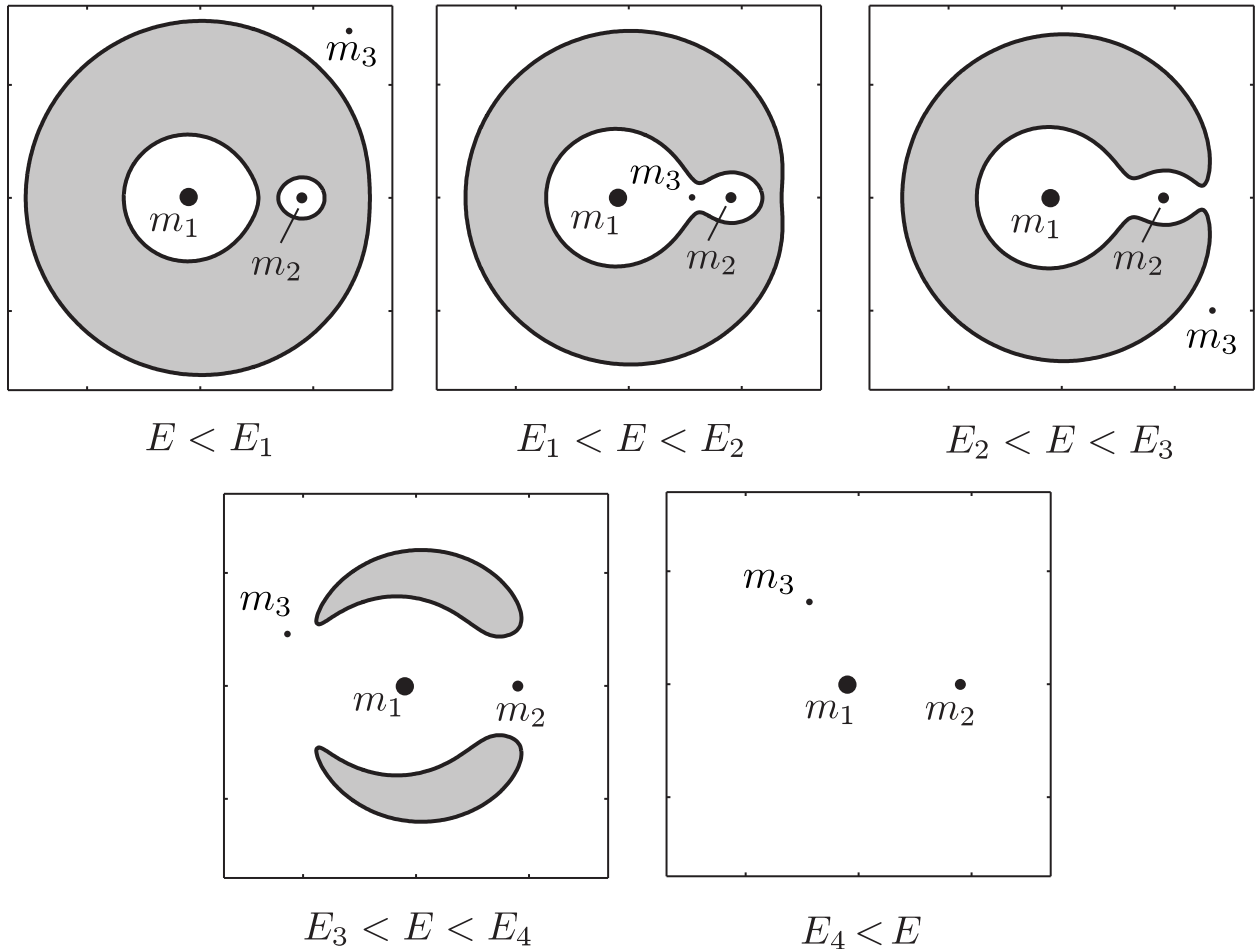


Figure 1.3: The five energy cases plotted for $\mu = 0.3$. Black lines are zero-velocity curves. The gray regions comprise the forbidden realm. Figure edited from [3].

around the L_1 point (see Subsection 1.1.3) appears between the m_1 and m_2 realms, permitting transit between the two realms. In fact, E_1 is the value of the energy at the L_1 point.

3. For $E_2 < E < E_3$ (Case 3), $\partial M_E \cong S^1$. A neck region around the L_2 point appears between the m_2 and exterior realms, permitting transit between all three realms. E_2 is the value of the energy at the L_2 point. The classical theory of PCR3BP low energy transit, as well as Chapters 2 and 3, is usually concerned with this energy interval.
4. For $E_3 < E < E_4$ (Case 4), $\partial M_E \cong S^1 \sqcup S^1$ and M_E is a connected space. A neck region around the L_3 point opens between m_1 and exterior realms, permitting direct transit between the two realms. E_3 is the value of the energy at the L_3 point.
5. For $E_4 < E$ (Case 5), $\partial M_E \cong \emptyset$. The forbidden realm disappears and the particle can move anywhere in position space. Chapter 4 is concerned with this energy interval.

Notice how the realms are topologically the three disjoint components of M_E in the Case 1 energy interval, whereas they are meaningless in the Case 5 energy interval. In the Case 3 energy interval, we define the m_1 realm as the connected neighborhood of m_1 that lies entirely within M_E and which is bounded by a vertical line through the L_1 point. We define the m_2 realm as the connected neighborhood of m_2 that lies entirely within M_E and which is bounded by vertical lines through the L_1 and L_2 points. We define the exterior realm as the remaining connected region of M_E .

1.1.3 The Lagrange points

The PCR3BP equations of motion, written in velocity coordinates, are

$$\begin{aligned}
 \dot{x} &= v_x, \\
 \dot{y} &= v_y, \\
 \dot{v}_x &= 2v_y - \frac{\partial U}{\partial x}, \\
 \dot{v}_y &= -2v_x - \frac{\partial U}{\partial y}.
 \end{aligned} \tag{1.19}$$

Equilibrium points of this system, which are usually called *Lagrange points*, *Lagrangian points*, or *libration points* [3, 4], occur when the right hand sides of the equations of motion equal zero. All equilibrium configurations have zero velocity when viewed in the rotating frame because $v_x = v_y = 0$, and so the positions of the equilibrium configurations correspond to critical points of $\bar{U}(x, y)$. There are five critical points and therefore five Lagrange points for all values of μ (see Figure 1.4).

There are two Lagrange points satisfying $y \neq 0$, the *equilateral* or *triangular* points, which always satisfy $x = \frac{1}{2} - \mu$ and $y = \pm \frac{\sqrt{3}}{2}$. The point with positive y is called the L_4 point, whereas the point with negative y is called the L_5 point [3, 4]. The equilateral Lagrange points have interesting properties useful for mission design—for example, they are dynamically stable for $\mu \lesssim 0.0385$ [3, 4, 13]—but they are minimally relevant to the analyses in the current dissertation and will not be discussed in depth.

There are three Lagrange points satisfying $y = 0$, which are called the *collinear* points and

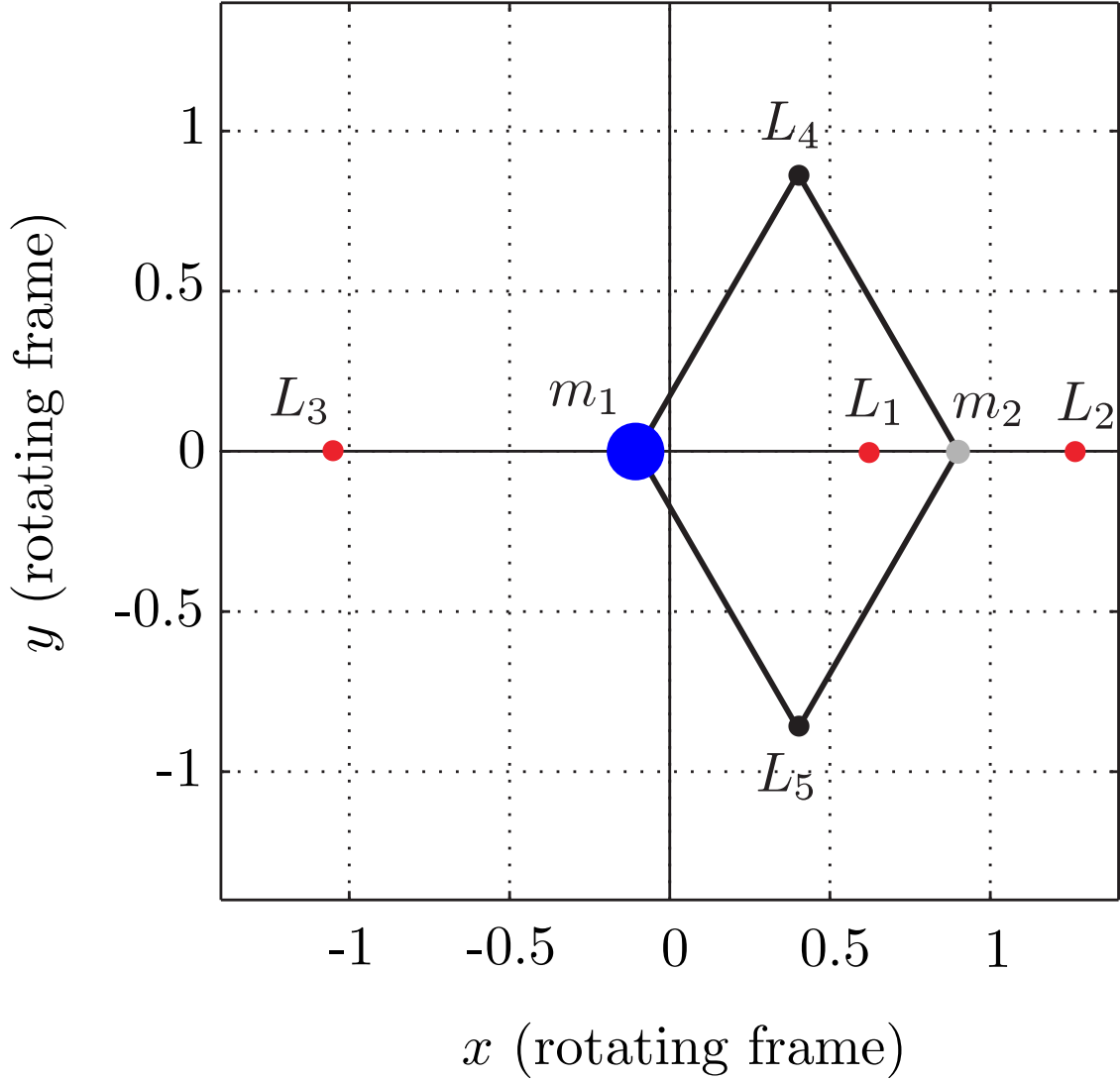


Figure 1.4: The locations of the five Lagrange points in the CR3BP for $\mu = 0.3$. Figure edited from [3].

which are central to our analysis. They occur when (1.13) becomes

$$\begin{aligned}\bar{U}(x, 0) &= -\frac{1}{2}x^2 + U(x, 0) \\ &= -\frac{1}{2}x^2 - \frac{1-\mu}{|x+\mu|} - \frac{\mu}{|x-1+\mu|} - \frac{1}{2}\mu(1-\mu).\end{aligned}\tag{1.20}$$

For all values of μ , $\bar{U}(x, 0)$ has three critical points. The critical point that we denote L_1 has $x \in (-\mu, 1-\mu)$ or $x \in (0, 1)$; the critical point that we denote L_2 has $x \in (1-\mu, \infty)$ or $x \in$

(1, 1.271630); the critical point that we denote L_3 has $x \in (-\infty, -\mu)$ or $x \in (-1.198406, -1)$ [3, 4]. This assignment of the labels L_1 , L_2 , and L_3 is overwhelmingly used in the literature and in space mission design, but alternate conventions do exist; for example, the points to which “ L_1 ” and “ L_2 ” refer are occasionally interchanged (see [4]). In addition, as discussed in Subsection 1.1.1, the rotating frame coordinate system is sometimes “flipped” in the literature, which changes the notated locations of the equilibria even if the standard naming scheme is being used.

Computing the locations of the L_1 and L_2 points necessitates solving the quintic equation

$$\gamma^5 \mp (3 - \mu)\gamma^4 + (3 - 2\mu)\gamma^3 - \mu\gamma^2 \pm 2\mu\gamma - \mu = 0 \quad (1.21)$$

where γ is the distance of the equilibrium point from m_2 and the upper sign is for locating the L_1 point whereas the lower sign is for locating the L_2 point. Computing the location of the L_3 point instead necessitates solving the quintic equation

$$\gamma^5 + (2 + \mu)\gamma^4 + (1 + 2\mu)\gamma^3 - (1 - \mu)\gamma^2 - 2(1 - \mu)\gamma - (1 - \mu) = 0 \quad (1.22)$$

where γ is now the distance of the equilibrium point from m_1 [4]. Alternatively, taking the first derivative of (1.20) and then applying a numerical rootfinder, like MATLAB’s `fzero` routine, to an initial guess in the interval of the interest easily yields the approximate locations of the collinear points.

1.1.4 Linearization about the Lagrange points

As stated previously, transit between realms at low energies must occur in neighborhoods of the collinear Lagrange points. Consider a collinear Lagrange point L_i located at $\mathbf{x}_e =$

$(x_e, 0, 0, 0)$ in velocity coordinates. Let $H(\mathbf{x}_e) = E_i$. Smoothness considerations and our assertions in Subsection 1.1.2 imply that, for sufficiently small $0 < r \ll 1$, there must exist some $E > E_i$ such that transit between realms is impossible without passing through the closed 4-ball $\overline{\mathbb{B}(\mathbf{x}_e, r)} \subset M_E$. Therefore, for sufficiently small r , the local dynamical geometry in the neighborhoods of the Lagrange points will control phase space transport. We ascertain this geometry by *linearizing* the dynamics around the Lagrange points.

To linearize and describe the resultant phase space geometry, we use the Hamiltonian dynamics approach outlined in [3]. This methodology has distinct advantages over competing techniques, such as the Lagrangian dynamics approach also described in [3] or the relatively direct derivation in [4, 12], because it enables the derivation of “local” integrals of motion in the linear dynamics and because the resulting equations of motion benefit from the symplectic structure. Extremely useful for rigorous analysis of the linear geometry, the method will be generalized to periodically-perturbed systems in Chapters 2 and 5.

The Legendre transformation 1.12 suggests that in momentum coordinates the location of L_i is $(x_e, 0, 0, x_e)$. Subject the full Hamiltonian system to a canonical transformation so that $(x_e, 0, 0, x_e)$ becomes the origin, and then expand (1.11) via Taylor series. Discarding all terms greater than quadratic order results in a quadratic Hamiltonian

$$H_2 = \frac{1}{2} ((p_x + y)^2 + (p_y - x)^2 - ax^2 + by^2) \quad (1.23)$$

where $a = 2m\bar{u} + 1$ and $b = \bar{\mu} - 1$ with

$$\bar{\mu} = \mu |x_e - 1 + \mu|^{-3} + (1 - \mu) |x_e + \mu|^{-3}. \quad (1.24)$$

H_2 generates the linearized, Hamiltonian equations of motion

$$\begin{aligned}
\dot{x} &= \frac{\partial H_l}{\partial p_x} = p_x + y, \\
\dot{y} &= \frac{\partial H_l}{\partial p_y} = p_y - x, \\
\dot{p}_x &= -\frac{\partial H_l}{\partial x} = p_y - x + ax, \\
\dot{p}_y &= -\frac{\partial H_l}{\partial y} = -p_x - y - by.
\end{aligned} \tag{1.25}$$

A theorem of Moser implies that the quadratic Hamiltonian, as well as the other integrals of motion that we will demonstrate subsist within it, locally behave as constants of motion for the full dynamics [14, 15].

The eigenvalues are the solutions β to the equation

$$\begin{vmatrix}
-\beta & 0 & 1 & 0 \\
0 & -\beta & 0 & 1 \\
a & 0 & -\beta & 2 \\
0 & -b & -2 & -\beta
\end{vmatrix} = 0 \tag{1.26}$$

which corresponds to the characteristic polynomial

$$p(\beta) = \beta^4 + (2 - \bar{\mu})\beta^2 + (1 + \bar{\mu} - 2\bar{\mu}^2). \tag{1.27}$$

(1.27) is a biquadratic equation. We rewrite it in terms of $\alpha = \beta^2$, resulting in a quadratic equation with solutions

$$\alpha_1 = \frac{\bar{\mu} - 2 + \sqrt{9\bar{\mu}^2 - 8\bar{\mu}}}{2}, \quad \alpha_2 = \frac{\bar{\mu} - 2 - \sqrt{9\bar{\mu}^2 - 8\bar{\mu}}}{2}. \tag{1.28}$$

It can be shown that the constant term of the characteristic polynomial is always negative,

so we take α_1 to be the resultant positive root of the quadratic equation and α_2 to be the resultant negative root. Therefore, the eigenvalues of (1.25) are $\pm\lambda = \pm\sqrt{\alpha_1}, \pm i\nu = \pm\sqrt{\alpha_2}$ where $\lambda, \nu \in \mathbb{R}$.

The corresponding eigenvectors \mathbf{v} must satisfy $(\nabla\mathbf{f} - \beta\mathbf{1})\mathbf{v} = \mathbf{0}$, where \mathbf{f} is the right-hand side of (1.25). Then the following set of equations must hold:

$$\begin{aligned} -\beta v_1 + v_3 &= 0, \\ -\beta v_2 + v_4 &= 0, \\ av_1 - \beta v_3 + 2v_4 &= 0, \\ -bv_2 - 2v_3 - \beta v_4 &= 0. \end{aligned} \tag{1.29}$$

$v_1 = 0$ implies that $\mathbf{v} = \mathbf{0}$, which is not permitted, so we set $v_1 = 1$. This results in the constraint that all eigenvectors must have the form

$$\mathbf{v} = (1, v_2, \beta, \beta v_2) \tag{1.30}$$

It also implies that the third and fourth equations comprising (1.29) become

$$\begin{aligned} a - \beta^2 + 2\beta v_2 &= 0, \\ -bv_2 - 2\beta - \beta^2 v_2 &= 0. \end{aligned} \tag{1.31}$$

Let $\beta = \pm\lambda$. Then (1.31) show, after rearranging terms, that

$$v_2 = \pm \frac{\lambda^2 - a}{2\lambda} = \mp \frac{2\lambda}{\lambda^2 + b}. \tag{1.32}$$

We define

$$\sigma = \frac{2\lambda}{\lambda^2 + b} = -\frac{\lambda^2 - a}{2\lambda} > 0. \tag{1.33}$$

Therefore, the eigenvectors corresponding to the real eigenvalues are

$$\begin{aligned}\mathbf{v}_\lambda &= (1, -\sigma, \lambda, -\lambda\sigma), \\ \mathbf{v}_{-\lambda} &= (1, \sigma, -\lambda, -\lambda\sigma)\end{aligned}\tag{1.34}$$

with $\sigma, \lambda \in \mathbb{R}^+$.

Instead let $\beta = \pm i\nu$. Then (1.31) show, after rearranging terms, that

$$v_2 = \pm i \frac{\nu^2 + a}{2\nu} = \pm i \frac{2\nu}{\nu^2 - b}.\tag{1.35}$$

We define

$$\tau = -\frac{\nu^2 + a}{2\nu} = -\frac{2\nu}{\nu^2 - b} < 0.\tag{1.36}$$

Therefore, the eigenvectors corresponding to the imaginary eigenvalues are

$$\begin{aligned}\mathbf{v}_{i\nu} &= (1, -i\tau, i\nu, \nu\tau), \\ \mathbf{v}_{-i\nu} &= (1, i\tau, -i\nu, \nu\tau)\end{aligned}\tag{1.37}$$

with $\nu \in \mathbb{R}^+$ and $\tau \in \mathbb{R}^-$.

1.1.5 Geometry of the linearized dynamics in the eigenbasis

We call the coordinate system with axes $\{\mathbf{v}_\lambda, \mathbf{v}_{-\lambda}, \mathbf{v}_{i\nu}, \mathbf{v}_{-i\nu}\}$ and origin at L_i the *eigenbasis*, and we notate the corresponding eigenbasis coordinates as $\mathbf{x} = (q_1, p_1, q_2, p_2)$. Rewriting (1.25) in terms of the eigenbasis coordinates results in the highly decoupled equations of

motion

$$\begin{aligned} \dot{q}_1 &= \lambda q_1, & \dot{p}_1 &= -\lambda p_1, \\ \dot{q}_2 &= \nu p_2, & \dot{p}_2 &= -\nu q_2 \end{aligned} \tag{1.38}$$

generated by the quadratic Hamiltonian

$$\tilde{H}_2 = \lambda q_1 p_1 + \frac{1}{2} \nu (q_2^2 + p_2^2). \tag{1.39}$$

The solutions of (1.38) are

$$\begin{aligned} q_1(t) &= q_{10} e^{\lambda t}, \\ p_1(t) &= p_{10} e^{-\lambda t}, \\ q_2(t) &= q_{20} \cos(\nu t) + p_{20} \sin(\nu t), \\ p_2(t) &= -q_{20} \sin(\nu t) + p_{20} \cos(\nu t) \end{aligned} \tag{1.40}$$

for initial conditions $\mathbf{x}(0) = (q_{10}, p_{10}, q_{20}, p_{20})$. Note that (1.39) is not the only constant of motion; both $q_1 p_1$ and $q_2^2 + p_2^2$, the two constituent components of the Hamiltonian, are individually conserved.

Subsection 1.1.4 briefly described the “neck regions” about the Lagrange points as closed unit balls $\overline{\mathbb{B}(\mathbf{x}_e, r)}$ (for some $r \in \mathbb{R}$) which separated connected regions of M_E . This definition is useful for attaining basic topological intuition, but in order to analyze the local transit structure we will define equilibrium regions using a more geometrically precise construction.

We define the equilibrium region \mathcal{R} (following [3]) as the region of phase space in which the

two equations

$$\begin{aligned} \tilde{H}_2 &= \varepsilon, \\ |p_1 - q_1| &\leq c \end{aligned} \tag{1.41}$$

both hold for some $c, \varepsilon \in \mathbb{R}^+$. $\mathcal{R} \cong S^2 \times I$, because each value of $p_1 - q_1$ along the interval $I = [-c, c]$ corresponds to a two-sphere

$$\frac{\lambda}{4}(p_1 + q_1)^2 + \frac{\nu}{2}(q_2^2 + p_2^2) = \varepsilon + \frac{\lambda}{4}(p_1 - q_1)^2. \tag{1.42}$$

(1.40) imply that the flow can be described as the Cartesian product of two *canonical planes*: the first canonical plane in terms of q_1 - p_1 , which hosts a linear saddle point and so is also called the *saddle projection*, and the second canonical plane in terms of q_2 - p_2 , which hosts a linear center point and so is called the *center projection*. The resulting geometry is depicted in Figure 1.5. Within the saddle projection, the zero-velocity curve ∂M_E locally manifests as the zero-velocity hyperbola $q_1 p_1 = \frac{\varepsilon}{\lambda}$, which the structure of (1.39) implies must bound the motion. The gray area in Figure 1.5 is the linearized approximation of the forbidden region, for motion at the selected energy ε is impossible in this region. \mathcal{R} is bounded by both $q_1 p_1 = \frac{\varepsilon}{\lambda}$ and the lines $p_1 - q_1 = \pm c$, the latter of which are the projections of n_1 and n_2 onto the first canonical plane.

Because $q_1 p_1$ is a constant of the motion, all motion in the saddle plane traces out hyperbolas of the form $q_1 p_1 = k_1$ for some constant $k_1 \in \mathbb{R}$. If $k_1 > 0$, then both branches of the hyperbola intersect with both bounding lines $p_1 - q_1 = \pm c$, whereas if $k_1 < 0$, then each branches of the hyperbola intersects with only one of the bounding lines. *This observation is the theoretical foundation of the low-energy transport theory*, because the n_1 bounding sphere separates \mathcal{R} from one realm of motion whereas the n_2 bounding sphere separates \mathcal{R} from

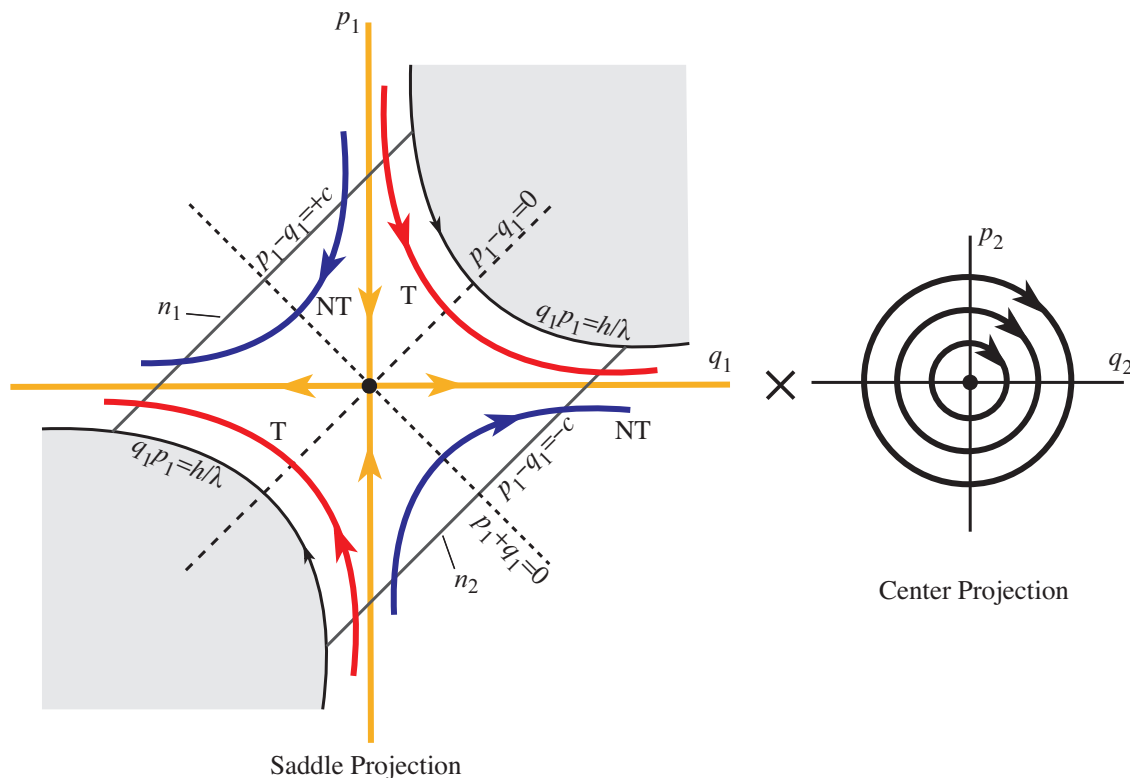


Figure 1.5: The projection of the neck region \mathcal{R} onto the canonical planes. In the saddle projection, the dot at the center represents the Lagrange point and its center manifold, and the orange lines represent the stable (arrows pointing towards the origin) and unstable (arrows pointing away from the origin) manifolds. Blue trajectories enter and leave \mathcal{R} from the same bounding sphere, whereas red trajectories enter and leave \mathcal{R} from different bounding spheres. These two cases correspond to orbits which do not transit between the realms and orbits which do transit between the realms, respectively. Figure edited from [3].

a different realm of motion. Thus, distinguishing trajectories that transit between realms from trajectories that do not transit between realms becomes possible.

Because $q_2^2 + p_2^2$ is also a constant of the motion, all motion in the center plane traces out circles of the form $q_2^2 + p_2^2 = k_2^2$ of some constant radius $k_2 \geq 0$. Along $q_1 p_1 = \frac{\varepsilon}{\lambda}$, $k_2 = 0$, and so phase space transit in the saddle plane is fastest along the zero-velocity curve because it is purely hyperbolic. On the other hand, if $q_1 = p_1 = 0$, the motion of the entire trajectory is purely oscillatory.

Using this description, a few basic types of trajectories are distinguishable [3]:

1. If $q_1 = p_1 = 0$, the trajectory lies on the *center manifold* of the libration point. It takes the form of a periodic orbit, which is usually called a *Lyapunov orbit* (occasionally romanized as *Liapunov orbit*; see, for instance, [16]). If $q_2 = p_2 = 0$ also holds, then the trajectory is the Lagrange point itself.
2. If $q_1 = 0$ and $p_1 \neq 0$, the trajectory lies on the *stable manifold*, which asymptotically approaches the center manifold as $t \rightarrow \infty$. If $p_1 = 0$ and $q_1 \neq 0$, the trajectory lies on the *unstable manifold*, which asymptotically approaches the center manifold as $t \rightarrow -\infty$.
3. Each branch of the hyperbolas with $k_1 > 0$ intersects both bounding lines $p_1 - q_1 = \pm c$. Trajectories with this behavior are called *transit orbits* because they pass between realms of motion.
4. Each branch of the hyperbolas with $k_1 < 0$ intersects only one of the bounding lines $p_1 - q_1 = \pm c$. Trajectories with this behavior are called *nontransit orbits* because they do not pass between realms of motion, instead returning to the realms from which they came.

Notice how the stable and unstable manifolds physically separate the transit orbits from the nontransit orbits. The stable and unstable manifolds each have the topology $\mathcal{C} = S^1 \times \mathbb{R}$, which corresponds to a cylinder—each point along the lines shown in the saddle projection corresponds to a circle in the center projection—and so are sometimes called *tubes*. The orbits inside the tube transit, whereas the orbits outside the tube do not transit. This observation is the origin of the epithet *tube dynamics*, which is sometimes used in reference to the globalized low-energy transport theory [3].

1.1.6 Geometry of the linearized dynamics in standard coordinates

The eigenbasis analysis of the dynamics described in Subsection 1.1.5 is convertible back into the standard rotating frame coordinate system. Its projection onto position space completes our overview of the CR3BP transit theory [17].

Subsection 1.1.4 established that the eigenvalues of the linearized dynamics are $\pm\lambda$ and $\pm i\nu$ with eigenvectors $\mathbf{v}_{\pm\lambda}$ and $\mathbf{v}_{\pm i\nu}$. Then the general solution in standard position/velocity coordinates is

$$\mathbf{x}(t) = \alpha_1 e^{\lambda t} \mathbf{v}_\lambda + \alpha_2 e^{-\lambda t} \mathbf{v}_{-\lambda} + 2 \operatorname{Re} (\beta e^{i\nu t} \mathbf{v}_{i\nu}) \quad (1.43)$$

where $\alpha_1, \alpha_2 \in \mathbb{R}$ and $\beta = \beta_1 + i\beta_2 \in \mathbb{C}$.

In particular, we have

$$x(t) = \alpha_1 e^{\lambda t} + \alpha_2 e^{-\lambda t} + 2(\beta_1 \cos(\nu t) - \beta_2 \sin(\nu t)) \quad (1.44)$$

which implies that the first term dominates the dynamics for $t \rightarrow \infty$ and the second term dominates the dynamics for $t \rightarrow -\infty$. In either case, depending on the sign of α_1 or α_2 , $x(t) \rightarrow -\infty$, $x(t) = 0$, or $x(t) \rightarrow \infty$. Different combinations of signs result in the same basic types of trajectories described in the previous subsection [17]:

1. If $\alpha_1 = \alpha_2 = 0$, the trajectory is a Lyapunov orbit. The center manifold to the libration point is foliated by family of these Lyapunov orbits parameterized by ϵ . m_3 travels the periodic orbit in a clockwise direction. The major axis of the orbit has length $2|\tau| \sqrt{\frac{\epsilon}{\kappa}}$ and coincides with the y -axis, whereas the minor axis of the orbit has length $2\sqrt{\frac{\epsilon}{\kappa}}$ and coincides with the x -axis. $\kappa = -a + b\tau^2 + \nu^2 + \nu^2\tau^2 \in \mathbb{R}^+$.
2. If $\alpha_1 = 0$ and $\alpha_2 \neq 0$, the trajectory lies on the stable manifold, which asymptotically

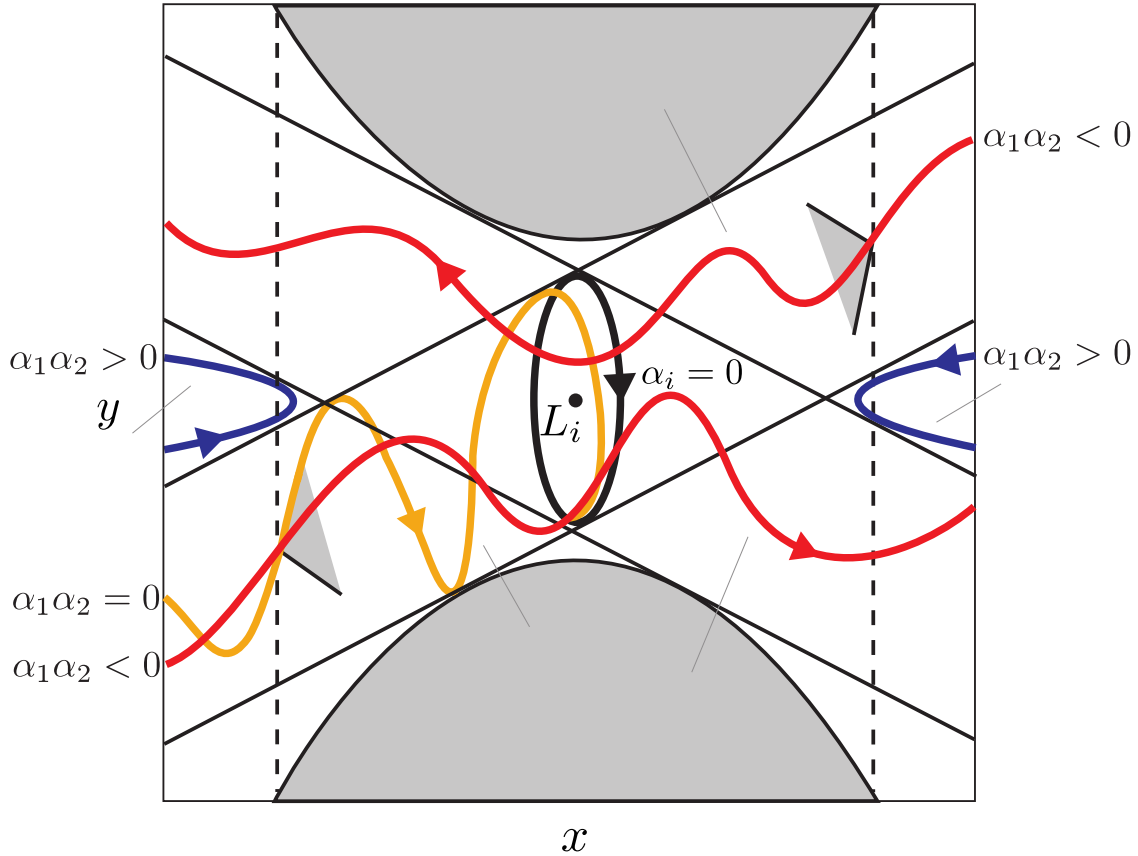


Figure 1.6: The projection of the neck region \mathcal{R} onto position space. The dot at the center represents a Lagrange point, which is surrounded by the black Lyapunov orbit corresponding to the chosen energy. The orange trajectory is on the stable manifold to the Lyapunov orbit. The blue trajectories fail to transit, whereas the red trajectories transit. The gray triangles represent the wedges of velocity for which transit is possible at the chosen position space point. Figure edited from [3].

approaches a Lyapunov orbit as $t \rightarrow \infty$, and must lie between the lines $y = \sigma x \pm 2\sqrt{2\epsilon(\sigma^2 + \tau^2)/\kappa}$. If $\alpha_2 = 0$ and $\alpha_1 \neq 0$, the trajectory lies on the unstable manifold, which asymptotically approaches a Lyapunov orbit as $t \rightarrow -\infty$, and must lie between the lines $y = -\sigma x \pm 2\sqrt{2\epsilon(\sigma^2 + \tau^2)/\kappa}$.

3. If $\alpha_1\alpha_2 < 0$, the trajectory is a transit orbit because as $t \rightarrow \infty$ $x(t) \rightarrow \pm\infty$ and as $t \rightarrow -\infty$ $x(t) \rightarrow \mp\infty$.
4. If $\alpha_1\alpha_2 < 0$, the trajectory is a nontransit orbit because as $t \rightarrow \pm\infty$ either $x(t) \rightarrow \infty$

or $x(t) \rightarrow -\infty$.

Each point in \mathcal{Q} is associated with a set of velocities (sometimes called the “wedge of velocities” [3]) for which $\alpha_1\alpha_2 < 0$ and so transit occurs, although this set is permitted to be empty. Points outside of the set cannot transit because $\alpha_1\alpha_2 > 0$, and points on the boundary lie on the stable and unstable manifolds [17].

1.2 Selected historical applications of manifold-based transit geometry

This low-energy phase space transit geometry has been used repeatedly for space mission design. We provide an summary of some milestones in the application of the theory without intending comprehensiveness.

The International Sun/Earth Explorer 3 (ISEE-3) spacecraft, which was launched in 1978, was the first spacecraft inserted into orbit around a Lagrange point [18]. ISEE-3 was placed into a *halo orbit*—a periodic, three-dimensional trajectory on a collinear Lagrange point’s center manifold in the spatial circular restricted three-body problem—around the Sun-Earth L_1 point [3]. Transferring ISEE-3, which had been gathering data on the solar wind and interplanetary medium, from the Sun-Earth L_1 point to the Sun-Earth L_2 point was seriously considered [19], but it was instead renamed the *International Cometary Explorer* and redirected to study the magnetotail of the Earth and then the comet Giacobini-Zimmer, which it intercepted in 1985 [20, 18].

The plan that would have transferred ISEE-3 between Sun-Earth Lagrange points in the mid-1980’s would have replaced ISEE-3 at the L_1 point with a spacecraft called the Interplanetary Physics Laboratory (IPL) [19, 21]. However, the launch of IPL (which was

eventually renamed Wind) only occurred in 1994, and its insertion at the Sun-Earth L_1 point was delayed until 2004 by other mission objectives [22, 23]. As a consequence, the Solar Heliospheric Observatory (SOHO) and the Advanced Composition Explorer (ACE) were the first spacecraft to replace ISEE-3 at the Sun-Earth L_1 point, arriving in 1996 and 1997, respectively [23]. Wind, SOHO, and ACE were joined by the Deep Space Climate Observatory (DSCOVR) in 2015 [24]. Wind was originally inserted into a *Lissajous orbit*—a three-dimensional trajectory which is similar to a halo orbit but whose path is quasiperiodic instead of periodic [3]—around L_1 [25]. However, its trajectory was altered to a halo orbit in 2020 [26]. SOHO and ACE were launched into halo orbits, whereas DSCOVR was launched into a Lissajous orbit [22, 24].

Hiten, launched in 1991, constitutes an interesting case study of the use of a low-energy trajectory to salvage a mission that underwent unexpected spacecraft failure [18, 27, 28]. The mission utilized two spacecraft, MUSES-A (renamed Hiten after launch) and Hagoromo, and was intended to make Japan the third country to orbit the Moon. Hiten released Hagoromo, a smaller spacecraft with no scientific instrumentation, into lunar orbit successfully, but Hagoromo’s transmission system had failed before decoupling from Hiten, preventing Hagoromo from transmitting from lunar orbit [18]. However, a novel trajectory was developed which utilized the theory of *Weak Stability Boundaries*, which encapsulate the points at which gravitational fields balance, in order to insert Hiten itself into lunar orbit using the combined gravitational effects of the Sun, Earth, and Moon [28]. It was later demonstrated that Hiten-style trajectories utilize the manifold structures emanating from the Lagrange points in the CR3BP and the BCP [27, 29].

The Genesis mission, launched in 2001 in order to recover samples of the solar wind [18], was designed to take full advantage of the stable and unstable manifolds associated with the Lagrange points and their center manifolds; it has been described as “the first mission to

be designed using modern dynamical systems theory” [30]. The Genesis mission trajectory utilized a *heteroclinic connection*, or a trajectory lying in the intersection between the unstable manifold to one dynamical object and the stable manifold to another, between halo orbits around the Sun-Earth L_1 and L_2 points [31, 30]. With a single impulsive maneuver with a ΔV of less than 40 m/s, the spacecraft was inserted onto the unstable manifold to the L_1 point, and without any deterministic maneuvers proceeded onto the L_2 orbit [30]. The mission largely succeeded: the trajectory functioned as intended, and although a parachute failed to deploy due to the incorrect installation of an accelerometer, the resultant sample return canister fragments still yielded useful scientific data [18].

The trajectory for the BepiColombo mission, launched in 2018, was calculated by exploring trajectory space to find solutions that achieve “weak capture” around Mercury, but the chosen orbit was demonstrated to exploit the low-energy geometry [32, 33, 34]. Specifically, it followed a heteroclinic connection that linked a Lissajous orbit around the Sun-Mercury L_1 point with a quasi-periodic orbit around Mercury itself in the *elliptic* restricted three-body problem [33].

The James Webb Space Telescope (JWST), launched in 2021, is an example of a mission designed to follow a *quasi-halo orbit* around the Earth-Moon L_2 point [35]. A quasi-halo orbit is a quasi-periodic trajectory surrounding the center manifold of a halo orbit, which itself lies on the center manifold of the libration point [36]. The JWST inserted onto the quasi-halo orbit via the orbit’s stable manifold [37].

1.3 The periodically-perturbed circular restricted three-body problem

The CR3BP can be brought closer to the full ephemeris via a variety of modifications. One approach is to incorporate a time-periodic perturbation into the CR3BP Hamiltonian H which models additional forces which are present in the “real world.” In this dissertation, we discuss two examples of *periodically-perturbed circular restricted three-body problems*: the bicircular problem, or BCP, and the elliptic restricted three-body problem, or ER3BP (see Figure 1.7). We introduce them briefly in the current section, but for more detail the reader is requested to refer to Chapter 2.

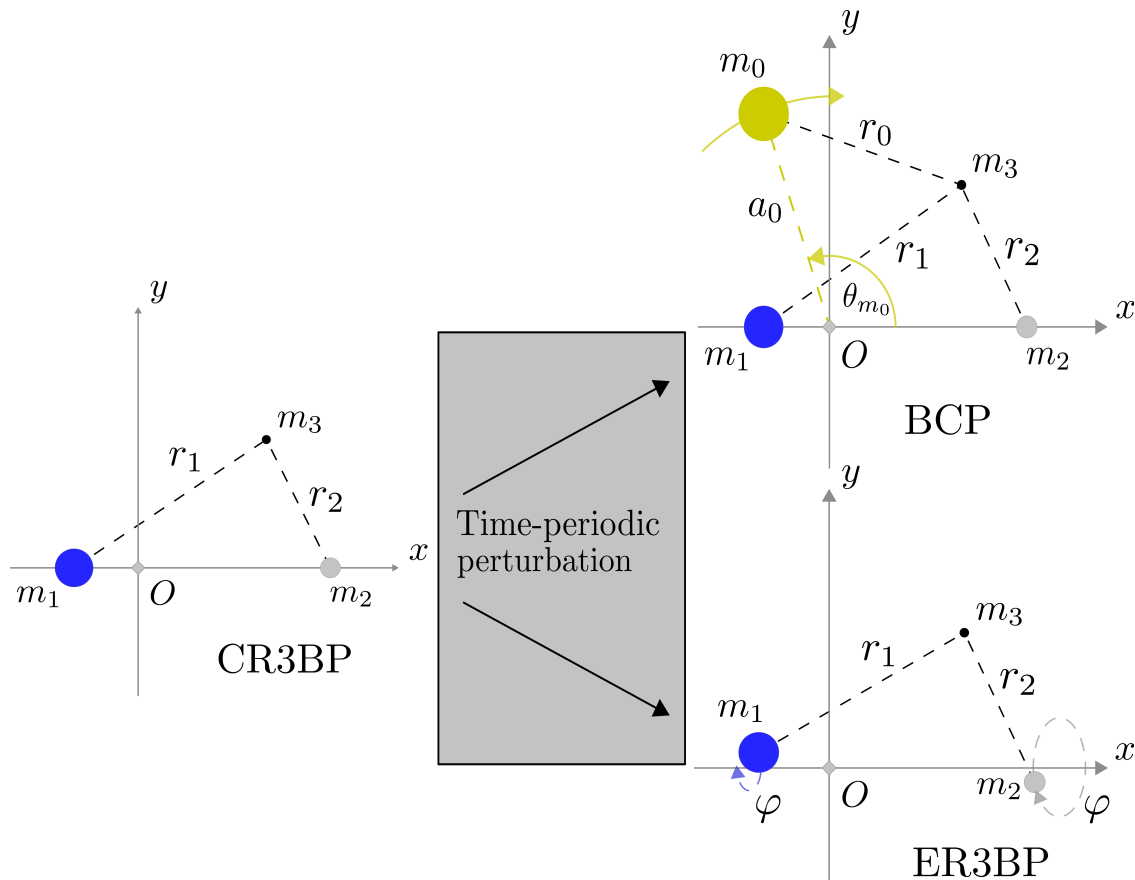


Figure 1.7: The CR3BP bifurcates to the BCP or the ER3BP, depending on the periodic perturbation introduced into the system.

The *bicircular problem (BCP)* corresponds to the introduction of a fourth mass m_0 which appears to orbit the center of the CR3BP [38, 39, 3]. One example of a bicircular problem is the Sun-perturbed Earth-Moon System, in which the Sun perturbs the Earth-Moon CR3BP [39].

The bicircular problem has Hamiltonian $H + H_{m_0}$ where the perturbation takes the form

$$H_{m_0}(t) = \frac{\mu_0}{a_0^2} \left(x \cos \theta_{m_0}(t) + y \sin \theta_{m_0}(t) \right) - \frac{\mu_0}{r_0(t)} \quad (1.45)$$

where,

$$\begin{aligned} r_0(t)^2 &= (x - a_0 \cos \theta_{m_0}(t))^2 + (y - a_0 \sin \theta_{m_0}(t))^2, \\ \theta_{m_0}(t) &= -\omega_{m_0} t + \theta_{m_0 0} \end{aligned} \quad (1.46)$$

where a_0 , μ_0 , ω_{m_0} , θ_{m_0} , $\theta_{m_0 0}$, and r_0 are the distance, mass, angular velocity, current angle, initial angle of m_0 , and distance from the particle, respectively, in non-dimensionalized units.

The *elliptic restricted three-body problem* corresponds to dropping the requirement that the primaries orbit their center of mass in circular orbits, thereby introducing the eccentricity e into the system [40, 4, 3]. In the CR3BP rotating reference frame, m_1 and m_2 move in periodic orbits around their locations in the unperturbed model. One example of an ER3BP is the Earth-Moon system, for in reality $e = 0.0549006$ instead of $e = 0$.

The Hamiltonian for the ER3BP is

$$H_{\text{ER3BP}} = \frac{1}{2}(p_x^2 + p_y^2) - xp_y + yp_x - \frac{\mu_1}{r_1(t)} - \frac{\mu_2}{r_2(t)}, \quad (1.47)$$

with

$$r_i^2(t) = \left| \left(\begin{bmatrix} x \\ y \end{bmatrix} + \frac{1 - \mu_i}{1 + e \cos \varphi(t)} \mathbf{R}(t) \begin{bmatrix} \cos \varphi(t) \\ \sin \varphi(t) \end{bmatrix} \right) \right|^2, \quad (1.48)$$

$$\text{with } \mathbf{R}(t) = \begin{bmatrix} \cos t & \sin t \\ -\sin t & \cos t \end{bmatrix},$$

where $\varphi(t)$ solves

$$\dot{\varphi} = \frac{(1 + e \cos \varphi)^2}{(1 - e^2)^{3/2}}, \quad (1.49)$$

with initial condition $\varphi(0) = \varphi_0$.

1.4 Review of recent developments in the restricted three-body literature

Much new investigation has sought to extend the transport theory described in Section 1.1 in a variety of directions (see Table 1.1).

Some recent work has explored the consequences of introducing dissipation into Hamiltonian systems that host saddle-center equilibrium points in the conservative case, such as the CR3BP [41, 42, 43, 44]. Transit orbits still exist, but the saddle-center dynamics at the equilibrium point are replaced by saddle-spiral sink dynamics, and so the cylindrical tubes of transit orbits bifurcate into ellipsoids. In addition, while the first and second canonical planes are independent in the conservative case, some dissipative systems introduce coupling between the canonical planes whereas others do not [41].

An emerging body of literature also exists to analyze the problem of relative spacecraft

motion in the CR3BP [7, 45, 46]. Within this context, the survival of phase space structures surrounding the collinear Lagrange points, such as the stable and unstable manifolds, has been shown through analysis of the Hamiltonian [7].

Other recent studies have investigated periodically-perturbed CR3BP models. In particular, very much analysis has concerned the computation of families of quasi-periodic orbits, also known as invariant tori, that bifurcate from periodic orbits about the Lagrange points under perturbation [47, 48, 49, 50, 51, 52]. Some work has also investigated the computation of the invariant manifolds emanating from the tori [53, 9, 52] and the heteroclinic connections associated with these manifolds [49, 9]. [9] notably presents the manifolds as the custodians of low-energy phase space transport in the BCP and demonstrates how Lagrange points bifurcate to periodic orbits, but does not provide a systematic geometric method for discriminating between transit and nontransit orbits. Specific applications in which the stable and unstable manifolds are used for insertion into a quasi-periodic orbit in a periodically-perturbed model have also been discussed [54, 55].

The transit geometry of periodically-perturbed three-body problems has not typically been analyzed as a unified theory. Instead, most of the literature treats the elliptic restricted three-body problem, for example, separately from the bicircular problem, using separate and incompatible techniques to render each model more tractable. In the ER3BP, it is customary to use a pulsating frame in which the primaries no longer rotate at constant speed, as this approach renders the flow time-independent [56, 57, 58, 59], although some work has instead used various other sets of “sidereal” coordinates [60, 61, 62]. Within this context, analysis of trajectories on the center manifolds to the collinear points has been performed [63, 40], and transit and nontransit orbits have even been discriminated using local constants of motion, in a similar vein to Section 1.1 but using a much more complicated approach [64]. On the other hand, in the BCP it is common in mission design to patch together two restricted

three-body problems to approximate the dynamics via switching orbits and other techniques [65, 66, 3, 27, 67]. Both techniques are useful, but we take a different tack in the current dissertation which unifies the two phenomena and takes full advantage of the full, time-dependent dynamics in a simple, elegant fashion.

[68, 69, 70] used the theory of *Lagrangian coherent structures (LCS)*, which generalize stable and unstable manifolds to highly time-dependent systems, to calculate tubes separating transit and nontransit orbits. The resultant technique was used to compute a Hiten-style trajectory in the BCP. While this method seems enormously promising, the numerical derivation of Lagrangian coherent structures, which must be extracted from FTLE ridges, limits the analytical rigor of the method [68].

The dynamical transit properties of the periodically-perturbed restricted three-body problem has been analyzed by studying the eigenvalue evolution at the instantaneous libration points in the ER3BP and the BCP as a function of perturbation phase [71]. This method suffers from minimal development of the dynamical geometry.

	[9]	[64]	[68]	[71]	Chapters 2 and 3
Lagrange Periodic Orbits	✓				✓
Stable and Unstable Manifolds	✓	✓	✓		✓
Local Integrals of Motion		✓			✓
Transit Orbit Discrimination		✓	✓		✓
BCP-ER3BP Unification				✓	✓
Use of Invariant Sets	✓	✓			✓
Close Connection to CR3BP Geometry				✓	✓

Table 1.1: Comparison of our transit theory for periodically-perturbed models with the studies in the literature which attempted to formulate a similar theory.

Recent investigation has also hinted at the usefulness of manifold-based dynamics for linking low-energy and high-energy regimes of the CR3BP [72, 73] or for understanding phase space structures numerically demonstrated to exist at high-energies [74]. Many of these works also analyze collision with the singularities residing at the locations of the primaries [72, 73], a topic about which a rich body of work rooted in dynamical systems methods already exists [10, 75, 76, 77, 78, 79]. The rigorous application of manifold-based collision analysis methods to the high-energy phase space structures discovered in [74], which are called the “arches of chaos” and which were discovered—using the numerical method of *fast Lyapunov indicators* (*FLI*)—to create high phase space divergence over short timescales, is the focus of Chapter 4.

1.5 Research overview

Much of this dissertation utilizes the manuscript format permitted by the Virginia Tech Graduate School. Chapters 2, 3, and 4 are written as standalone manuscripts which have been already published or which will soon be submitted for publication. Chapter 5, on the other hand, represents miscellaneous results and is not in manuscript format. Chapter 6 concludes the dissertation and is also not in manuscript format.

In Chapter 2, we analyze to first order the transit structure of the periodically perturbed restricted three-body problem. We demonstrate that phase space transport relies on periodic orbits that generalize the Lagrange points. Using a stroboscopic map, we remove time dependence from the system, and thereby illustrate that under the map the transit geometry is a discrete analogue of the geometry in the unperturbed case.

In Chapter 3, we improve upon the analysis in Chapter 2 by introducing higher order terms of the Taylor series expansion about the Lagrange points, whose coefficients are given by monodromy tensors. We outline a method for using nonlinear approximate stroboscopic

maps to predict the nonlinear transit geometry.

In Chapter 4, we show that the stable and unstable manifolds to the singularities of the circular restricted three-body problem can be identified with the arches of chaos, dynamical structures spanning throughout the solar system that create high rates of phase space stretching at high energies and that were recently uncovered using FLI methods [74]. We also link the arches of chaos with the patched conics approximation.

In Chapter 5, we discuss assorted research results which do not fit within the narrative flow of the preceding chapters. We introduce the Context Manager for Dynamical Systems (CMDS), which is the underlying MATLAB framework that we constructed to facilitate this dissertation research, and outline a method for calculating quadratic Hamiltonians that “generate” linear symplectic maps using the theory of polynomial vector spaces.

In Chapter 6, we summarize our work and discuss methodological commonalities between the different topics. We also elaborate upon concrete applications of this work for mission planning and upon avenues for future study.

Chapter 2

Geometry of low-energy transit orbits in the periodically-perturbed restricted three-body problem

Attribution

This chapter, a collaborative work with Shane Ross, was originally published in *Advances in Space Research*, 70.1 (2020), 144-156. It resides online at <https://doi.org/10.1016/j.asr.2022.04.029>.

Author Contributions

Fitzgerald and Ross conceived of the project. Fitzgerald developed the underlying mathematical model and software, derived the analytical expressions and proofs, implemented the numerical simulations, and analyzed the simulation output with supervisory assistance from Ross. Fitzgerald produced almost all figures, and the remainder were adapted by Fitzgerald from earlier work by Ross. Fitzgerald wrote most of the manuscript with some assistance by Ross. Fitzgerald coordinated the revisions.

2.1 Introduction

In recent decades, investigations of the circular restricted three-body problem (CR3BP) from a dynamical systems point of view have revealed an intricate fabric of manifolds woven between planets and moons [17, 80, 81, 82, 56, 83, 84, 85, 74, 86, 15, 87, 11, 88, 89, 90, 67, 91]. These manifolds separate low-energy *transit trajectories* that successfully pass through neck regions of permitted motion about the Lagrange points, thereby travelling between phase space realms of interest, from *non-transit trajectories* that fail to pass through the neck regions. The phase space structures that separate transit and non-transit trajectories appear when linearizing the governing differential equations about the system's equilibria in the co-orbiting (rotating) frame, the collinear Lagrange points (particularly L_1 and L_2). Linearization nonetheless fails on generalizations of the circular restricted three-body problem subject to time-dependent perturbations, such as fourth-body effects (i.e., the bicircular problem) or orbital eccentricity of the primaries, because the fixed Lagrange points are no longer equilibria. Moreover, the instantaneous (moving) null points of the time varying vector field are not trajectories [92].

In this paper, we introduce a geometric framework for analysis of transit phenomena in time-periodic restricted three-body models like the bicircular problem (BCP) or the elliptic restricted three-body problem (ER3BP) as a natural counterpart to the time-independent circular R3BP (CR3BP). Higher-dimensional time-dependent manifolds, which we refer to as *Lagrange manifolds*¹, dynamically replace the L_1 and L_2 points as the fundamental objects whose stable and unstable manifolds provide the template for low energy dynamical behavior near the smaller primary. Under a time-periodic perturbation of period T , the Lagrange manifold is a manifold in the phase space diffeomorphic to S^1 , that is, a periodic orbit with a (minimal) period equal to T [93]. Additional perturbations, not considered here, would

¹As they are higher-dimensional analogs of the Lagrange *points*

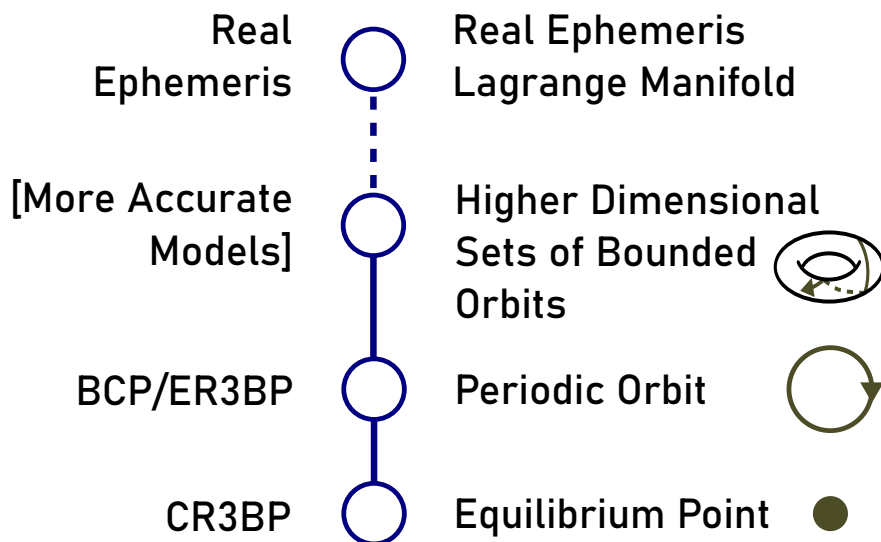


Figure 2.1: Schematic illustrating how the Lagrange manifold bifurcates as astrodynamical models go from simplest and least accurate at the bottom, increasing in fidelity to the real ephemeris. The bifurcation discussed in this paper is the transition from the equilibrium point to the periodic orbit.

further alter the topology, as depicted schematically in Figure 2.1.

Prior investigations into models more complicated than the CR3BP have successfully found periodic and quasi-periodic orbits in the vicinity of former Lagrange points by employing single shooting or multiple shooting algorithms [94, 52]. Studies have found quasi-periodic orbits on the center manifolds of these dynamical replacements [52] and have numerically demonstrated associated transit phenomena [9, 64].

In this paper, we demonstrate that the linear dynamics corresponding to transit and non-transit behavior in T -periodically-perturbed versions of the CR3BP can be reduced to a linear time- T map with the same dynamics and geometry as that in the unperturbed CR3BP. *This is a significant simplification for understanding the geometry of transit orbits*, as results from several decades ago carry over in a straightforward manner, without requiring higher-order expansions. In the phase space of the map, the Lagrange manifold periodic orbit corresponds to an index-1 fixed point with a 1-dimensional stable manifold and 1-dimensional unstable manifold. Construction of transit and non-transit orbits follows from established methods

dating to Conley in the 1960s [17, 15]. The geometry in the linearized regime extends to the full nonlinear system, where the linear symplectic map near the Lagrange manifold will be replaced by a nonlinear symplectic map. Finding this nonlinear map is not our current goal, but is an objective for future research. According to a theorem by Moser, the linear map provides the basic geometric picture that carries over to the nonlinear case [14, 95]. We demonstrate our results by considering transit orbits near the Earth-Moon L_1 cislunar point, the closest Lagrange point to Earth and a likely future hub for a space transportation system [96, 97, 98].

The paper is organized as follows. Section 2.2 reviews the nature of phase space transit in the planar CR3BP. Section 2.3 reviews an assortment of mathematical preliminaries, such as flow maps and state transition matrices, necessary for understanding the rest of the analysis. It also introduces the general theory of periodic orbit Lagrange manifolds and outlines a method for determining their initial conditions. Section 4 analyzes the local dynamics near an index-1 saddle-type fixed point of the Poincaré stroboscopic map (also called an elliptic-hyperbolic point in the discrete map context). Sections 2.5 and 2.6 apply these results to two examples of periodic perturbations of the CR3BP, illustrated in Figure 2.2: (i) the effect of the Sun's perturbation, known as the *bicircular problem* (BCP) and (ii) the effect of the eccentricity in the Earth-Moon system, the *elliptic R3BP* (ER3BP). In putting these two distinct modifications of the R3BP on an equal footing, we seek to emphasize the generality of our main result, the geometry of transit and non-transit orbits.

2.2 Classification of orbits in the circular restricted three-body problem

2.2.1 Equations of motion

The CR3BP models the motion of a small mass or test particle m_3 in the gravity field of two massive bodies $m_1 > m_2$. Masses m_1 and m_2 orbit their common center of mass O in circular orbits. We consider here only the planar CR3BP where m_3 is free to move throughout the m_1 - m_2 orbital plane. Generalizing the following theory to the spatial CR3BP is very straightforward in the unperturbed case, and so we consider descriptions of the spatial unperturbed and perturbed cases to be beyond the scope of the current work. The equations of motion are written in a rotating reference frame with origin O . The x -axis of the rotating frame coincides with the line between m_1 and m_2 whereas the y -axis points in the direction of motion of m_2 (see Figure 2.2).

The non-dimensional equations of motion for m_3 in the planar CR3BP (our focus here) are autonomous Hamilton's canonical equations with Hamiltonian function [3],

$$H_{\text{CR3BP}} = \frac{1}{2}(p_x^2 + p_y^2) - xp_y + yp_x - \frac{\mu_1}{r_1} - \frac{\mu_2}{r_2}, \quad (2.1)$$

where,

$$r_1 = \sqrt{(x + \mu_2)^2 + y^2}, \quad r_2 = \sqrt{(x - \mu_1)^2 + y^2}, \quad (2.2)$$

with $\mu_1 = 1 - \mu$ and $\mu_2 = \mu$ the non-dimensional masses of m_1 and m_2 , where $\mu = m_2/(m_1 + m_2)$ is the mass parameter.

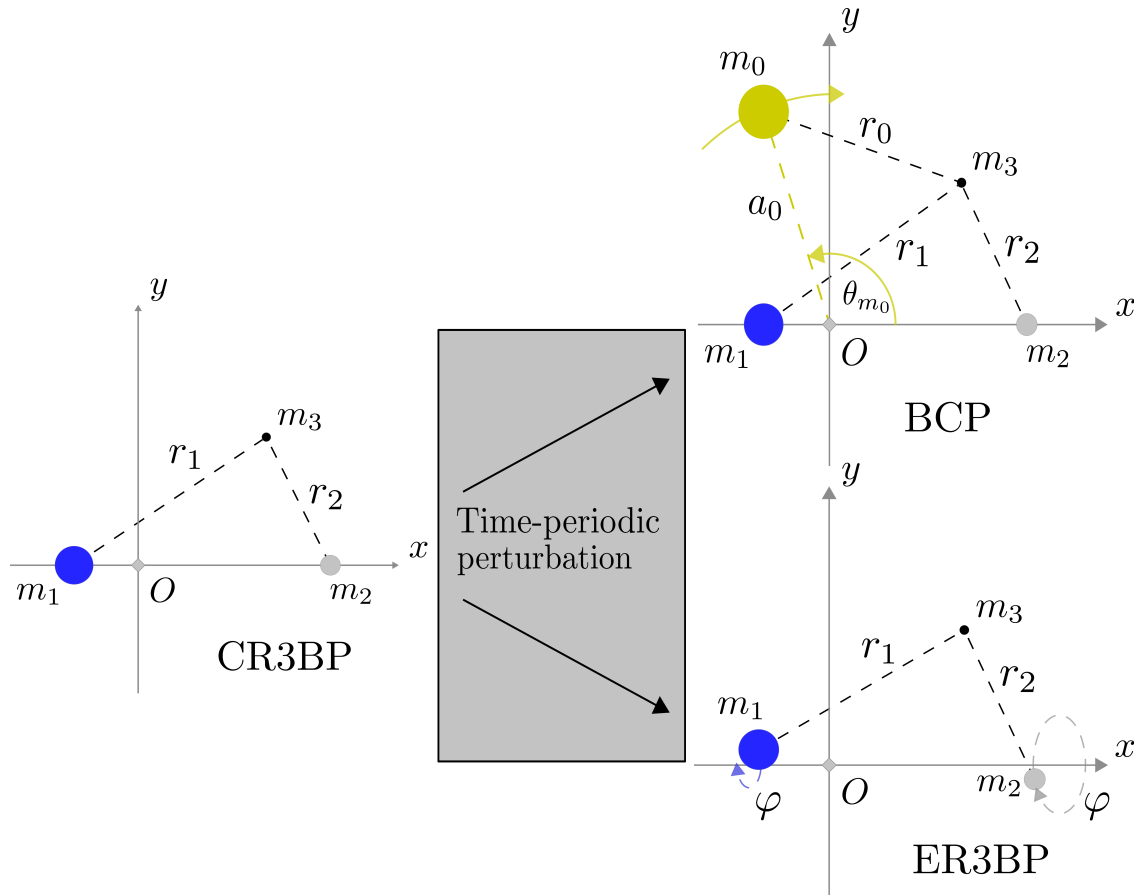


Figure 2.2: The models considered, viewed in the m_1 - m_2 barycentered average rotating frame.

2.2.2 The Lagrange points

The CR3BP, as an autonomous system, has five equilibrium points called *Lagrange points* as viewed in the rotating frame, as shown in Figure 2.3(a). The three equilibria lying on the x -axis, L_1 , L_2 , and L_3 , are index-1 saddle *collinear points*; the remaining two, which form equilateral triangles with m_1 and m_2 , are the *triangular points* (center \times center points for $\mu \lesssim 0.039$). Because of their connection with low energy orbits via transit from orbits about m_2 and about m_1 and vice-versa, we focus on the collinear points.

2.2.3 The Hill's region and the Hamiltonian energy

Trajectories of the CR3BP conserve the Hamiltonian energy, $H_{\text{CR3BP}} = E$, where $E \in \mathbb{R}$ is the initial Hamiltonian energy. The *Hill's region* is the subset of position space throughout which m_3 has enough energy to travel. The boundary of the *Hill's region*, beyond which lies the *forbidden realm*, is called the *zero-velocity surface* in the spatial case and *zero-velocity curve* in the planar case [4]. The qualitative characteristics of the corresponding Hill's region naturally assign E to one of five different intervals (see Figure 2.3(b)):

1. For $E < E_1$, m_3 is confined to either a subset of position space around m_1 (the m_1 *realm*), a subset of position space around m_2 (the m_2 *realm*), or a subset of position space outside m_1 and m_2 (the exterior realm). In this situation, m_3 cannot cross between any of the three realms.
2. For $E_1 < E < E_2$, a *neck region* opens up around the L_1 point that permits travel between the m_1 and m_2 realms.
3. For $E_2 < E < E_3$, another neck region opens up around the L_2 point that permits travel between the m_2 and exterior realms.
4. For $E_3 < E < E_4$, yet another neck region opens up around the L_3 point that permits travel between the m_1 and exterior realms.
5. For $E_4 < E$, the forbidden realm completely disappears.

Thus, regions around the collinear Lagrange points play an important role in controlling transit between realms. We typically consider the second or third cases, in which transit between realms is possible but is governed by manifold structures associated with L_1 and in the latter case L_2 .

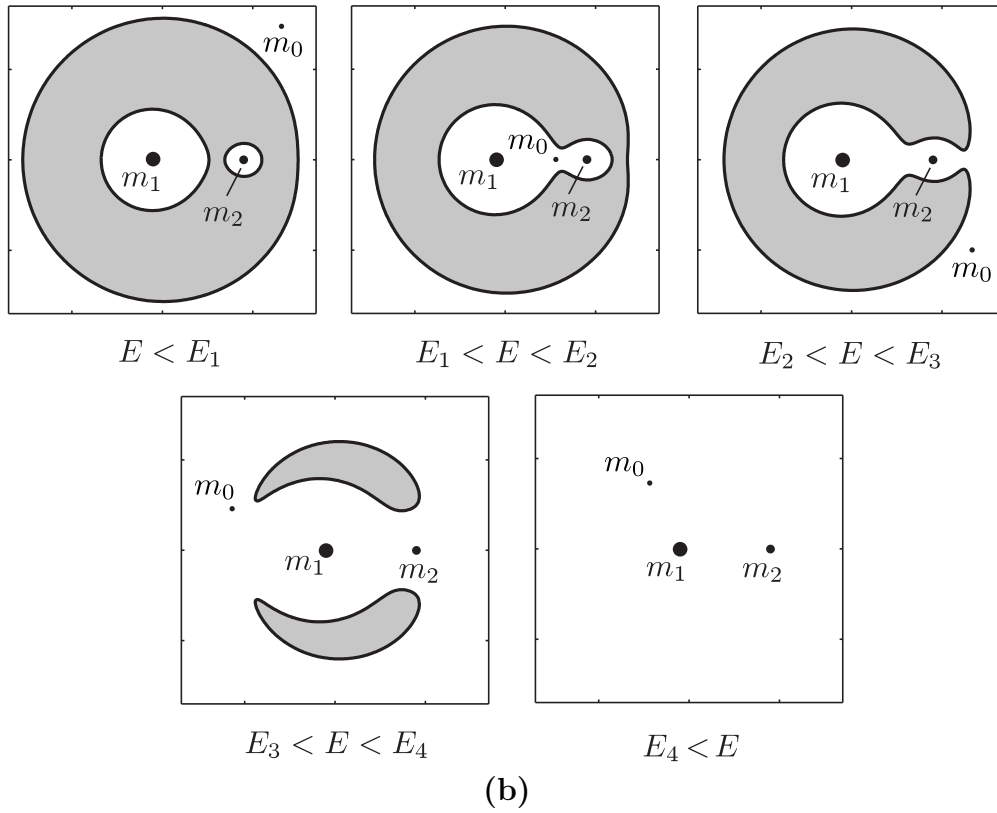
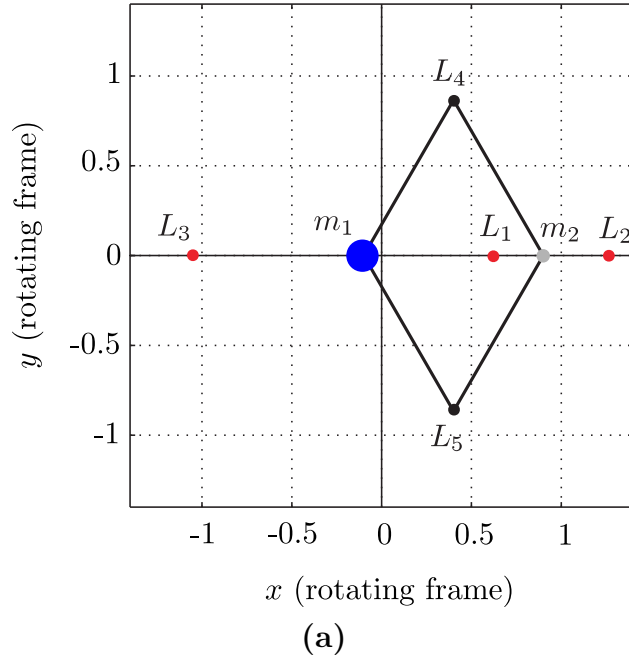


Figure 2.3: (a) The Lagrange points of the CR3BP for $\mu = 0.3$. (b) The five cases of the energetically accessible regions (i.e., Hill's region) by CR3BP Hamiltonian energy.

2.2.4 Linearization about L_1 and L_2

Linearizing the Hamilton's equations about L_1 or L_2 , the eigenvalues of the linear system are a purely real pair, $\pm\lambda$, and a purely imaginary pair, $\pm i\nu$, where $\lambda, \nu > 0$, which makes such points index-1 saddles [99]. The corresponding generalized eigenvectors, when properly rescaled, provide a *symplectic* eigenbasis [41]. In the symplectic eigenbasis with corresponding coordinates and momenta (q_1, p_1, q_2, p_2) , the linearized equations simplify to,

$$\begin{aligned} \dot{q}_1 &= \lambda q_1, & \dot{p}_1 &= -\lambda p_1, \\ \dot{q}_2 &= \nu p_2, & \dot{p}_2 &= -\nu q_2. \end{aligned} \tag{2.3}$$

which are Hamilton's canonical equations with corresponding quadratic Hamiltonian function,

$$H_2 = \lambda q_1 p_1 + \frac{1}{2}\nu(q_2^2 + p_2^2). \tag{2.4}$$

As (2.3) is linear, its solution is readily obtained and must conserve the quadratic Hamiltonian function (2.4).

2.2.5 Geometry of the linearized equilibrium region

The two canonical planes associated with (2.3) are uncoupled: the q_1 - p_1 canonical plane has saddle behavior whereas the q_2 - p_2 canonical plane has center behavior, as shown in Figure 2.4.

Choose a fixed, small $h > 0$ such that $H_2 = h$. Because $\frac{1}{2}\nu(q_2^2 + p_2^2) \geq 0$, a forbidden region in the saddle projection arises for each h . The boundary of the forbidden region is given by the hyperbolas $q_1 p_1 = h/\lambda$; the shape of the area outside this boundary reproduces the neck region found in the full equations of motion [17], as shown in Figure 2.4.

For some small constant $c > 0$, initial conditions along the line $p_1 - q_1 = +c$ lie entirely

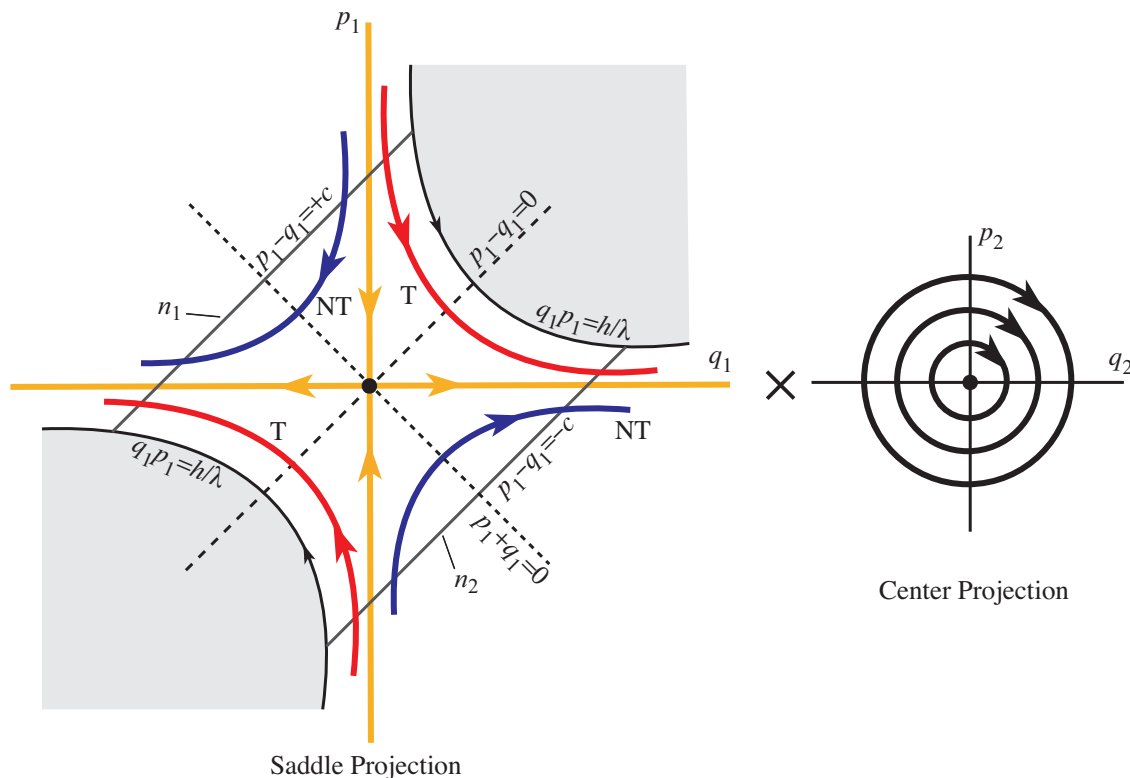


Figure 2.4: The two canonical planes of the dynamics in the symplectic eigenbasis in the neighborhood of a collinear Lagrange point; orbits labeled T transit from one realm to another, while those labeled NT do not.

within one realm whereas initial conditions along the line $p_1 - q_1 = -c$ lie entirely within the other. For details, see [3] and references therein. We refer to these boundaries as n_1 and n_2 , respectively (see Figure 2.4).

Orbits present in the neighborhood of the equilibrium point can be classified [17] according to their behaviors in the saddle projection (see Figure 2.4):

1. The point at the origin of the saddle projection corresponds to the center manifold of the Lagrange point. Each trajectory within the center manifold is a planar periodic orbit called a *Lyapunov orbit* about the equilibrium point.
2. The q_1 -axis and the p_1 -axis of the saddle projection correspond to trajectories that asymptotically approach the Lyapunov orbits as $t \rightarrow -\infty$ or $t \rightarrow +\infty$, respectively.

These sets of trajectories are the *unstable and stable manifolds*, respectively, of the Lyapunov orbit of energy h , or, together, the *asymptotic orbits*.

3. The hyperbolic trajectories in the first and third quadrants, when integrated, intersect both $p_1 - q_1 = +c$ and $p_1 - q_1 = -c$. Because they pass from one realm to the other, they are called *transit orbits*.
4. The hyperbolic trajectories in the second and fourth quadrants are unable to intersect both $p_1 - q_1 = +c$ and $p_1 - q_1 = -c$. As they do not pass from one realm to the other, they are *non-transit orbits*.

This qualitative picture in the linearized case carries over to the nonlinear setting via a theorem of Moser [14, 95].

2.3 Lagrange manifolds in periodically-perturbed systems

2.3.1 Periodically-perturbed systems

In the analysis which follows, we consider periodically-perturbed non-autonomous dynamical systems of the form,

$$\dot{\mathbf{x}} = F(\mathbf{x}, t; \epsilon), \quad \text{where } \mathbf{x} \in U \subset \mathbb{R}^n, \quad t, \epsilon \in \mathbb{R}. \quad (2.5)$$

where F is periodic in time t ; that is, there exists a minimal period T such that $F(\mathbf{x}, t; \epsilon) = F(\mathbf{x}, t + T; \epsilon)$ for all t , and ϵ is a perturbation parameter such that $F(\mathbf{x}, t; \epsilon) \rightarrow f(\mathbf{x})$ as $\epsilon \rightarrow 0$, where f is an autonomous system. A special form of $F(\mathbf{x}, t; \epsilon)$ is $f(\mathbf{x}) + g(\mathbf{x}, t; \epsilon)$, where $g(\mathbf{x}, t; \epsilon) \rightarrow 0$ as $\epsilon \rightarrow 0$.

In a periodically-perturbed system, we can define the *phase* as $\theta = \omega t \bmod 2\pi$, where $\omega = 2\pi/T$. The system can then be written in autonomous form,

$$\begin{aligned}\dot{\mathbf{x}} &= F(\mathbf{x}, \theta; \epsilon), \\ \dot{\theta} &= \omega.\end{aligned}\tag{2.6}$$

where we note that time has been turned into a cyclic variable, $\theta \in S^1$.

2.3.2 Flow maps

Consider an arbitrary trajectory of the system (2.5) with initial condition $\mathbf{x}(t_0) = \mathbf{x}_0$. Define the corresponding flow map, $\phi(\cdot)$, as,

$$\mathbf{x}(t_0) \mapsto \mathbf{x}(t) = \phi(t, t_0; \mathbf{x}_0).\tag{2.7}$$

Consider the family of time- T *stroboscopic* maps $P_{t_0} : U \rightarrow U$ defined as,

$$\mathbf{x}_0 \mapsto P_{t_0}(\mathbf{x}_0) = \phi(t_0 + T, t_0; \mathbf{x}_0).\tag{2.8}$$

For a time-periodic Hamiltonian system, P_{t_0} is a symplectic, stroboscopic map of the phase space over one period. It can equivalently be written with the parameter as the initial phase $\theta_0 = \omega t_0$ as P_{θ_0} . Note that $P_{t_0}(\mathbf{x}_0)$ has an inverse,

$$\mathbf{x}_0 \mapsto P_{t_0}^{-1}(\mathbf{x}_0) = \phi(t_0 - T, t_0; \mathbf{x}_0).\tag{2.9}$$

2.3.3 State transition and monodromy matrices

The state transition matrix $\Phi(t, t_0; \mathbf{x}_0)$ linearly approximates the flow map, $\phi(t, t_0; \mathbf{x}_0)$. That is, it maps how trajectories slightly displaced from a reference trajectory $\bar{\mathbf{x}}(t)$ evolve from time t_0 to t . For simplicity of notation, the dependence of the state transition matrix on its initial condition $\mathbf{x}_0 = \bar{\mathbf{x}}(t_0)$ is suppressed. For (2.5), $\Phi(t, t_0)$ is the solution to the initial value problem

$$\dot{\Phi}(t, t_0) = DF(\bar{\mathbf{x}}(t), t; \epsilon)\Phi(t, t_0), \quad \Phi(t_0, t_0) = I_n, \quad (2.10)$$

where I_n is the $n \times n$ identity matrix and DF is the Jacobian of F .

For a periodic orbit, the *monodromy matrix* is,

$$\mathbf{M}_{\theta_0} = \Phi(t_0 + T, t_0), \quad (2.11)$$

which maps small initial displacements from the periodic orbit at phase θ_0 (initial time t_0) to their resulting displacement after one period [100]. For Hamiltonian systems, the monodromy matrix defines a linear symplectic map [101].

2.3.4 Lagrange periodic orbits replace Lagrange points

In perturbed systems where the perturbation is time-periodic and sufficiently small, equilibrium points are expected to bifurcate to periodic orbits. This result follows from the Averaging Theorem [93]. The Lagrange points of the CR3BP consequently bifurcate into periodic orbits in the presence of periodic perturbations. These periodic orbits, because they dynamically replace the Lagrange points, by definition form a class of Lagrange manifolds. The behavior near a Lagrange point is determined via linearization of the continuous differential equations. By contrast, the behavior near a *Lagrange periodic orbit* is determined via monodromy matrix calculation, which yields a discrete linear map.

A Lagrange periodic orbit has the same period as the perturbation. We can compute a Lagrange periodic orbit by solving a zero-finding problem: choose $\bar{\mathbf{x}}$ that minimizes the quantity $|\bar{\mathbf{x}} - P_0(\bar{\mathbf{x}})|$ to within a certain tolerance (where for convenience we choose the zero phase map, P_0). For example, an optimization method was used to find the Earth-Moon L_1 Lagrange periodic orbit in the elliptic problem (Section 6).

To obtain periodic orbits with arbitrary perturbation sizes, we can combine this methodology with continuation. By artificially decreasing the magnitude of the perturbation to nearly zero, calculating the Lagrange manifold using the approach described, and then increasing the magnitude of the perturbation slightly and using the previous initial condition as an initial guess, it is possible to “continue” the Lagrange periodic orbit out of the Lagrange point (see Appendix D for an example in the elliptic problem).

Unlike as in the elliptic problem, our initial condition for the bicircular problem was obtained via personal communication with the authors of [52], who utilized a multiple-shooting and continuation method.

Example initial conditions are given in Appendix B.

2.4 Linear 4D symplectic map near elliptic-hyperbolic point

2.4.1 Definitions

Suppose a fixed point of the time- T map P_0 has been identified and it is of elliptic-hyperbolic type, corresponding to a periodic orbit of saddle-center type of period T of a T -periodic 2 degree of freedom Hamiltonian system. Let $\mathbf{x} = (q_1, p_1, q_2, p_2)$ denote the displacement from the fixed point within the domain of the map P_0 . The linearization of P_0 about the fixed point (i.e., the monodromy matrix) can be put into a symplectic eigenbasis. Suppose

that (q_1, p_1, q_2, p_2) are coordinates with respect to this symplectic eigenbasis, where the first canonically conjugate coordinate pair (q_1, p_1) corresponds to the hyperbolic (or saddle) directions and the second canonically conjugate coordinate pair (q_2, p_2) corresponds to the elliptic (or center) directions. In other words, the dynamics for small \mathbf{x} are given by a linear 4-dimensional symplectic map,

$$\mathbf{x} \mapsto \mathbf{\Lambda} \mathbf{x} \tag{2.12}$$

where $\mathbf{\Lambda}$ is a symplectic matrix of the block diagonal form,

$$\mathbf{\Lambda} = \begin{bmatrix} \sigma & 0 & 0 & 0 \\ 0 & \sigma^{-1} & 0 & 0 \\ 0 & 0 & \cos \psi & \sin \psi \\ 0 & 0 & -\sin \psi & \cos \psi \end{bmatrix}, \tag{2.13}$$

for $\sigma > 1$ and for some $\psi \in S^1$.

2.4.2 The effective quadratic Hamiltonian

Proposition 2.1. The discrete map $\mathbf{x} \mapsto \mathbf{\Lambda} \mathbf{x}$ is identical to the time- T map of the linear Hamilton's canonical equations generated by an *effective* quadratic Hamiltonian,

$$\tilde{H}_2 = \tilde{\lambda} q_1 p_1 + \frac{1}{2} \tilde{\nu} (q_2^2 + p_2^2), \tag{2.14}$$

where,

$$\tilde{\lambda} = \frac{1}{T} \ln \sigma > 0, \quad \tilde{\nu} = \frac{1}{T} \psi > 0. \tag{2.15}$$

For the proof, see Appendix C.

2.4.3 Geometry of the linear map

Because \tilde{H}_2 is qualitatively identical to H_2 from (2.4), the solution geometry under Λ is qualitatively the same as a discrete time- T map of the dynamics near a collinear Lagrange point of the CR3BP. The primary difference in interpretation is that solutions are now discrete, but still belong to families of continuous curves in the saddle and center canonical projections, as shown in Figure 2.5. Note that the two canonical planes are uncoupled. All the qualitative results related to the four types of orbits from Section 2.2.5 carry over to the discrete case. In particular, hyperbolas in the saddle projection corresponding to transit and non-transit orbits can be identified.

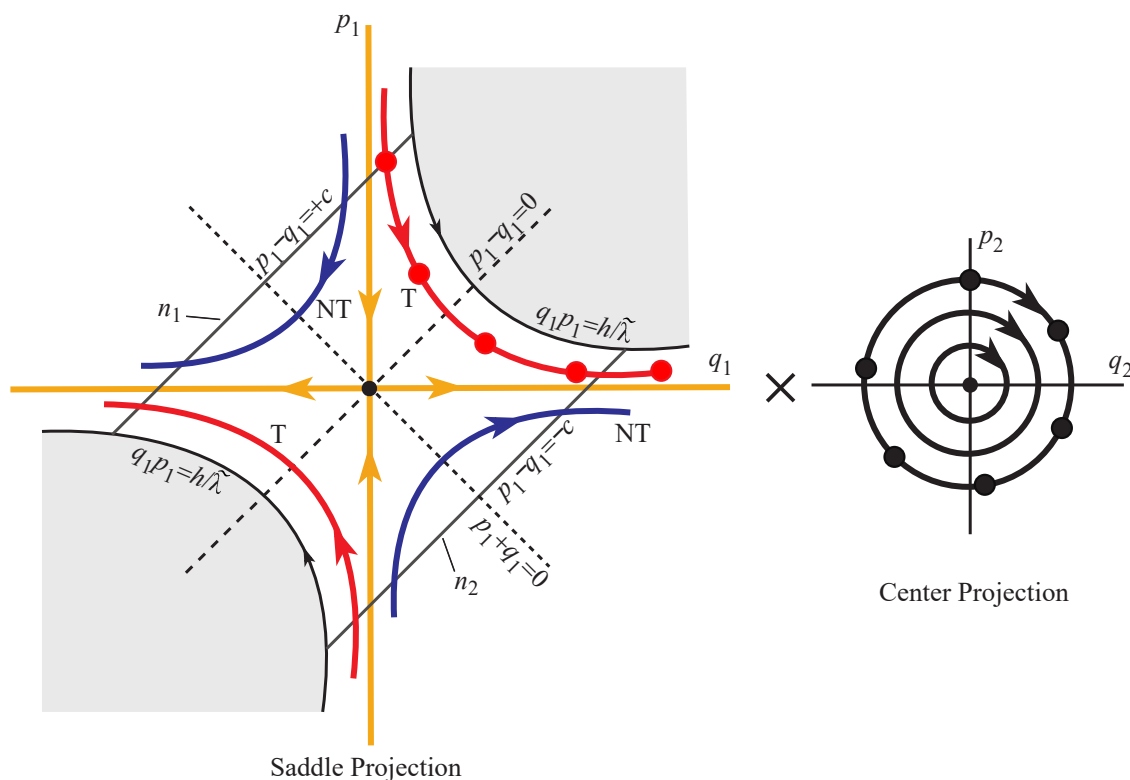


Figure 2.5: The two canonical planes of the dynamics under the mapping $\mathbf{x} \mapsto \Lambda \mathbf{x}$; the orbits here are discrete solutions of a map (represented as large dots in one of the transit curves) as compared to continuous orbits in Figure 2.4.

2.4.4 Topology of the equilibrium region of the map

In the saddle projection, the boundaries of the equilibrium region can be defined by the two intervals of initial conditions parallel to the $q_1 = p_1$ line that extends between the forbidden regions. Pick one of the bounding intervals, say, $p_1 - q_1 = c$, and consider the sub-interval that enters the equilibrium region under the forward mapping, as depicted in Figure 2.6. Each point along this sub-interval corresponds to a circle in the center projection. The structure of the effective quadratic Hamiltonian implies that, for the trajectory on the border of the forbidden region, the corresponding circle shrinks to a point [41]. The bounding sub-interval is consequently homeomorphic to a spherical hemisphere; that is, $S^2 \cap \mathcal{H}^3$, where \mathcal{H}^3 is the upper three-dimensional half-space with boundary. This analysis also holds for those initial conditions that enter the region under the backward mapping, so the complete bounding interval in the saddle projection is given by S^2 . Because the distance between the bounding interval and $q_1 = p_1$ is arbitrary, the entire equilibrium region is homeomorphic to $S^2 \times I$, where $I = [-c, c] \subset \mathbb{R}$ is an interval and $c > 0$ is as defined in Section 2.2.5.

The *McGehee representation* of the equilibrium region is informative for understanding the phase space structure of the unperturbed problem [102, 103, 104, 105, 106]. However, we can extend the McGehee representation to the perturbed problem in a straightforward manner, as depicted in Figure 2.7. The initial conditions along the boundaries of the equilibrium region that enter the region in forward time are highlighted. For example, along the outermost bounding sphere, n_1 (following the terminology of [102] and [104]), the spherical cap of transit orbits is Γ_T^1 and the spherical band of non-transit orbits is Γ_{NT}^1 . The point C which separates Γ_T^1 and Γ_{NT}^1 is on an orbit to an invariant circle in the equilibrium region (i.e., a quasi-periodic orbit in the full system). The image of Γ_T^1 and Γ_{NT}^1 under the forward stroboscopic map P_0 is shown schematically.

Although transit initial conditions must eventually transit, they may or may not reach the

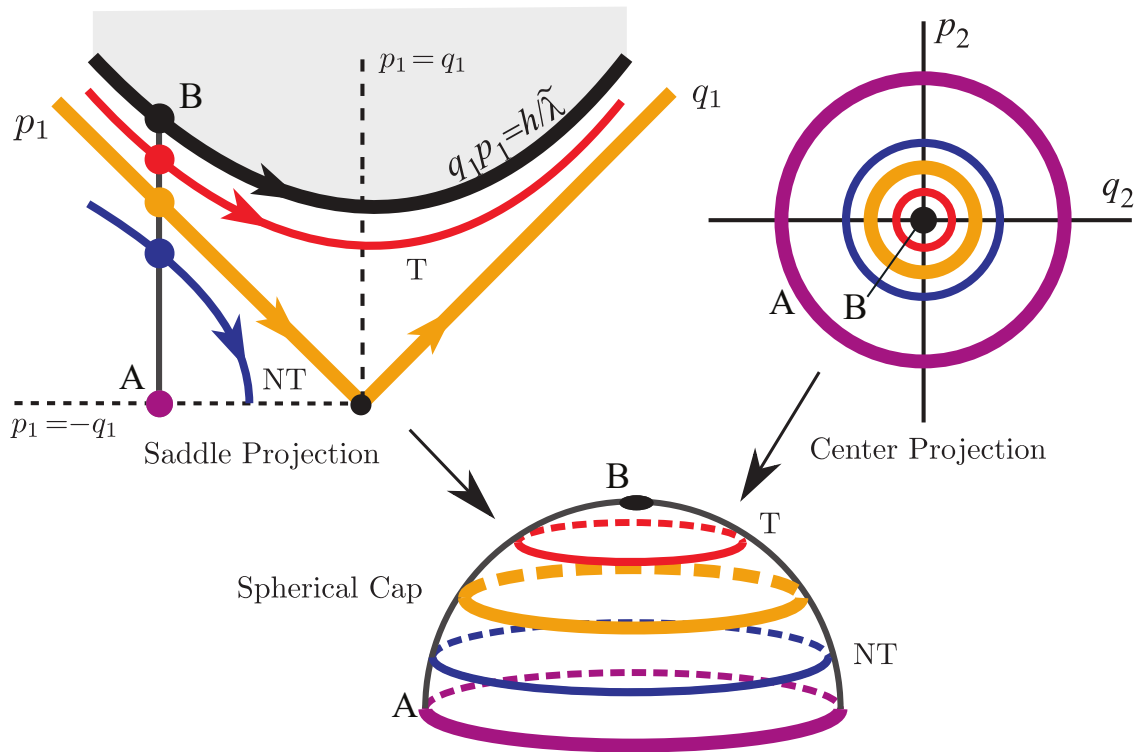


Figure 2.6: Construction of a hemisphere bounding the equilibrium region of the map, along an energy manifold of energy h : each point along the bounding line \overline{AB} in the saddle projection corresponds to the circle of initial conditions in the center projection of the same color, shrinking to a point at B .

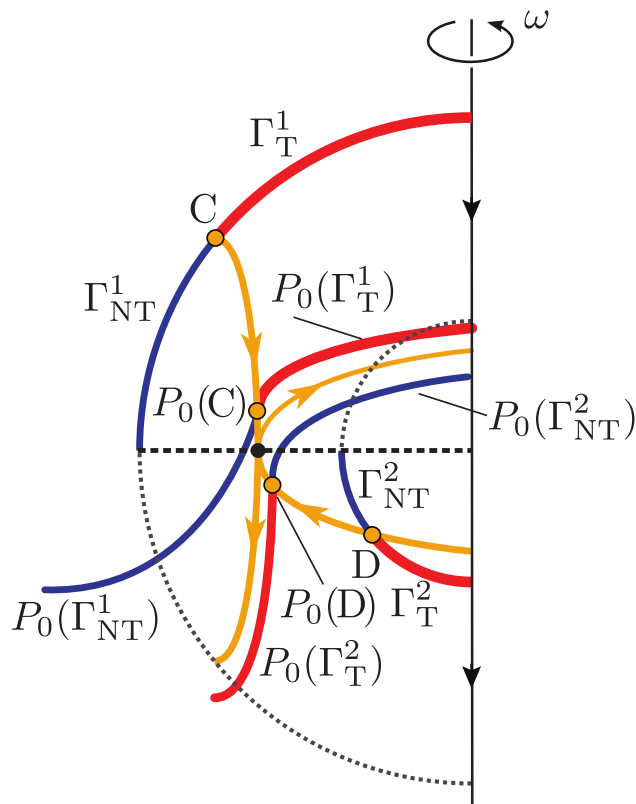


Figure 2.7: The McGehee representation of the discrete dynamics in the equilibrium region of the map on a fixed energy shell is obtained by rotating this diagram one revolution about the ω axis. The red lines correspond to iterates of the transit conditions under the stroboscopic map P_0 ; the blue lines correspond to iterates of the non-transit conditions; the orange lines correspond to the stable and unstable manifolds under the quadratic Hamiltonian. The black point corresponds to an invariant circle of the map of energy h , analogous to a Lyapunov orbit of energy h in the unperturbed case.

other bounding sphere, n_2 , after a single iteration of the map P_0 , depending on their initial proximity to the stable manifold. Those points closest to the stable manifold will take the largest number of iterates to transit; a discrete-time analogy to a result obtained previously (see, e.g., [104]). Non-transit initial conditions may similarly fail to leave the equilibrium region after a single iteration. Thus, the transit and non-transit sets undergo stretching under the stroboscopic map.

2.4.5 Connection with Lagrange periodic orbits

A T -periodic Hamiltonian perturbation of the CR3BP will give rise to a Lagrange periodic orbit of period T of saddle-center type. Therefore, the geometry at each phase will follow the geometry given above, including in the *full nonlinear map* of the motion [92].

Thus, *the CR3BP perturbed by a periodic Hamiltonian perturbation will have the transit structure described herein*. Below, we consider two particular examples: the bicircular problem (which includes the effect of an additional mass) and the elliptic restricted three-body problem.

2.5 Transit orbits in the bicircular problem

2.5.1 Equations of motion of the BCP

The bicircular problem (BCP) is a generalization of the CR3BP that describes the motions of four gravitationally interacting bodies m_0 , m_1 , m_2 , and m_3 where $m_2 < m_1$ and where m_3 has negligible mass. In the inertial frame, m_1 and m_2 trace circular orbits around their center of mass O ; similarly, m_0 and O trace circular orbits around their common center of mass [38, 39]. The equations of motion are written in the CR3BP rotating reference frame so that m_1 and m_2 are still fixed. The large mass m_0 is not fixed in the rotating frame but appears to trace a circle around O (see Figure 2.2).

The non-dimensional equations of motion for m_3 in the BCP are, unlike the equations of motion for the CR3BP, specifically time-periodic [3]. They are Hamilton's canonical equations for a Hamiltonian,

$$H_{\text{BCP}} = H_{\text{CR3BP}} + H_{m_0}(t), \quad (2.16)$$

where the time-dependent perturbation is,

$$H_{m_0}(t) = \frac{\mu_0}{a_0^2} \left(x \cos \theta_{m_0}(t) + y \sin \theta_{m_0}(t) \right) - \frac{\mu_0}{r_0(t)} \quad (2.17)$$

where,

$$\begin{aligned} r_0(t)^2 &= (x - a_0 \cos \theta_{m_0}(t))^2 + (y - a_0 \sin \theta_{m_0}(t))^2, \\ \theta_{m_0}(t) &= -\omega_{m_0} t + \theta_{m_0 0} \end{aligned} \quad (2.18)$$

where μ_0 , a_0 , ω_{m_0} , θ_{m_0} , $\theta_{m_0 0}$, and r_0 are the mass, distance, angular velocity, current angle, initial angle of m_0 , and distance from the particle, respectively, in non-dimensional units. The period of m_0 about the origin is $T = 2\pi/\omega$ where the frequency is $\omega = \omega_{m_0}$ for this system. Note that the resulting equations of motion are of the form (2.5) where μ_0 corresponds to ϵ . This model has been used to model a small celestial body or spacecraft (m_3) in the gravity field of the Earth (m_1) and Moon (m_2) when perturbed by the effect of the Sun (m_0) [39]. The parameters in this case are $\mu = 0.01215$, $\mu_0 = 328900.54$, $a_0 = 388.81114$, and $\omega_{m_0} = 0.925195985520347$ in non-dimensional units.

The BCP reduces to the CR3BP when gravitational perturbations from m_0 are negligible; that is, when the terms due to m_0 go to zero, which occurs when $\mu_0 \rightarrow 0$ or when $a_0 \rightarrow \infty$. The CR3BP also approximates the BCP when $\omega_{m_0} \rightarrow \infty$ as the perturbation averages out for sufficiently large angular velocity.

2.5.2 The instantaneous Lagrange points

As discussed previously, the perturbation from m_0 fundamentally removes the equilibrium points (see Figure 2.8). Because the BCP is non-autonomous, the vector field associated with the equations of motion varies with t or, equivalently, θ_{m_0} . Setting the right side of the

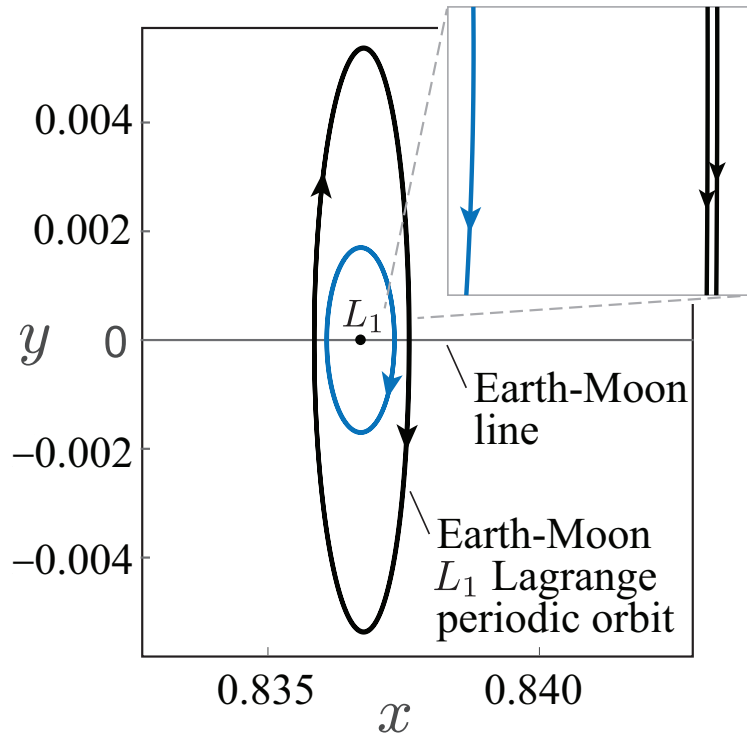


Figure 2.8: The BCP Earth-Moon L_1 periodic orbit (black) compared with the path (in blue) traced by the instantaneous zero, or stagnation point, of the BCP vector field. The former is a trajectory; the latter is not. Both have doubly-looping structures over a single period of the perturbation, but at the resolution shown, even in the inset, only the periodic orbit's two loops are visible.

BCP equations of motion to zero yields an instantaneous zero of the vector field that varies with the independent variable, tracing out a path that repeats every 2π in the Sun angle θ_{m_0} . Such points are not equilibria, and this path is *not* a trajectory; particles with initial conditions along it diverge quickly. One must consider the Lagrange periodic orbit which dynamically replaces the Lagrange point.

2.5.3 Dynamics near the Sun-perturbed Earth-Moon BCP L_1 Lagrange periodic orbit

The initial condition of the Sun-perturbed Earth-Moon BCP's L_1 Lagrange periodic orbit can be found numerically using a zero-finding procedure [107, 52]; the numerical values are given in Appendix B. Figure 2.8 depicts its path in position space. The eigenvalues of the monodromy matrix from 0 to T are of the elliptic-hyperbolic form given previously, with $\sigma = 4.2874 \times 10^8$ and $\psi = 3.0273$. Note that the monodromy matrix could be calculated starting at a different initial phase.

The monodromy matrix of the Lagrange periodic orbit from 0 to T can be transformed into its symplectic eigenbasis, which is in the form of (2.13). As a result, we can construct initial conditions that are transit or non-transit between the Earth and Moon realms when integrated in the full nonlinear equations of motion with Hamiltonian (2.16). In Figure 2.9(a), the black hyperbola represents the calculated boundary of the forbidden realm, as shown schematically in Figure 2.5; the red line contains initial conditions that should transit whereas the blue line are initial conditions that should not transit. In Figure 2.9(b), the corresponding red trajectories are transit orbits, starting in the Moon realm and going to the Earth realm, whereas the blue trajectories are non-transit orbits. Trajectories going from the Earth realm to Moon realm could just as easily be constructed by starting on the other boundary, n_2 , instead of n_1 .

The spherical cap of transit orbits (labeled Γ_T) in the bicircular model is mapped forwards and backwards for one period in Figure 2.10. Under the stroboscopic map P_0 , the set undergoes considerable distortion, but the topology, which is equivalent to that of a spherical cap, is still preserved. This setup is analogous to the description of Poincaré section transit orbit intersections previously computed in the Earth-Moon CR3BP [27, 108].

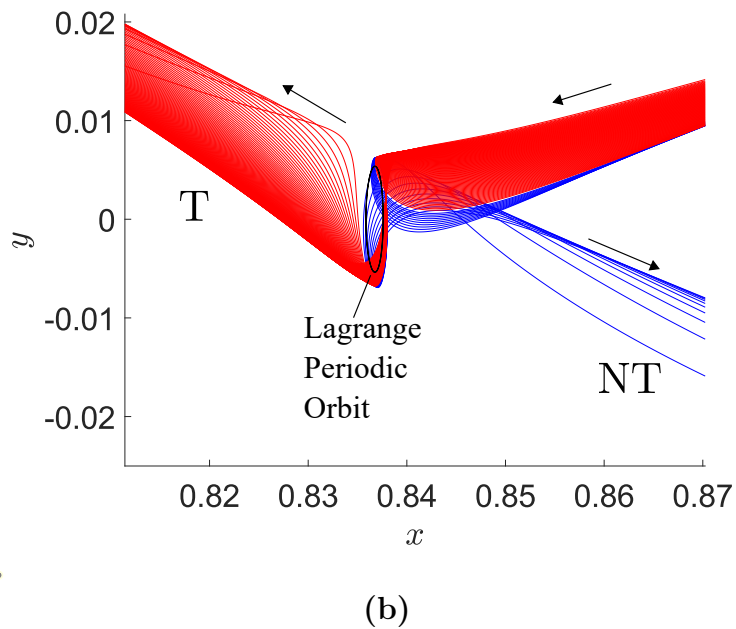
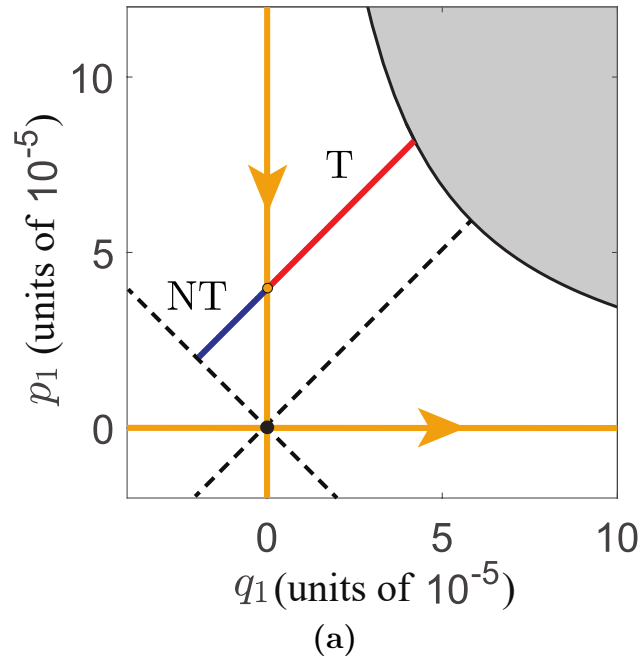


Figure 2.9: (a) Numerically determined initial conditions for transit and non-transit orbits found by looking in the q_1 - p_1 saddle canonical plane at initial phase $\theta = 0$. $\tilde{H}_2 = 10^{-6}$ and $c = 10^{-4}$. Compare with schematic shown in Figure 2.5. (b) The initial conditions integrated in the full equations of motion showing transit and non-transit behavior. Please refer to the online version of this article relating to color.

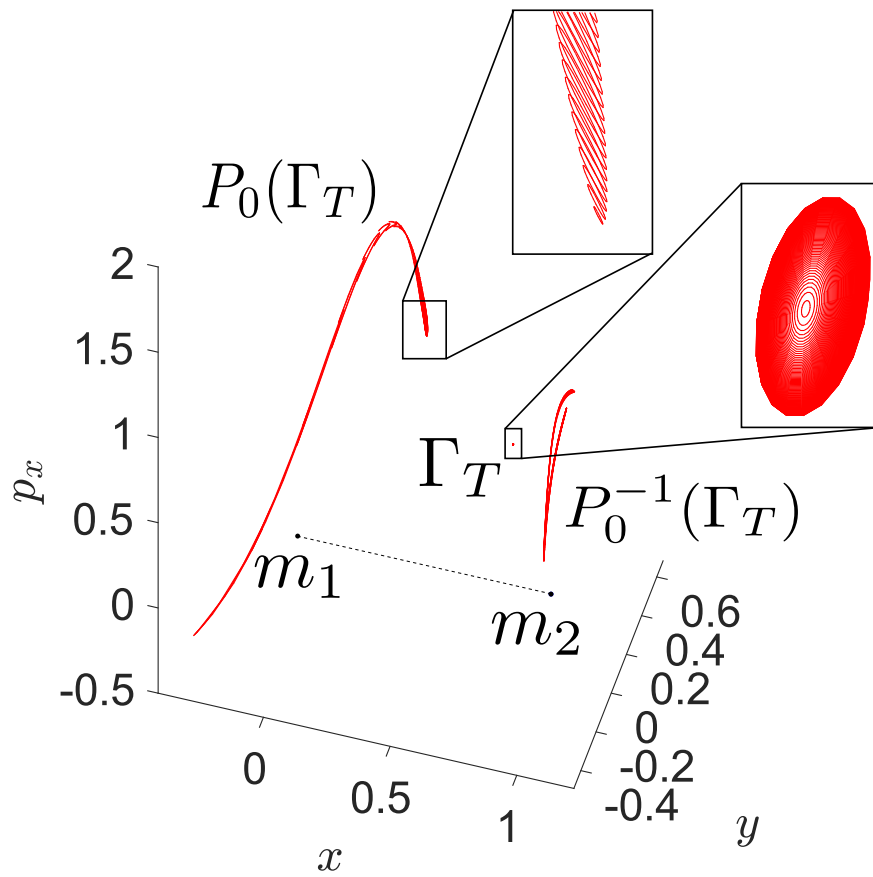


Figure 2.10: The spherical cap of transit orbits, Γ_T , is mapped forwards and backwards in the bicircular model and then projected into x - y - p_x space.

2.6 Transit orbits in elliptic restricted three-body problem

2.6.1 Equations of motion in the ER3BP

The elliptic restricted three-body problem (ER3BP) is a generalization of the CR3BP that drops the restriction that m_1 and m_2 move on circular orbits about their barycenter [40, 4]. Instead, m_1 and m_2 move in more realistic elliptical orbits around their center of mass O . We write the equations of motion in the rotating reference frame which rotates uniformly with the mean angular motion ($\omega = 1$); that is, we utilize the same rotating frame as used for the CR3BP. Most authors analyzing this system utilize a “pulsating” coordinate system [40, 56], which we have chosen not to do despite the considerable utility of this coordinate system; our aim is to bring about the commonalities of both the ER3BP and BCP and to provide ourselves with a useful toy model for our analysis.

Due to non-zero eccentricity, in this frame, m_1 and m_2 move periodically about their CR3BP locations; their movements are given by the true anomaly φ of the system as a function of time (see Figure 2.2 for the geometry). The equations of motion are Hamilton’s canonical equations with Hamiltonian,

$$H_{\text{ER3BP}} = \frac{1}{2}(p_x^2 + p_y^2) - xp_y + yp_x - \frac{\mu_1}{r_1(t)} - \frac{\mu_2}{r_2(t)}, \quad (2.19)$$

where the same non-dimensional units as in the CR3BP are used. Compared to the circular

problem Hamiltonian, (2.1), the distances r_i are now explicit functions of time,

$$r_i^2(t) = \left| \left(\begin{bmatrix} x \\ y \end{bmatrix} + \frac{1 - \mu_i}{1 + e \cos \varphi(t)} \mathbf{R}(t) \begin{bmatrix} \cos \varphi(t) \\ \sin \varphi(t) \end{bmatrix} \right) \right|^2, \quad (2.20)$$

with $\mathbf{R}(t) = \begin{bmatrix} \cos t & \sin t \\ -\sin t & \cos t \end{bmatrix}$,

where $\varphi(t)$ is the solution to the differential equation,

$$\dot{\varphi} = \frac{(1 + e \cos \varphi)^2}{(1 - e^2)^{3/2}}, \quad (2.21)$$

with initial condition $\varphi(0) = \varphi_0$. For the Earth-Moon system, we use $e = 0.0549006$. Using the mean anomaly as the phase θ , the equations of motion are of the form (2.5) with $T = 2\pi/\omega = 2\pi$ and with e corresponding to ϵ . Note that H_{ER3BP} from (2.19) becomes H_{CR3BP} from (2.1) as $e \rightarrow 0$.

2.6.2 Dynamics near the Earth-Moon ER3BP L_1 Lagrange periodic orbit

The initial condition of the Earth-Moon eccentric problem's L_1 Lagrange periodic orbit, obtained via a zero-finding algorithm (section 2.3.4), is given in Appendix B. Figure 2.11 depicts its path in position space. We show the BCP L_1 manifold for comparison, which is an order of magnitude smaller in amplitude.

The eigenvalues of the monodromy matrix from 0 to T are of the elliptic-hyperbolic form given in Section 2.4.1, with $\sigma = 8.3659 \times 10^7$ and $\psi = 1.9863$. Constructing a symplectic eigenbasis from the monodromy matrix yields initial conditions that transit or fail to transit between the Earth and Moon realms when integrated in the full nonlinear equations of

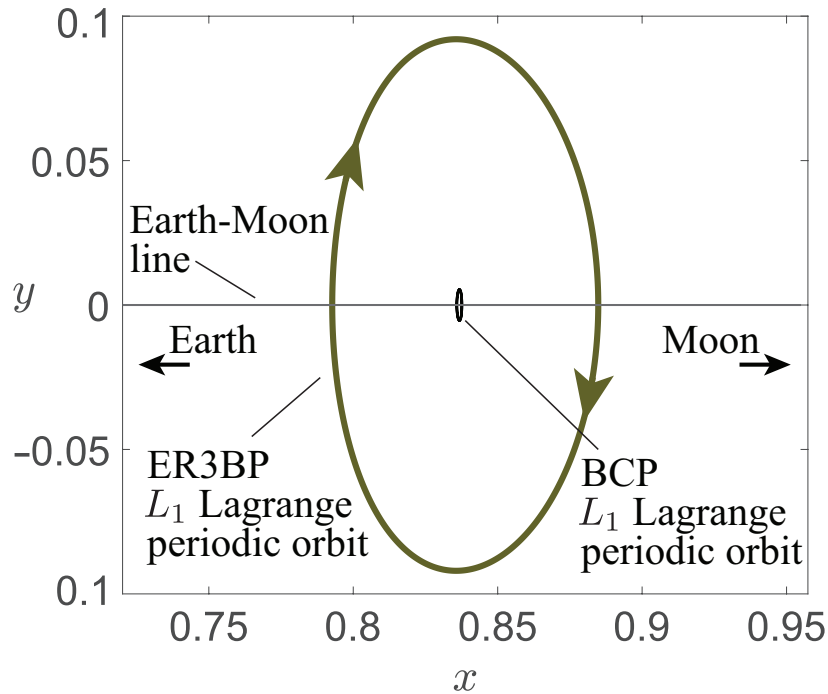


Figure 2.11: The ER3BP Earth-Moon L_1 periodic orbit (large, dark green) and the BCP L_1 periodic orbit (black) in the position space (average rotating frame, CR3BP coordinates). The ER3BP L_1 periodic orbit is singly-looping, not doubly-looping as in the BCP.

motion—that is, Hamilton’s canonical equations with Hamiltonian H_{ER3BP} given in (2.19). In Figure 2.12(a), the black hyperbola represents the calculated boundary of the forbidden realm in the saddle projection. The red line corresponds to initial conditions, Γ_{T} , that should transit whereas the blue line is initial conditions that should not transit, Γ_{NT} . In Figure 2.12(b), the trajectories in the full equations of motion are shown. As expected, the red trajectories are transit orbits, starting in the Moon realm and going to the Earth realm, whereas the blue trajectories are non-transit orbits.

Although we have shown examples of systematically finding transit and non-transit orbits for the BCP and the ER3BP at a single phase in the periodic perturbation, the method works equally well at other phases. We illustrate this at two additional initial phases for the initial conditions in parts (c) and (d) of Figure 2.12 for the ER3BP.

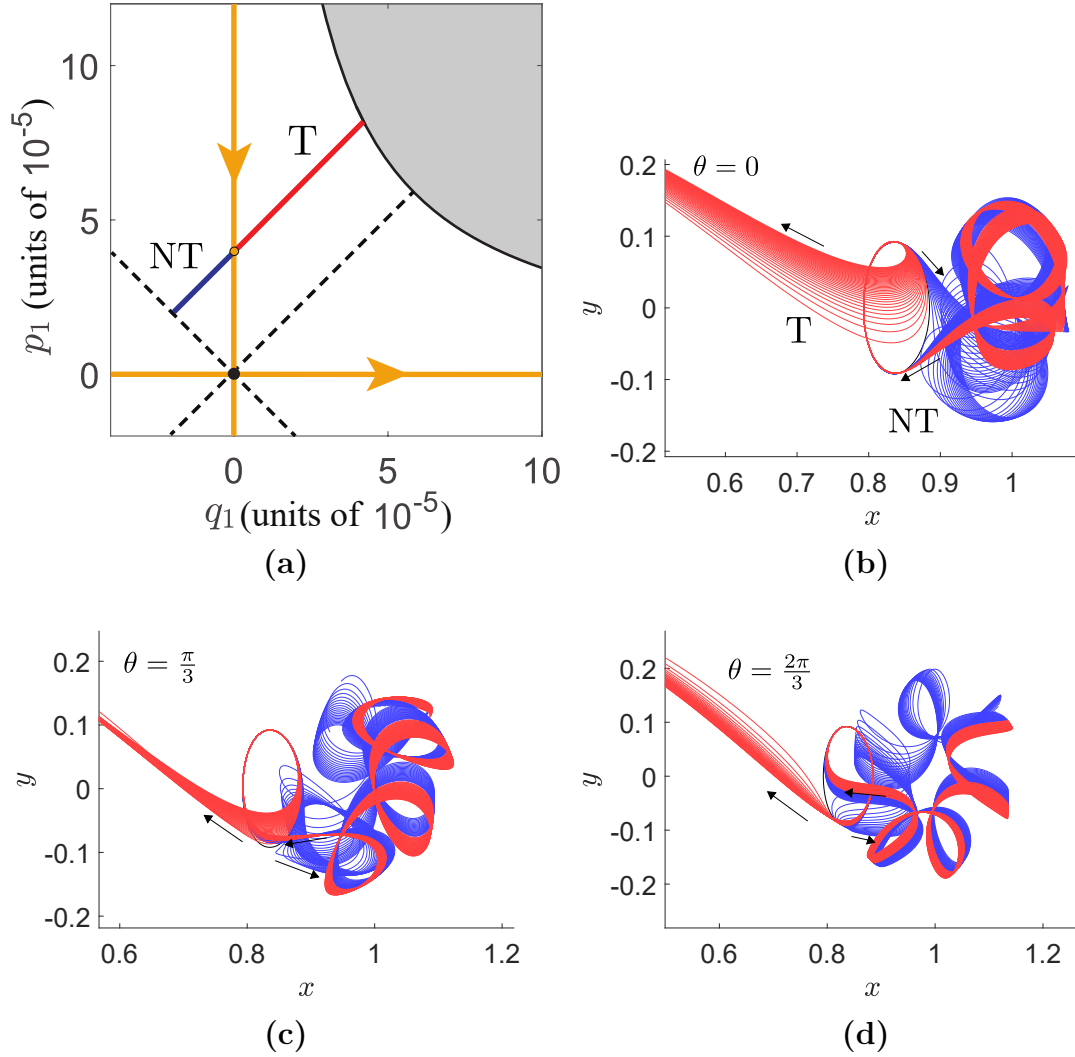


Figure 2.12: (a) Initial conditions for transit and non-transit orbits found by looking in the q_1 - p_1 saddle canonical plane in the symplectic eigenbasis. $\tilde{H}_2 = 10^{-8}$ and $c = 4 \times 10^{-5}$. (b) The initial conditions integrated backwards and forwards in the full equations of motion, as shown, starting at phase (mean anomaly) $\theta = 0$. (c) The initial conditions from part (a) integrated backwards and forwards in the full equations of motion for $\theta = \frac{\pi}{3}$. Note that the transit theory still holds at a different phase. (d) The integrated initial conditions for $\theta = \frac{2\pi}{3}$.

2.7 Discussion and conclusion

We demonstrate that the linear dynamics corresponding to transit and non-transit behavior in T -periodically-perturbed versions of the circular restricted three-body problem can be

reduced to a linear time- T map with the same orbit geometry as is now well-known in the CR3BP, going back to Conley and McGehee [17, 102]. Dynamically replacing the index-1 Lagrange equilibrium point of the autonomous system is a period- T Lagrange periodic orbit, analyzed via a time- T stroboscopic Poincaré map. In the phase space of the map, the Lagrange periodic orbit corresponds to an index-1 fixed point, or elliptic-hyperbolic point. As we consider only the planar (two degree of freedom) problem, the Lagrange periodic orbit has a 2-dimensional center manifold, 1-dimensional stable manifold, and 1-dimensional unstable manifold.

In the extended phase space of the perturbed models (that is, including the phase of the perturbation, or cyclic time), the transit and non-transit orbits form open sets bounded by the stable and unstable manifolds to the Lagrange periodic orbit. These results carry over to the full nonlinear system, where the linear symplectic map near the Lagrange periodic orbit is replaced by the full nonlinear symplectic map.

Moreover, a method for elucidating the geometry of transit orbits in generalizations of the circular restricted three-body problem experiencing periodic perturbations is given. The Conley-McGehee representation is re-interpreted in terms of a discrete mapping rather than continuous dynamics (in Section 2.4). The theory was demonstrated in two examples of perturbed models: the bicircular problem and the elliptic restricted three-body problem.

We illustrated our results by considering transit orbits near the Earth-Moon L_1 cislunar point, the most easily accessible Lagrange point from Earth and a likely focus for future space endeavours [96, 82, 98, 109, 110]. Cislunar space also has significant natural connections to the Sun-Earth L_1 and L_2 regions [97, 27], which can be explored using geometric techniques rather than less direct, optimization-based approaches [111, 85, 112].

We believe that the results herein contribute significantly to the state-of-the-art in the literature. As implied in the introduction to this paper, exploring the dynamical properties of perturbations of the CR3BP has lately become a popular area of investigation in astro-

dynamics (refer to [52, 9, 64, 53] for just a few recent examples). This study, by outlining a simple and straightforward method for delineating transit and nontransit behavior within perturbed models, elegantly fills an important niche in this emerging topic.

This paper also suggests a much more general discovery with ramifications beyond astrodynamics: that *manifold-based transit phenomena are robust under time-periodic perturbation*. Recent scholarship has determined that manifold-based transit phenomena are also robust under dissipation [41, 43]. These two discoveries together help to demonstrate rigorously that natural systems subject to perturbation can exhibit the behaviors predicted by idealized tube-manifold models.

We also believe that the work herein will have useful real-world applications. Existing integrated frameworks for low-energy trajectory design utilize the dynamical characteristics of the circular restricted three-body problem [3]. As shown in this paper, however, the effects of perturbations can be very large from a qualitative perspective and can permit the design of unique mission architectures that arise from the specific dynamical characteristics of perturbed models. For example, the diagrams in Sections 5 and 6 demonstrate that transit orbits “wind” on and off of the Lagrange manifolds in a way that might have practical navigational utility.

There are several potential avenues for further investigation. This study only considered one possible topological class of Lagrange manifolds, periodic orbits generated by a single periodic perturbation. Additional perturbations will lead to additional bifurcations in the topology of the Lagrange point dynamical replacement (see Figure 2.1). For instance, quasi-periodic Lagrange manifolds in systems with two or more perturbations of incommensurate period will generate hyperbolic structures controlling transit [94, 113, 52].

Another possibility for further study involves combining periodic perturbations with general non-conservative (e.g., dissipative, solar sail) effects [114, 41]. Our approach is applicable to the geometry of transition dynamics in other periodically-perturbed (or driven) systems

governed by Hamiltonian dynamics, including chemical systems, ship dynamics, solid state physics, and structural systems [43, 115, 114, 116].

Acknowledgments

This work was supported in part by the National Science Foundation under awards 1537349 and 1821145. J.F. was supported by a Virginia Space Grant Consortium Graduate Research Fellowship. The authors would like to thank Angel Jorba and Jose Rosales for providing an initial condition for the periodic orbit dynamical replacement to L_1 in the bicircular problem.

Chapter 3

State transition tensors and the nonlinear transit geometry of the periodically-perturbed restricted three-body problem

Attribution

This chapter, a collaborative work with Shane Ross, has not yet been published.

Author Contributions

Fitzgerald and Ross conceived of the project. Fitzgerald developed the underlying mathematical model and software, derived the analytical expressions and proofs, implemented the numerical simulations, and analyzed the simulation output with supervisory assistance from Ross. Fitzgerald produced almost all figures, and the remainder were adapted by Fitzgerald from earlier work by Ross. Fitzgerald wrote most of the manuscript with some assistance by Ross. Fitzgerald coordinated the revisions.

3.1 Introduction

The phase space of the circular restricted three-body problem (CR3BP) is filled with a complicated assemblage of invariant manifolds that guide bodies throughout the system [17, 15, 87, 11, 90, 85, 110, 83, 74, 86, 117]. Recent work has generalized the existing theory of invariant manifolds in the CR3BP to models constructed as time-periodic perturbations of the standard problem [52, 109, 49, 118, 119]. In particular, it was demonstrated that the basic phase space transit structure associated with the Lagrange points, which dominates the dynamics at low energies in the CR3BP, persists under periodic perturbation. Perturbation transforms the Lagrange points into higher dimensional invariant objects called *Lagrange manifolds* which, in the case of a single, time-periodic perturbation force, are diffeomorphic to S^1 and so are called *Lagrange periodic orbits* (see Figure 3.1). When the system is viewed using a stroboscopic map of the same period as the perturbation, the Lagrange periodic orbit becomes a fixed point, and a first-order analysis reveals that the transit geometry is a discrete version of that from the unperturbed case [120].

Although the first-order analysis yields an accurate picture of the global transport structure for very small displacements from Lagrange periodic orbits, for practical mission design applications it would be useful to consider larger displacements—but at larger displacements, nonlinear effects contribute to the dynamics, and so the simple, elegant framework provided by the linear theory becomes considerably messier.

In this study, we broaden the theory to quadratic and higher orders using *state transition tensors*, generalizations of state transition tensors which encode the higher order dynamics of displacements along a reference trajectory. Instead of a linear map approximating trajectories near the Lagrange periodic orbit, we obtain a quadratic map, although the theory generalizes to higher orders in straightforward fashion. We then outline and test a method for coupling this quadratic map with the linear eigenbasis to calculate a more accurate boundary between

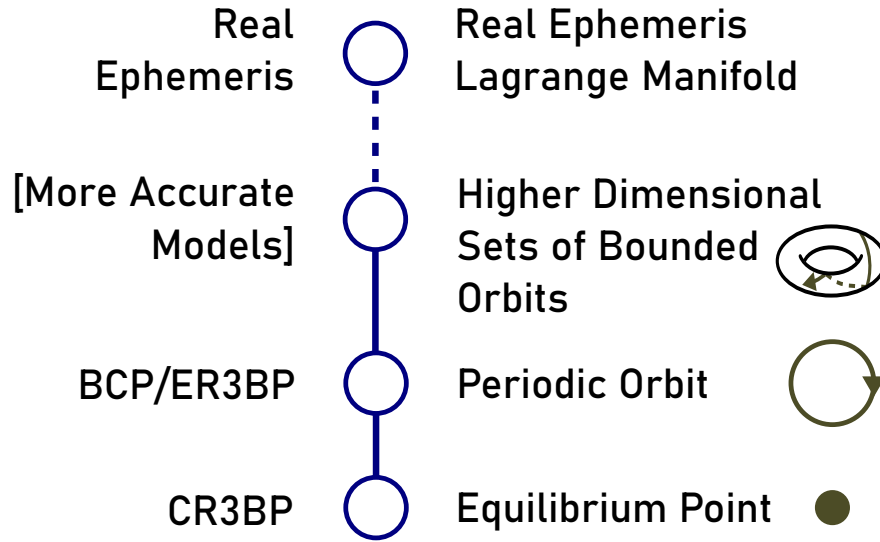


Figure 3.1: Schematic of the sequence of Lagrange manifolds that “links” the transit structure of the CR3BP with the full ephemeris. As additional perturbation forces are added to the system, the dimension and topological complexity of the Lagrange manifold correspondingly increases.

transit and nontransit orbits.

This paper is organized as follows. Section 3.2 introduces the mathematical and theoretical foundations of the rest of the paper, namely periodically-perturbed dynamical systems, flow maps, and state transition tensors. Section 3.3 reviews the linear phase space transit structure for the periodically perturbed CR3BP. It also introduces the CR3BP itself as well as the two periodically perturbed models—the bicircular problem (BCP) and the elliptic restricted three-body problem (ER3BP)—employed in this study. Section 3.4 outlines the method used to investigate the phase space transit structure up to quadratic order, and Sections 3.5 and 3.6 apply this method to the BCP and ER3BP, respectively.

3.2 Periodically-perturbed systems and state transition tensors

3.2.1 Periodically-perturbed systems

Consider a non-autonomous, periodically perturbed dynamical system $F : M \rightarrow M$ on a smooth manifold M of the form

$$\dot{\mathbf{x}} = F(\mathbf{x}, t; \epsilon), \quad \text{s.t. } \mathbf{x} \in U \subset \mathbb{R}^n, \quad t, \epsilon \in \mathbb{R}. \quad (3.1)$$

F is periodic in the time variable t with period T so that $\forall t \in \mathbb{R} \ F(\mathbf{x}, t; \epsilon) = F(\mathbf{x}, t+T; \epsilon)$, and also $F(\mathbf{x}, t; \epsilon) \rightarrow f(\mathbf{x})$ as $\epsilon \rightarrow 0$, where f is an autonomous system and ϵ is the *perturbation parameter*.

The *phase* θ of a periodically-perturbed system is given by $\theta = \omega t \bmod 2\pi$, where $\omega = 2\pi/T$.

3.2.2 Flow maps

Consider the system (3.1). The corresponding flow map, $\phi : \mathbb{R} \times \mathbb{R} \times M \rightarrow M$, transports points from time t^o to time t so that

$$\mathbf{x}(t^o) \mapsto \mathbf{x}(t) = \phi(t, t^o; \mathbf{x}^o) \quad (3.2)$$

where $\mathbf{x}(t^o) = \mathbf{x}^o$ is an initial condition.

Define the family of time- T *stroboscopic maps* $P_{t^o} : M \rightarrow M$ as

$$\mathbf{x}^o \mapsto P_{t^o}(\mathbf{x}^o) = \phi(t^o + T, t^o; \mathbf{x}^o). \quad (3.3)$$

If (3.1) is Hamiltonian, then each P_{t^o} is a symplectic map.

3.2.3 State transition tensors

Summarizing the analysis in Park and Scheeres [121], we demonstrate how the flow map ϕ can be written as a Taylor series about a fixed trajectory.

Fix a reference trajectory with initial condition $\mathbf{x}(t^o) = \mathbf{x}^o$ and consider a small displacement $\mathbf{x}^o + \delta\mathbf{x}^o$ in the initial condition. The evolution of the displacement under the flow map is

$$\delta\mathbf{x}(t) = \phi(t, t^o; \mathbf{x}^o + \delta\mathbf{x}^o) - \phi(t, t^o; \mathbf{x}^o). \quad (3.4)$$

We can expand (3.4) about \mathbf{x}^o via a Taylor series. Employing the Einstein summation convention in order to simplify the notation, the result, written component-wise, is

$$\delta x_i(t) = \sum_{p=1}^m \frac{1}{p!} \Phi_{i, k_1 \dots k_p} \prod_{j=1}^p \delta x_{k_j}^o \quad (3.5)$$

where $k_j \in \{1, \dots, n\}$ and where

$$\Phi_{i, k_1 \dots k_p} = \frac{\partial^p x_i}{\partial x_{k_1}^o \dots \partial x_{k_p}^o}. \quad (3.6)$$

Φ with $p + 1$ indices represents the *state transition tensor of order p* , which we denote in a coordinate-free way by $\Phi^{(p)}$. The state transition tensor generalizes a more familiar concept, the state transition matrix, which corresponds to the case $p = 1$. The state transition matrix—a rank two tensor—encapsulates the linear, first-order behavior of small displacements from the reference trajectory, and similarly the state transition tensor of rank $p + 1$ encapsulates the nonlinear behaviors of order p of small displacements.

(3.5) is crucial to our analysis because it provides an analytical series expansion for the full nonlinear flow map. Previous work analyzed the transit structure of periodically perturbed models by approximating the stroboscopic map by calculating (3.5) about relevant Lagrange

periodic orbits, but restricted to $m = 1$ [120]. The current study will consider $m = 2$, which corresponds to approximating the stroboscopic map up to quadratic order, but the underlying method generalizes easily to any m .

A state transition matrix, when calculated for a periodic orbit over one period of the orbit, is called a *monodromy matrix*. By analogy, we will call state transition tensors calculated for a periodic orbit over one period *monodromy tensors*.

The linear and quadratic state transition tensors are calculated over a reference trajectory by integrating, simultaneously with the standard equations of motion,

$$\begin{aligned}\dot{\Phi}_{i,a} &= f_{i,\alpha}^* \Phi_{\alpha,a} \\ \dot{\Phi}_{i,ab} &= f_{i,\alpha}^* \Phi_{\alpha,ab} + f_{i,\alpha\beta}^* \Phi_{\alpha,a} \Phi_{\beta,b}\end{aligned}\tag{3.7}$$

for the initial conditions $\Phi_{i,a} = \delta_{ij}$ and $\Phi_{i,ab} = 0$. \mathbf{f}^* generalizes the Jacobian:

$$f_{i,k_1\dots k_p}^* = \left. \frac{\partial^p f_i}{\partial x_{k_1} \dots \partial x_{k_p}} \right|_{\mathbf{x}=\mathbf{x}^*}\tag{3.8}$$

where \mathbf{x}^* is the reference trajectory [121].

3.3 Linear transit geometry of the periodically perturbed three-body problem

3.3.1 Hierarchy of models

The circular restricted three-body problem

In order to understand the perturbed models of spacecraft motion used in this study, we must first consider the unperturbed model from which they are built: the circular restricted

three-body problem (CR3BP). To construct the CR3BP, consider a small particle m_3 with negligible mass. Place two point masses $m_1 > m_2$ in circular orbits around their common center of gravity, and let m_3 move under the resultant gravitational field. In this study, we only consider the planar CR3BP (PCR3BP), in which m_3 is confined to the plane of motion of m_1 and m_2 . We write the corresponding equations of motion in a rotating frame whose x -axis coincides with the m_1 - m_2 line and whose y -axis points towards the direction in which m_2 is moving. The origin O of this frame is the barycenter of the system (see Figure 3.2).

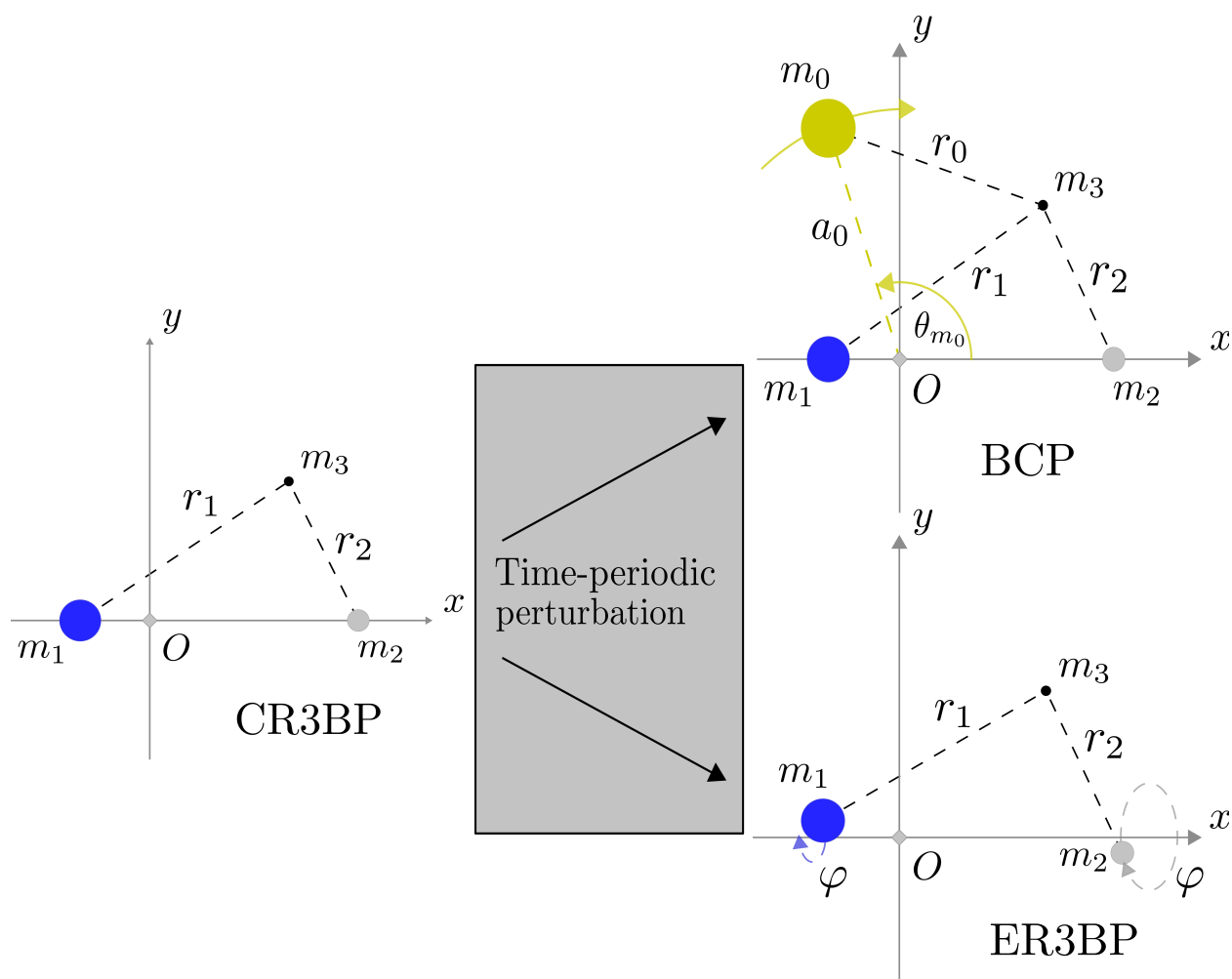


Figure 3.2: The models considered. The reference frame in each model rotates at the same constant rate as m_1 and m_2 in the CR3BP and has its origin at their center of mass.

The equations of motion for m_3 in the PCR3BP are the standard Hamiltonian equations of

motion with Hamiltonian [122],

$$H_{\text{CR3BP}} = \frac{1}{2} (p_x^2 + p_y^2) - xp_y + yp_x - \frac{1-\mu}{r_1} - \frac{\mu}{r_2}, \quad (3.9)$$

where

$$r_1 = \sqrt{(x + \mu_2)^2 + y^2}, \quad r_2 = \sqrt{(x - \mu_1)^2 + y^2}, \quad (3.10)$$

$\mu_1 = 1 - \mu$ and $\mu_2 = \mu$ are the non-dimensionalized masses of μ_1 and μ_2 , and $\mu = m_2/(m_1 + m_2)$ is the mass parameter.

The bicircular problem

The first generalization of the CR3BP to be considered is the bicircular problem (BCP). The BCP adds an additional mass, m_0 , to the system (see Figure 3.2). m_0 and O circle their mutual center of mass, but the equations are written in the CR3BP reference frame so that m_1 and m_2 still appear fixed and m_0 seems to circle O [38, 39].

Unlike the equations of motion of the CR3BP, those for m_3 in the BCP are dependent on a time-periodic perturbation and can be written in the form (3.1). The BCP equations of motion are the standard Hamiltonian equations of motion with Hamiltonian

$$H_{\text{BCP}} = H_{\text{CR3BP}} + H_{m_0}(t), \quad (3.11)$$

with time-dependent perturbation

$$H_{m_0}(t) = \frac{\mu_0}{a_0^2} \left(x \cos \theta_{m_0}(t) + y \sin \theta_{m_0}(t) \right) - \frac{\mu_0}{r_0(t)} \quad (3.12)$$

and in which

$$\begin{aligned} r_0(t)^2 &= (x - a_0 \cos \theta_{m_0}(t))^2 + (y - a_0 \sin \theta_{m_0}(t))^2, \\ \theta_{m_0}(t) &= -\omega_{m_0} t + \theta_{m_0 0}. \end{aligned} \tag{3.13}$$

a_0 , μ_0 , θ_{m_0} , $\theta_{m_0 0}$, ω_{m_0} , and r_0 are the distance from O , mass, current angle, initial angle of m_0 , angular velocity, and distance from m_3 , respectively, in non-dimensional units.

The BCP's time perturbation has period $T = 2\pi/\omega_{m_0}$. We observe that the BCP converges to the CR3BP when $\mu_0 \rightarrow 0$, when $a_0 \rightarrow \infty$, or when $\omega_{m_0} \rightarrow \infty$: when m_0 's mass gets arbitrarily close to 0, when m_0 gets arbitrarily far away, or when m_0 's angular velocity becomes so large that the perturbation averages out, respectively.

The elliptic restricted three-body problem

The second generalization of the CR3BP to be considered is the elliptic restricted three-body problem (ER3BP). Instead of adding in a fourth body, as in the BCP, the ER3BP drops the restriction that m_1 and m_2 orbit O in circles, and instead permits them to orbit O in more realistic ellipses. Unlike most researchers [40, 123, 56, 124], but following our prior usage for the analysis of the linear case [120], we use the standard CR3BP rotating frame instead of a pulsating coordinate system. m_1 and m_2 are no longer fixed but periodically orbit their locations in the CR3BP (see Figure 3.2).

The ER3BP equations of motion are also dependent on a time periodic perturbation and can be written as (3.1). They are the standard Hamiltonian equations of motion with Hamiltonian

$$H_{\text{ER3BP}} = \frac{1}{2}(p_x^2 + p_y^2) - xp_y + yp_x - \frac{\mu_1}{r_1(t)} - \frac{\mu_2}{r_2(t)}, \tag{3.14}$$

where

$$r_i^2(t) = \left| \left(\begin{bmatrix} x \\ y \end{bmatrix} + \frac{1 - \mu_i}{1 + e \cos \varphi(t)} \mathbf{R}(t) \begin{bmatrix} \cos \varphi(t) \\ \sin \varphi(t) \end{bmatrix} \right) \right|^2, \quad (3.15)$$

with $\mathbf{R}(t) = \begin{bmatrix} \cos t & \sin t \\ -\sin t & \cos t \end{bmatrix}$,

and in which $\varphi(t)$ solves the differential equation

$$\dot{\varphi} = \frac{(1 + e \cos \varphi)^2}{(1 - e^2)^{3/2}} \quad (3.16)$$

with initial condition $\varphi(0) = \varphi_0$.

The ER3BP's time perturbation has period $T = 2\pi$ and the system converges to the CR3BP when the eccentricity $e \rightarrow 0$.

3.3.2 The Lagrange periodic orbits

The phase space transit structure of the CR3BP, once subjected to a single time-periodic perturbation, is determined by the local transport geometry near *Lagrange periodic orbits* or more generally *Lagrange manifolds*, which are also termed *the dynamical equivalents of the equilibria* in the literature [120, 52]. Lagrange periodic orbits generalize the Lagrange points, the equilibria of the CR3BP, which similarly dictate the transport geometry of the unperturbed case [122]. For more details on calculating Lagrange periodic orbits and understanding how they bifurcate out of unperturbed equilibria, refer to Jorba, Jorba-Cuscó, and Rosales [52] and Fitzgerald and Ross [120].

In this study, we consider the transit geometries arising from the Lagrange periodic orbits replacing the L_1 Lagrange point in the Sun-perturbed Earth-Moon BCP and the Earth-Moon

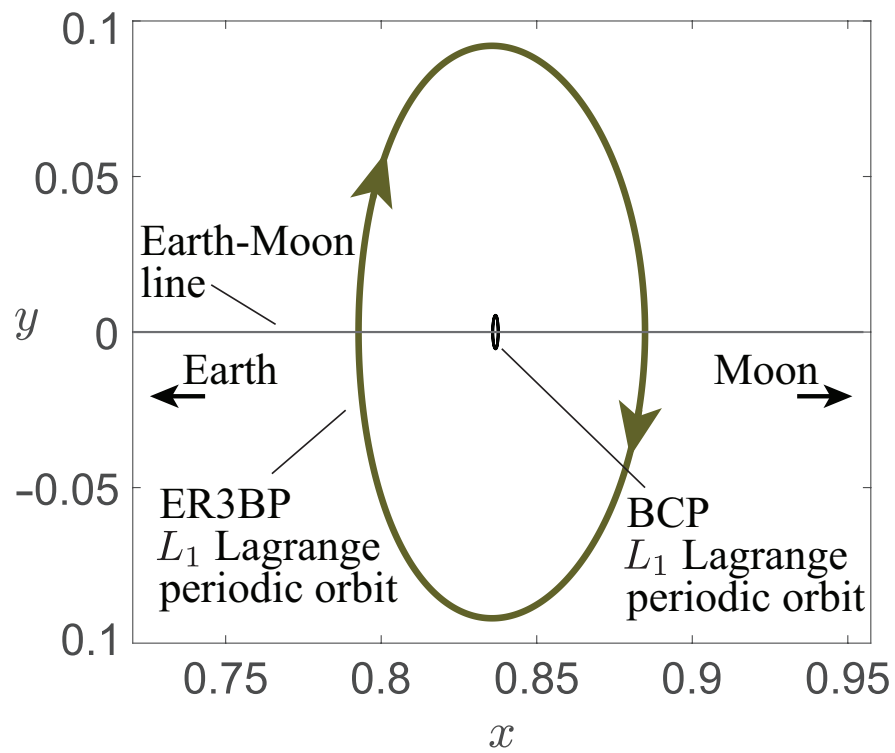


Figure 3.3: The ER3BP Earth-Moon L_1 periodic orbit (large, dark green) and the BCP Earth-Moon-Sun L_1 periodic orbit (black) projected into position space (CR3BP rotating coordinate frame). The BCP L_1 periodic orbit has a doubly looping structure (not shown) whereas the ER3BP L_1 periodic orbit has a singly looping structure.

ER3BP (see Figure 3.3).

3.3.3 Geometry of the linear map

As mentioned in Subsection 3.2.3, Fitzgerald and Ross [120] approximated the stroboscopic maps of the BCP and ER3BP at the L_1 periodic orbits using (3.5), setting $m = 1$, which enables the analysis of the linear geometry.

The first step enabling this analysis is to numerically integrate the monodromy matrix $\Phi^{(1)}$ over the L_1 periodic orbit. We then verify that $\Phi^{(1)}$ is symplectic; that is, it permits

$$\left(\Phi^{(1)}\right)^T \mathbf{J} \Phi^{(1)} = \mathbf{J} \quad (3.17)$$

where

$$\mathbf{J} = \begin{bmatrix} \mathbf{0} & \mathbf{1} \\ -\mathbf{1} & \mathbf{0} \end{bmatrix} \quad (3.18)$$

is the symplectic matrix, with the zero matrix $\mathbf{0}$ and the identity matrix $\mathbf{1}$.

However, the phase space is so unstable that numerical inaccuracies arise at standard machine precision, destroying the symplecticity of the matrix. We circumvented this issue by integrating the monodromy matrix at quadruple precision using the Multiprecision Computing Toolbox [125], which allowed us to demonstrate that the matrix is symplectic to within a maximum error of less than 10^{-8} in the BCP.

The second step enabling this analysis is to calculate the eigensystem of $\Phi^{(1)}$ and construct a symplectic eigenbasis using the eigenvectors. Let $\mathbf{x} = (q_1, p_1, q_2, p_2)$ be a small displacement from the reference trajectory expressed in the symplectic eigenbasis, where the first canonical plane (q_1, p_1) contains hyperbolic / saddle dynamics and the second canonical plane (q_2, p_2) contains elliptic / center dynamics. $\Phi^{(1)}$ can be written in this eigenbasis, which yields a

linear, symplectic map

$$\tilde{\phi}_1 = \mathbf{x} \mapsto \mathbf{\Lambda} \mathbf{x} \quad (3.19)$$

where $\mathbf{\Lambda}$ is a symplectic, block diagonal matrix of the form

$$\mathbf{\Lambda} = \begin{bmatrix} \sigma & 0 & 0 & 0 \\ 0 & \sigma^{-1} & 0 & 0 \\ 0 & 0 & \cos \psi & \sin \psi \\ 0 & 0 & -\sin \psi & \cos \psi \end{bmatrix} \quad (3.20)$$

for some $\psi \in S^1$ and for $\sigma > 1$.

The third step enabling this analysis is to notice that the map (3.19), although computed using the full equations of motion, could *also* arise by applying a stroboscopic map to the equations of motion generated from the effective quadratic Hamiltonian

$$\tilde{H}_2 = \tilde{\lambda} q_1 p_1 + \frac{1}{2} \tilde{\nu} (q_2^2 + p_2^2), \quad (3.21)$$

where

$$\tilde{\lambda} = \frac{1}{T} \ln \sigma > 0, \quad \tilde{\nu} = \frac{1}{T} \psi > 0. \quad (3.22)$$

For a proof of the validity of this Hamiltonian, see Fitzgerald and Ross [120].

Because (3.21) locally approximates the true Hamiltonian in the vicinity of the Lagrange periodic orbit when the stroboscopic map is taken, it can be used to develop a qualitative picture of the dynamics (see Figure 3.4). Fix sufficiently small $h = \tilde{H}_2 > 0$. A *forbidden region* arises, which also exists in the full dynamics, through which m_3 cannot move because it does not have enough energy. This forbidden region separates the *realms* of position space that the particle can visit (refer to Fitzgerald and Ross [120] for a fuller discussion of the forbidden region and the realms of motion). The only way to pass between realms is through

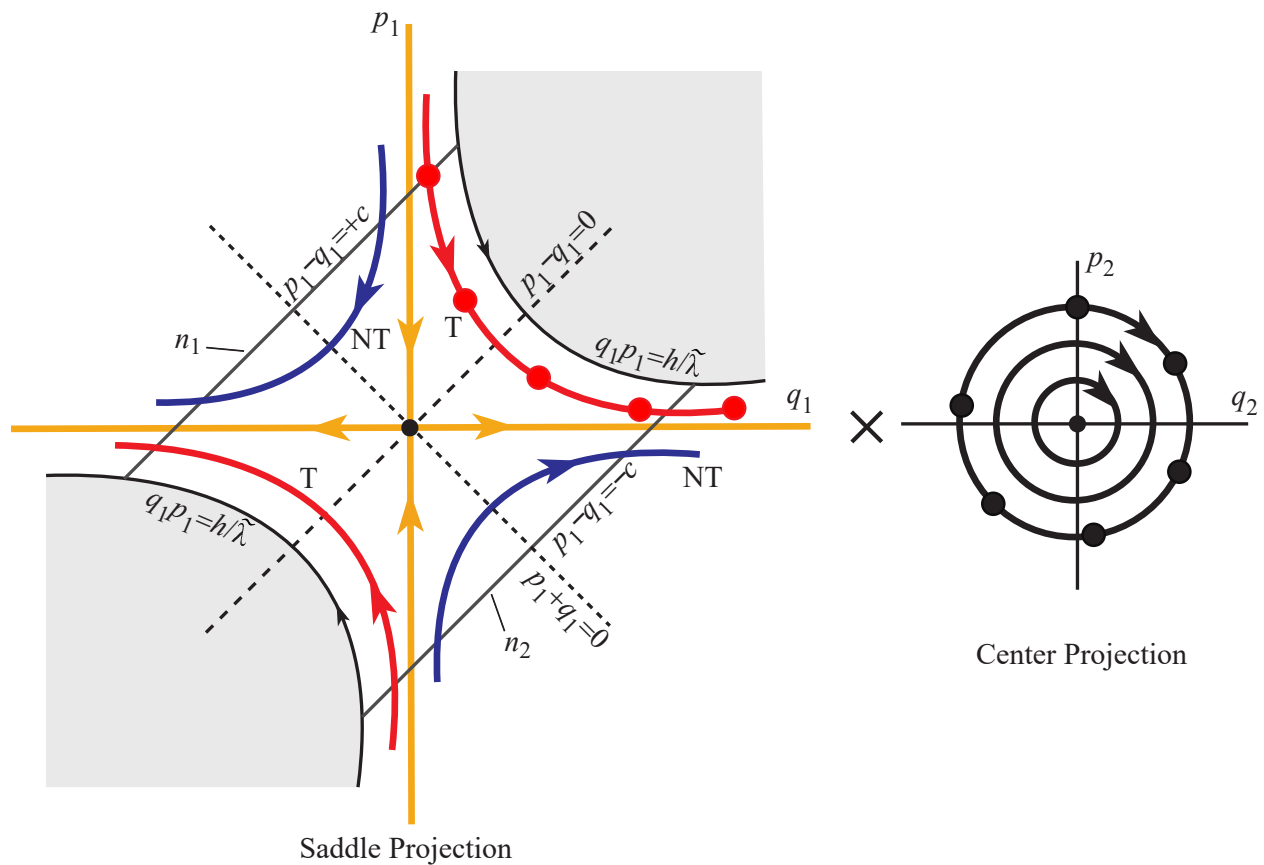


Figure 3.4: The two canonical planes of the discrete dynamics governed by $\mathbf{x} \mapsto \Lambda \mathbf{x}$; the orbits here are discrete points (the large dots) that when iterated under the map “jump” along the solution curves.

a “neck” region about the Lagrange periodic orbit.

For small c , the bounding line $p_1 - q_1 = +c$ lies wholly within one realm; the bounding line $p_1 - q_1 = -c$ lies wholly within the other. The origin of the saddle plane is the center manifold to the Lagrange periodic orbit, which corresponds to the family of quasi-Lyapunov orbits of the full system [109]. Consider the types of initial conditions that can lie along these bounding lines [120]:

1. The intersection of $p_1 - q_1 = \pm c$ with the p_1 -axis contains points that, when iterated under the map, asymptotically approach the quasi-Lyapunov orbit of energy h . These are the *stable manifolds*, and similarly points along the q_1 -axis comprise the *unstable manifolds*.
2. The points along the bounding lines that lie in the first and third quadrants are constrained to “jump” along the solution curves, which must themselves intersect both $p_1 - q_1 = +c$ and $p_1 - q_1 = -c$. Because they pass between realms, they are called *transit orbits*.
3. The points along the bounding lines that lie in the second and fourth quadrants are unable to intersect both $p_1 - q_1 = +c$ and $p_1 - q_1 = -c$. Because they do not pass between realms, they are called *nontransit orbits*.

This discrete analysis holds at any initial perturbation phase, so it holds for the full, continuous dynamics.

3.4 Quadratic transit geometry of the periodically perturbed three-body problem

3.4.1 The quadratic map

Now consider $m = 2$. To construct the quadratic map, we must simultaneously integrate the monodromy tensors $\Phi^{(1)}$ and $\Phi^{(2)}$ alongside the standard equations of motion using (3.7).

The resulting quadratic map is

$$\phi_2 = x_i \rightarrow \Phi_{i,j}x_j + \frac{1}{2}\Phi_{i,jk}x_jx_k \quad (3.23)$$

for small displacements from the reference trajectory \mathbf{x} expressed in *standard* coordinates. Because this operator is not linear over the vector space of small displacements, it is not proper to speak of its eigenvectors as in the linear case, and so we do not construct a quadratic eigenbasis.

3.4.2 Notes regarding the effective Hamiltonian

It is tempting to try to construct a cubic Hamiltonian for the quadratic map analogous to the quadratic Hamiltonian (3.21) for the linear map. However, methodological difficulties exist.

The proof establishing the validity of (3.21) in Fitzgerald and Ross [120] relied on generating the linear, continuous system of ordinary differential equations corresponding to (3.21), solving this system analytically, and then taking the stroboscopic map of the explicit solution. But, a cubic Hamiltonian generates ordinary differential equations with quadratic polynomial terms. That is, given the structure of (3.23) and by analogy with (3.21), we

would expect governing Hamiltonian equations of the form

$$\dot{x}_i = A_{i,j}x_j + B_{i,jk}x_jx_k \quad (3.24)$$

for constant tensors \mathbf{A} and \mathbf{B} . Although (3.24) resembles a Riccati equation, which tend to be solvable, the quadratic terms in Riccati equations contain second-order, not third-order, tensors as coefficients [126]. (3.24) is instead the form of a *quadratic differential system*, a class of systems which are usually analyzed using qualitative methods due to their intractability—yet even fundamental knowledge of their qualitative behavior is limited [127, 128, 129].

3.4.3 The nonlinear transit / nontransit prediction method

As a consequence, we pivot to semi-numerical descriptions of the phase space geometry. Instead of attempting to construct a cubic Hamiltonian and a change of coordinates analogous to the eigenbasis in the quadratic case, we treat the quadratic case as a perturbation of the linear case. In fact, our general strategy is to employ the linear setting wherever possible. Our methodology is as follows (see Figure 3.5):

1. Define another quadratic map

$$\tilde{\phi}_2 = Q^{-1}\phi_2Q \quad (3.25)$$

where Q is the linear eigenbasis transformation matrix. $\tilde{\phi}_2$ is the quadratic map that takes points expressed in the eigenbasis to points expressed in the eigenbasis—the quadratic analogue of $\tilde{\phi}_1$.

2. Fix a constant, small $h = \tilde{H}_2 > 0$.
3. Construct a grid of initial conditions by making small displacements from the p_1 axis

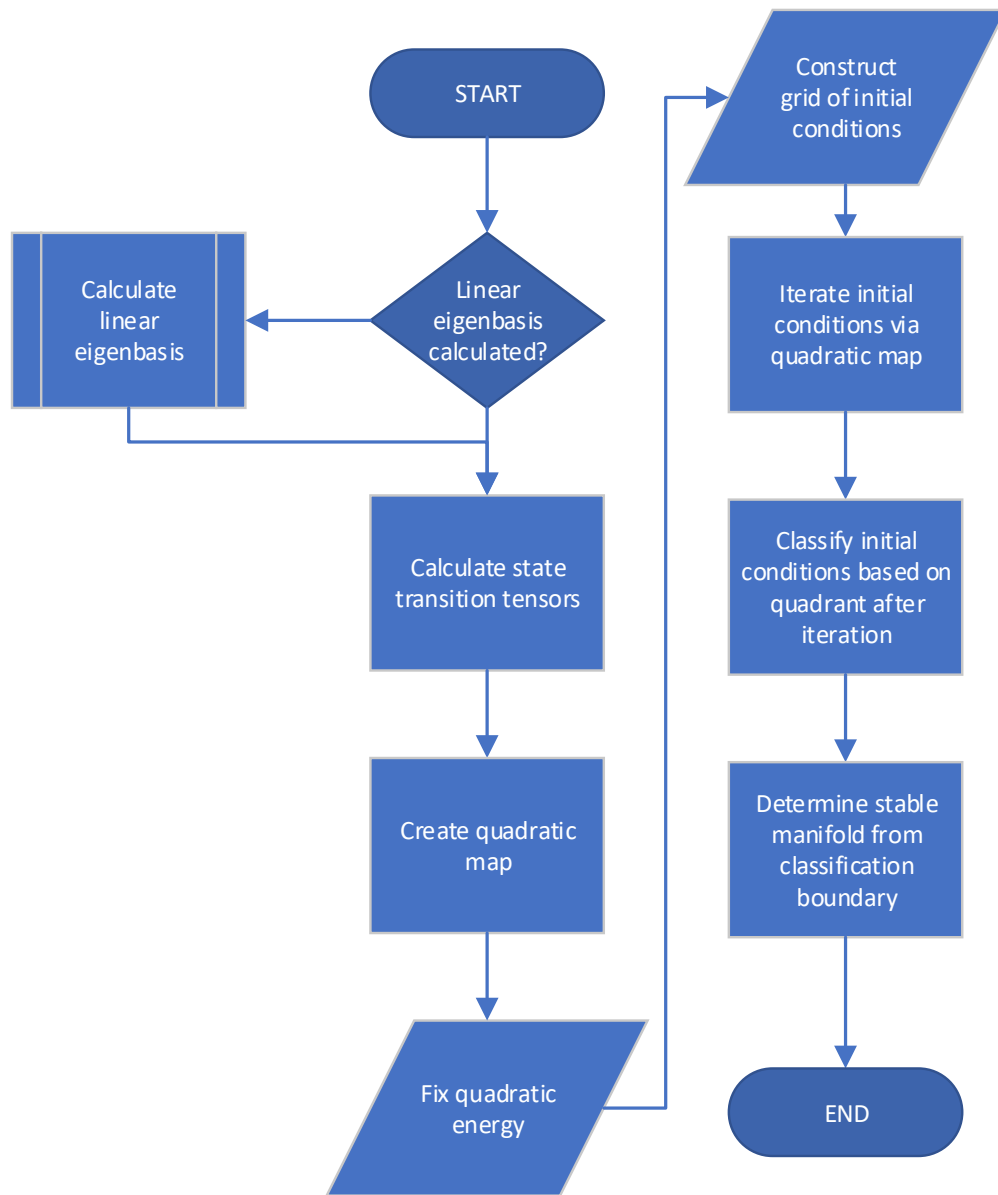


Figure 3.5: A flowchart representing the algorithm for using the quadratic map to approximate transit in the linear eigenbasis.

in the q_1 - p_1 plane. The part of the initial condition that lies in the q_2 - p_2 plane is chosen to have the form $(r \cos(\omega), r \sin(\omega))$ where r ensures that the initial condition has energy h and ω is fixed for all initial conditions under consideration.

4. Iterate forward each initial condition \mathbf{x} under ϕ_2 .
5. Determine the quadrant in which each $\phi_2(\mathbf{x})$. The linear geometry suggests that transit orbits will end up in either the first or third quadrant, depending on whether their initial conditions lie in the upper or lower half-plane, and nontransit orbits will end up in the second or fourth quadrant (recall Figure 3.4).
6. Because the stable manifold separates transit orbits from nontransit orbits, the stable manifold as predicted by the quadratic map forms the boundary between the region of transit initial conditions and the region of nontransit initial conditions.

Instead of generating a fixed grid of initial conditions, it is possible to implement the methodology above more dynamically by way of a bisection algorithm, which can locate the stable manifold to within a specified error tolerance.

The algorithm can also be adapted to locate the unstable manifold. Construct a grid of initial conditions as before, but make small displacements along the q_1 axis instead. Calculate the monodromy tensors over negative one periods, giving the inverse of the standard tensors, and then iterate the initial conditions under the inverse quadratic map ϕ_2^{-1} . Categorize the initial conditions as before; the boundary between the regions forms the unstable manifold. We expect the stable and unstable manifolds predicted via the quadratic map to trace a quadratic curve through the saddle projection of the linear eigenbasis, similarly to how the stable and unstable manifolds predicted via the linear map trace a quadratic curve (see Figure 3.6). As in the linear, periodically-perturbed case, trajectories will appear to “jump” along the manifolds when sampled via the stroboscopic map.

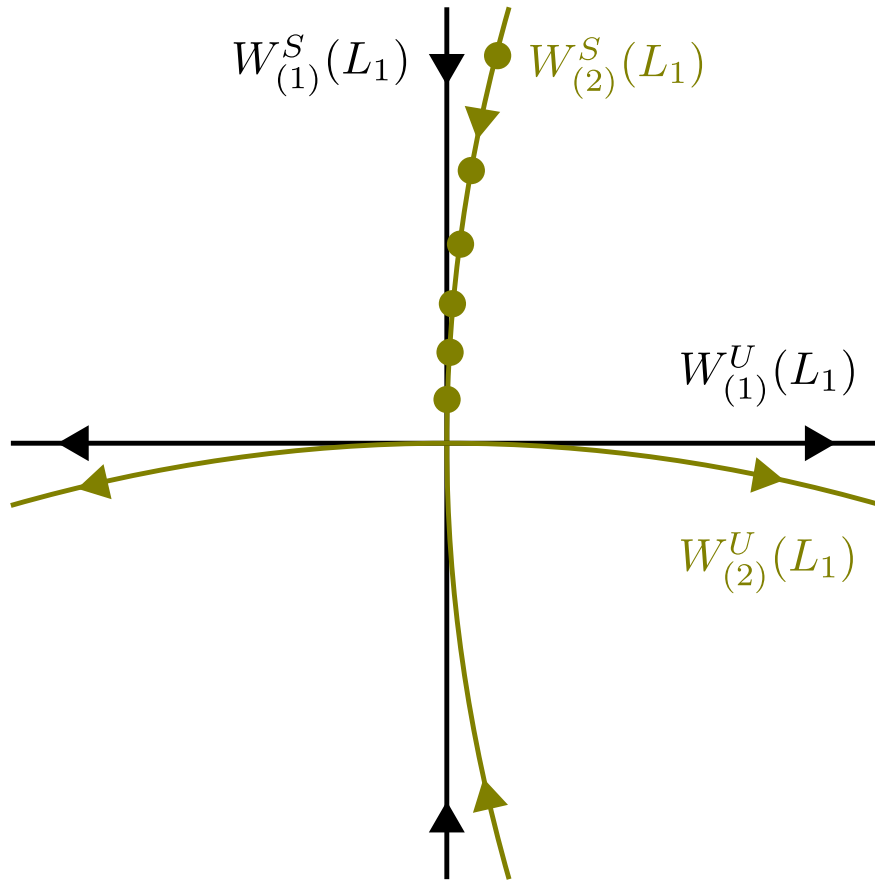


Figure 3.6: A schematic comparison of the expected geometries of the quadratic and linear stable and unstable manifolds, viewed in the linear eigenbasis. The stable and unstable manifolds predicted by the map of order i are denoted as $W_{(i)}^S(L_1)$ and $W_{(i)}^U(L_1)$, respectively. The circles on the quadratic stable manifold exemplify how, as in Figure 3.4, this picture is only valid at a fixed phase of the perturbation. Under the stroboscopic map, trajectories will return to the manifolds in a discrete, discontinuous fashion.

3.5 Transit orbits in the bicircular problem

We first apply the theoretical framework in Section 3.4 to the analysis of the Sun-perturbed Earth-Moon bicircular problem, in which m_3 represents a spacecraft moving under the gravitational fields of the Sun, the Earth, and the Moon, which correspond to m_0 , m_1 , and m_2 , respectively. In non-dimensional units, the physical parameters are $\mu = 0.01215$, $\mu_0 = 328900.54$, $\omega_{m_0} = 0.925195985520347$, and $a_0 = 388.81114$.

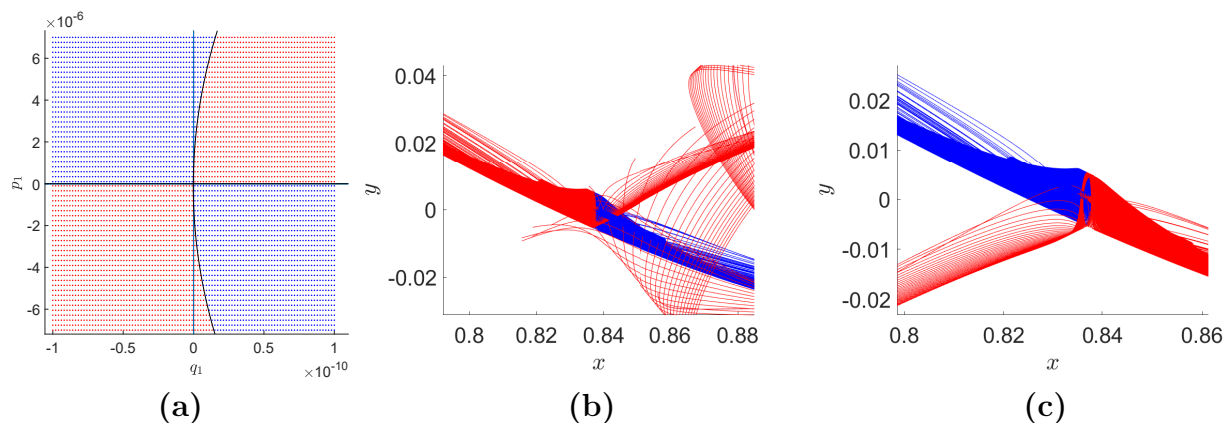


Figure 3.7: (a) The fates of orbits in the Sun-perturbed Earth-Moon BCP predicted by iterating the forward-time quadratic map over a grid of 6,000 initial conditions and classifying them depending on the linear q_1 - p_1 plane quadrant to which the iterate belongs. Blue points correspond to nontransit orbits, whereas red points correspond to transit orbits. The black lines correspond to the stable and unstable manifold, which were refined using bisection; the unstable manifold also possesses a slight curvature, but it is not visible due to the extreme inequality of the axes. $h = 10^{-13}$ and each initial condition is chosen so that $q_2 = p_2 > 0$. (b) The orbits from the $p_1 > 0$ halfplane of (a) integrated in standard coordinates and projected into position space. (c) The orbits from the $p_1 < 0$ halfplane of (a) integrated in standard coordinates and projected into position space.

Applying the results of this methodology to the Sun-perturbed Earth-Moon BCP yields the transit structure shown in Figure 3.7. The blue points/trajectories transit, whereas the red points/trajectories do not transit. We observe that the quadratic map more accurately predicts transit/nontransit behavior than the linear map, whose predicted stable manifold coincides with the p_1 axis in the eigenbasis. For even larger displacements from the Lagrange

periodic orbit, the quadratic map would prove insufficient and a cubic (or higher order) map would become necessary.

Notice that our approach for verifying the accuracy of the method contains a “built-in” sensitivity analysis. As demonstrated in Figure 3.7, our numerical experiments show that the quadratic map predicts transit for $|p_1| \lesssim 6 \times 10^{-6}$ and $|q_1| \lesssim 10^{-10}$ under these particular energy and parameter values. These bounds were chosen for visualization because the method fails, for example, when the range of p_1 is expanded much further.

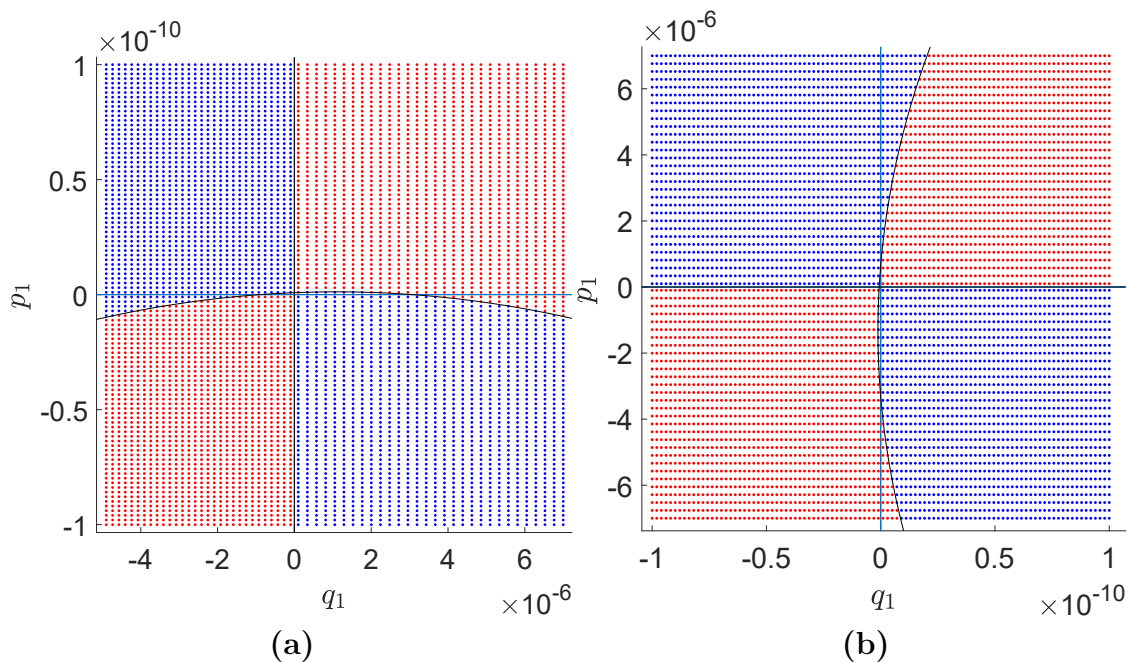


Figure 3.8: (a) The transit/nontransit behavior of initial conditions in backwards time where $p_2 = q_2$. (b) The transit/nontransit behavior of initial conditions in forward time where $p_2 = -q_2$ instead of $p_2 = q_2$.

As mentioned in Section 3.4, this analysis can also be modified to locate the unstable manifold, which yields maps of the transit behavior for particles moving backwards in time (see part (a) of Figure 3.8).

One of the most interesting results in the quadratic case is that the saddle plane of the linear eigenbasis is no longer uncoupled from the center plane. In Figure 3.7, each initial condition

is constructed so that $p_2 = q_2$. If we instead set $p_2 = -q_2$ where $q_2 > 0$, the stable manifold is still a parabola, but it follows a slightly different path in the q_1 - p_1 plane (see part (b) of Figure 3.8).

3.6 Transit orbits in the elliptic restricted three-body problem

We now apply the same theory to the analysis of the Earth-Moon elliptic restricted three-body problem. As in the BCP, m_1 is the Earth, m_2 is the Moon, and m_3 is a spacecraft. We use the eccentricity $e = 0.0549006$.

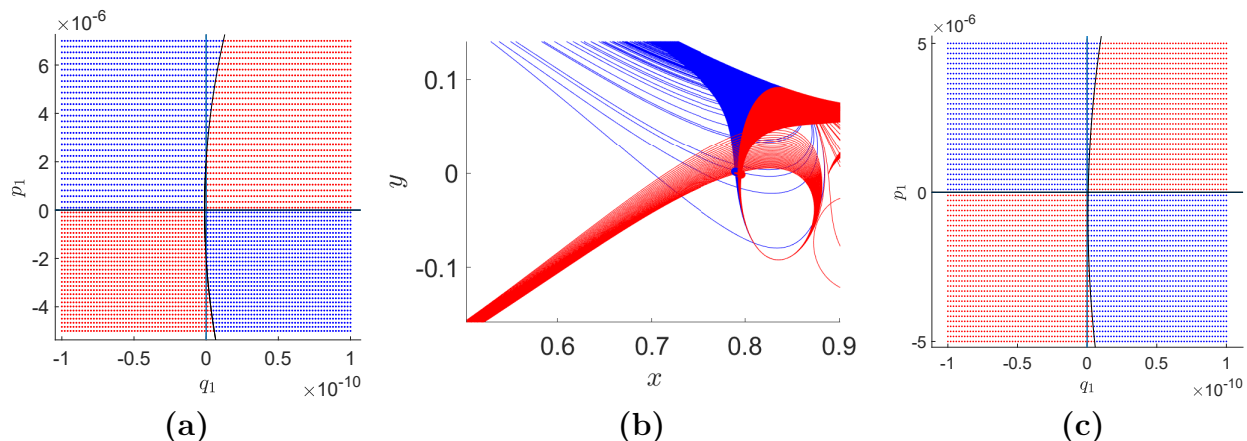


Figure 3.9: (a) The fates of orbits in the Earth-Moon ER3BP predicted by iterating the forward-time quadratic map over a grid of 6,000 initial conditions and classifying them. $h = 10^{-13}$ and each initial condition is chosen so that $q_2 = p_2 > 0$. (b) The orbits from the $p_1 < 0$ halfplane of (a) integrated in standard coordinates and projected into position space. (c) The transit/nontransit behavior of initial conditions in forward time where $p_2 = -q_2$ instead of $p_2 = q_2$.

An example of the transit structure for the Earth-Moon ER3BP is shown in parts (a) and (b) Figure 3.9. The blue points/trajectories transit, whereas the red points/trajectories do not transit. As in the bicircular problem, the quadratic map is more accurate than the linear map for the range of displacements from the Lagrange periodic orbit under consideration.

Just as in the bicircular case, we can build initial conditions with a different phase in the center projection. See part (c) of Figure 3.9.

3.7 Discussion and Conclusion

We demonstrate that the linear analysis of the transport geometry emanating from the Lagrange periodic orbits of the periodically perturbed CR3BP can be extended to nonlinear order via the use of state transition tensors. The state transition tensors correspond to the coefficients of higher order terms of the Taylor series expansion about a reference trajectory, which in this study was the L_1 Lagrange periodic orbit [121]. Instead of computing a linear approximation to the stroboscopic map and analyzing its geometry from within the linear eigenbasis, we compute an approximation of the map using the state transition tensors to desired order. We then use this approximated nonlinear map to quickly distinguish transit trajectories from nontransit trajectories, which is more computationally efficient than integrating the full equations of motion. Although this paper considered the quadratic map, which utilizes the first order and second order state transition tensors, this method is easily generalized to higher orders.

We demonstrate the validity of our method by applying it to the Sun-perturbed Earth-Moon bicircular problem and the Earth-Moon elliptic restricted three body problem. These two models, as more realistic generalizations of the Earth-Moon restricted three-body problem, have particular relevance for the burgeoning story of human expansion into the cislunar environment, which is exemplified by the ongoing NASA Artemis missions [130]. As a result, these astrodynamical models have been the focus of intense investigation very recently [131, 132, 133, 134, 135].

There are several opportunities for future study. For example, the current work focuses on a largely numerical algorithm for analyzing the behavior of the nonlinear approximation to

the stroboscopic map. However, more work on the analytical structure of the quadratic map, as well as higher order approximations, would be a useful complement to the theory herein. Although using the quadratic map instead of the linear map does not induce major differences in the fundamental topology of the neck region, the current study suggests that a coupling between the saddle and center planes of the linear eigenbasis appears at higher orders and could be isolated.

Also, the current work relies theoretically on Taylor series expansion about the Lagrange manifold in terms of state transition tensors, but future studies could instead expand about the Lagrange periodic orbit using other types of series expansions, such as Fourier series, and analyze the transit geometry using the chosen mathematical framework. Such an approach would intrinsically have different domains of validity, which could be useful for mission analysis.

Acknowledgments

J.F. was supported by a Virginia Space Grant Consortium Graduate Research Fellowship. The authors would like to thank Angel Jorba and Jose Rosales for providing an initial condition for the periodic orbit dynamical replacement to L_1 in the bicircular problem.

Chapter 4

Geometry Associated with the CR3BP Singularities

Attribution

This chapter, a collaborative work with Aaron Rosengren and Shane Ross, has not yet been published.

Author Contributions

Fitzgerald, Ross, and Rosengren conceived of the project. Fitzgerald developed the underlying mathematical model and software, derived the analytical expressions and proofs, implemented the numerical simulations, and analyzed the simulation output with supervisory assistance from Ross. Fitzgerald produced almost all figures, and the remainder were adapted by Fitzgerald from earlier work by Ross or provided by Rosengren. Fitzgerald wrote most of the manuscript with some assistance by Ross. Fitzgerald coordinated the revisions.

4.1 Introduction

The collinear Lagrange points anchor a fractal web of manifolds which transport particles throughout the Solar System [80]. The phase space structure emanating from the Lagrange

points was first analyzed within the circular restricted three-body problem, or CR3BP [17, 15, 87, 11, 90, 85, 110, 83], but recent studies have investigated more general dynamical models, such as periodically perturbed problems [52, 109, 120, 49, 118]. The resultant theory of low energy transport is well-understood and has proven invaluable for both understanding the motions of natural celestial bodies [88, 89] and planning spacecraft missions [30, 20, 136]. Applications of the theory outside of astrodynamics span a wide range of topics, from chemical reaction dynamics [114] to snap-through buckling [42, 43]. However, for reasons that will be discussed in this study, low energy transport theory does not govern particle motion within sufficiently high energy regimes, and so different dynamical sets must take precedence.

Recent numerical investigations into solar system dynamics have revealed “arches of chaos” stretching throughout the phase space [74]. These objects induce dramatic rates of divergence between nearby trajectories on either side, suggesting that a mechanism of underlying phase space structures is responsible. The arch structure exists not only when all seven planets are considered but also when the dynamics are simplified to the Sun-Jupiter-particle system, suggesting that the core phenomenon arises in the restricted three-body problem. The current work will demonstrate that the stable and unstable manifolds to the CR3BP’s singularities are responsible for the arches of chaos.

4.2 Introduction to the Arches of Chaos

4.2.1 The Fast Lyapunov Indicator

The Fast Lyapunov Indicator (FLI) is a computational method used to find chaotic regions and other phase space structures in a dynamical system [137, 138].

Consider a manifold M where the n -dimensional tangent space at each $p \in M$ is T_pM . An

autonomous dynamical system with time variable t on M induces a flow $\phi_t : M \rightarrow M$. Let $\left\{ \frac{\partial}{\partial x^1} \Big|_p, \dots, \frac{\partial}{\partial x^n} \Big|_p \right\}$ be a basis for $T_p M$. Then the FLI at time t , with initial condition x_0 at $t = 0$, is $\psi_t : M \times \mathbb{R} \rightarrow \mathbb{R}^+$ such that

$$\psi(x_0, t) = \left(\sup_{i \in \{1, \dots, n\}} \left\{ \left\| (\phi_{t,*})_{x_0} \frac{\partial}{\partial x^i} \Big|_{x_0} \right\| \right\} \right)^{-1}$$

where $(\phi_{t,*})_{x_0}$ is the pushforward induced by ϕ_t at x_0 [137].

Because the FLI distinguishes regions of greater and lesser local “stretching”, calculating it for grids of initial conditions facilitates detecting chaos-inducing structures. However, the Fast Lyapunov Indicator detects chaotic sets but does not indicate what dynamics *created* them. Additional methods are needed, and so explaining the dynamical geometry underlying the arches of chaos is the primary aim of this study.

4.2.2 The Arches of Chaos

A recent paper by Todorović et al. ([74]) describes regions of high local stretching discovered by computing the FLI for selected initial conditions in solar system models. One model incorporates the seven major planets, whereas the other is simpler and only incorporates the Sun and Jupiter. Calculating the FLI over dense grids of initial conditions in both models gradually reveals, over sufficient timescales, the arch-like regions seen in Figure 4.1. Much of this picture persists regardless of the model employed, which led the authors to conclude that interactions with Jupiter dominate the dynamics [74].

The manifold structures associated with the arches of chaos appear and operate over fast timescales by solar system standards: several decades rather than tens of thousands of years. Because of their higher 3-body energies (lower Tisserand parameter) and faster transit times, they also differ from the low-energy manifolds, which can require thousands of years to successfully transfer particles between planets [139, 140]. As shown in Figure 4.1, the stable

manifolds to the collinear Lagrange points bound the arches when depicted in a - e space.

The surface of initial conditions

The arches of chaos are computed using initial conditions lying on a surface of constant mean anomaly M , inclination i , argument of perihelion ω , and longitude of the ascending node Ω which is parameterized by the semi-major axis a and eccentricity e of the initial conditions. For the initial epoch 30 September 2012, i , ω , and Ω for all initial conditions are set to the inclination, argument of perihelion, and longitude of the ascending node of Jupiter's orbit, and M for all initial conditions is set 60° ahead of the mean anomaly of Jupiter's orbit. These values correspond to trajectories whose position space projections begin evolution near the Sun-Jupiter L_4 Lagrange point [74]; see Figure 2.3(a).

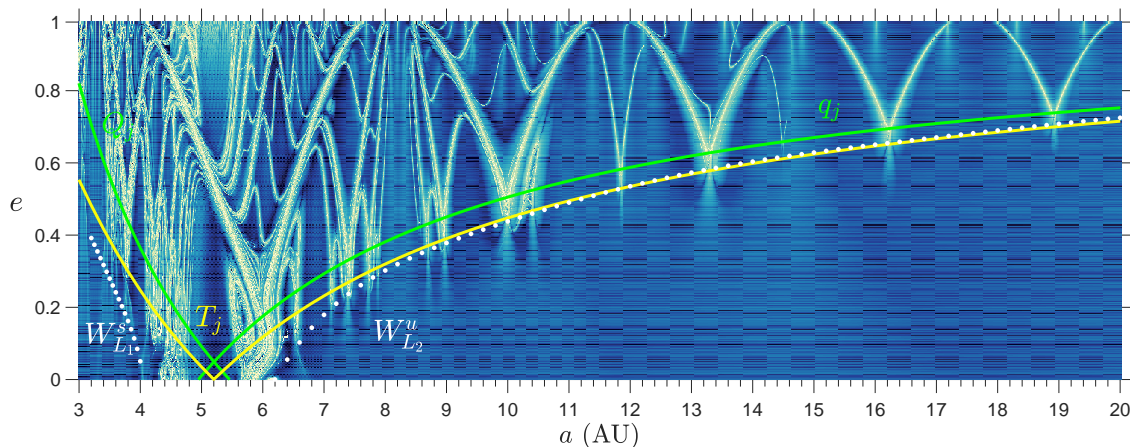


Figure 4.1: FLI maps of a grid of initial conditions with varying semi-major axes a and eccentricities e reveal a complex series of arch-like structures, the arches of chaos, in the Sun-Jupiter restricted three-body problem. Regions with lighter colors correspond to higher values of the FLI and therefore to higher trajectory divergence, which suggests the presence of stable and unstable manifolds. q_j and Q_j are Jupiter's perihelion and aphelion lines, respectively, and $T_j = 3$ is a Jupiter Tisserand curve. W_{L1}^s and W_{L2}^s are the stable manifold curves of the Sun-Jupiter L_1 and L_2 points, respectively. Figure edited from Todorović, Wu, and Rosengren [74].

4.3 The regularization of the circular restricted three-body problem

4.3.1 The CR3BP

The circular restricted three-body problem concerns the motion of a particle P of negligible mass subject to the gravitational influence of two large masses $m_1 > m_2$, which both circle their common barycenter O . For the remainder of this paper, we restrict analysis to the planar CR3BP (PCR3BP), in which P is constrained to the plane of motion of m_1 and m_2 . The generalization to the spatial case is straightforward.

We write the equations of motion within a rotating reference frame whose origin is O and whose x -axis and y -axis point along the line between m_1 and m_2 and along the direction of motion of m_2 , respectively (see Figure 4.2).

The equations of motion for P in the normalized PCR3BP are Hamilton's canonical equations

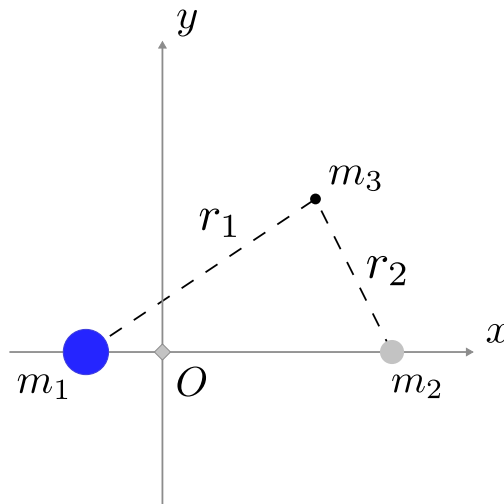


Figure 4.2: A schematic of the planar circular restricted three-body problem viewed in the rotating frame.

generated by the following Hamiltonian [122],

$$H_{\text{CR3BP}} = \frac{1}{2} (p_x^2 + p_y^2) - xp_y + yp_x - \frac{1-\mu}{r_1} - \frac{\mu}{r_2}, \quad (4.1)$$

where

$$r_1 = \sqrt{(x+\mu)^2 + y^2}, \quad r_2 = \sqrt{(x-1+\mu)^2 + y^2}$$

and $\mu = m_2/(m_1 + m_2)$ is the mass parameter.

4.3.2 The Lagrange Points and High Energies

At low Hamiltonian energies (4.1), that is, slightly above the energy of the collinear Lagrange points, phase space transport in the PCR3BP is controlled by the Lagrange points, the equilibria of the equations of motion [17, 15, 87, 122]. In the time-perturbed PCR3BP, phase space transport at low energies is controlled by generalizations of the Lagrange points sometimes called *dynamical replacements to the Lagrange points* or *Lagrange manifolds* [52, 120].

At high energies, the Lagrange points or Lagrange manifolds no longer control phase space transport. To understand why, vary the Hamiltonian energy and consider the evolution of the *forbidden realm*. Fix $H_{\text{CR3BP}} = E \in \mathbb{R}$ to be the (conserved) energy of a trajectory. P can only move throughout the *Hill's region*, the subset of position space accessible for the chosen E . The inaccessible complement is called the *forbidden realm*. The forbidden realm may exhibit one of five qualitatively distinct geometries corresponding to different intervals of the energy E (see Figure 4.3):

1. For $E < E_1$, P is confined to neighborhoods around m_1 or m_2 or to an area exterior to the forbidden realm.
2. For $E_1 < E < E_2$, P is confined to neighborhoods around m_1 or m_2 or to an area

exterior to the forbidden realm.

3. For $E_2 < E < E_3$, P gains the ability to travel between the m_1 and m_2 neighborhoods.
4. For $E_3 < E < E_4$, P gains the ability to travel between the m_2 neighborhood and the exterior area.
5. For $E_5 < E$, the forbidden realm is no longer present.

The dynamics of low-energy transport rely on the existence of the “neck regions” linking the neighborhoods. In the Case 3 energy interval often used in trajectory design, P can

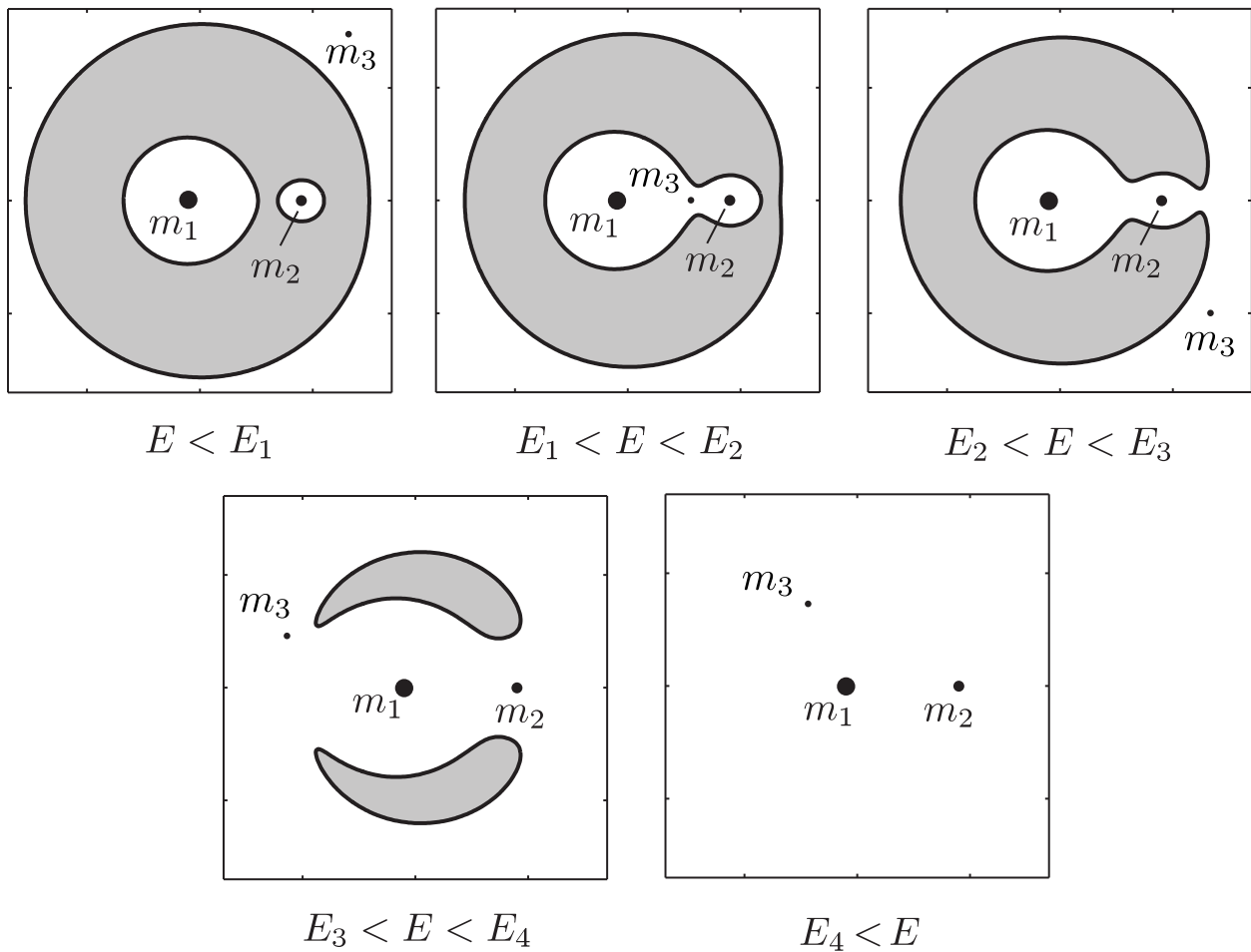


Figure 4.3: The Hamiltonian energy can be separated into five distinct intervals based on the topologies of the forbidden realm.

access all three regions of interest but is forced to travel through the necks. The neck regions correspond to the neighborhoods of the Lagrange points, which is why the linearized geometry about the Lagrange points is responsible for governing transit at low energies.

At high energies such as those within the Case 5 energy interval, the forbidden region disappears and so the neck regions no longer link regions of position space. The Lagrange points are no longer key to phase space transport.

4.3.3 Introduction to the Levi-Civita regularization

We will show in the remainder of the paper that the locations of m_1 and m_2 dictate high-energy transport, but we must first resolve a methodological difficulty.

The Hamiltonian (4.1) diverges as $r_i \rightarrow 0$ and so the associated equations of motion are not defined at $r_i = 0$. The locations of the primaries are singularities, creating challenges for numerical and analytical investigation in arbitrarily small neighborhoods of the two masses. The *Levi-Civita regularization* resolves these issues by reformulating the CR3BP in order to remove one of the singularities from the system. We assume, for the remainder of this study, that the singularity to be regularized is the singularity about m_2 .

We define a Cartesian coordinate system (X, Y) centered at m_2 where $X = x - 1 + \mu$ and $Y = y$ and a corresponding polar coordinate system (r, θ) where $r = \sqrt{X^2 + Y^2}$ and $\theta = \text{atan2}(Y, X)$.

Then, the Levi-Civita regularization recasts the phase space variables into the following form

[73],

$$\begin{aligned}
 x - 1 + \mu &= u_1^2 - u_2^2, \\
 y &= 2u_1u_2, \\
 p_x &= \frac{U_1u_1 - U_2u_2}{2|u|^2}, \\
 p_y - 1 + \mu &= \frac{U_1u_2 + U_2u_1}{2|u|^2}
 \end{aligned}
 \tag{4.2}$$

with $|u|^2 = u_1^2 + u_2^2$ (refer to a visualization of the position space transformation in Figure 4.4). In addition, the standard time t is re-scaled into the Levi-Civita time τ according to the conversion equation

$$dt = |u|^2 d\tau. \tag{4.3}$$

Regularization can recast the singularity as a *collision manifold* [141] which is included within the Levi-Civita phase space.

For topological reasons, one may extend phase space to six dimensions by including the standard time t and the standard energy E , which are conjugate to each other, so that the

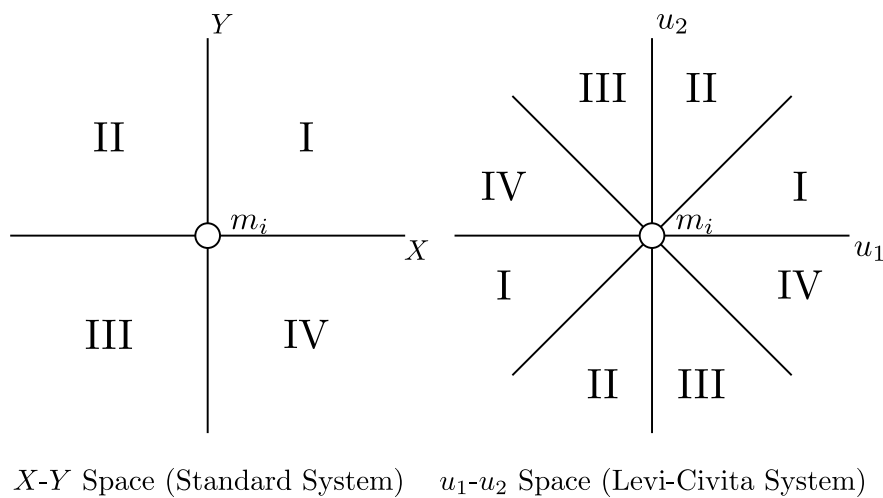


Figure 4.4: The x - y plane in standard coordinates maps to the half-plane in regularized coordinates.

full set of phase space variables becomes $(u_1, u_2, U_1, U_2, t, E)$. Note that for notational and conceptual simplicity, t and E may be omitted in certain sections of the ensuing analysis, resulting in four-dimensional state vectors. The value of E is constant in Levi-Civita time τ and must be set to the H_{CR3BP} energy of the trajectory under consideration.

The Hamiltonian for the Levi-Civita system is,

$$H_{\text{LCR}} = \frac{(U_1 + 2|u|^2 u_2)^2}{8} + \frac{(U_2 - 2|u|^2 u_1)^2}{8} - \frac{|u|^6}{2} - \mu - |u|^2 \left(E + \frac{(1 - \mu)^2}{2} \right) - (1 - \mu)|u|^2 \left(\frac{1}{\sqrt{1 + 2(u_1^2 - u_2^2) + |u|^4}} + u_1^2 - u_2^2 \right). \quad (4.4)$$

The equations of motion corresponding to (4.4) are as follows,

$$\begin{aligned} \frac{du_1}{d\tau} &= \frac{\partial H_{\text{LCR}}}{\partial U_1}, \\ \frac{du_2}{d\tau} &= \frac{\partial H_{\text{LCR}}}{\partial U_2}, \\ \frac{dt}{d\tau} &= \frac{\partial H_{\text{LCR}}}{\partial E}, \\ \frac{dU_1}{d\tau} &= -\frac{\partial H_{\text{LCR}}}{\partial u_1}, \\ \frac{dU_2}{d\tau} &= -\frac{\partial H_{\text{LCR}}}{\partial u_2}, \\ \frac{dE}{d\tau} &= -\frac{\partial H_{\text{LCR}}}{\partial t}. \end{aligned} \quad (4.5)$$

Note that the third equation in (4.5) is equivalent to (4.3) and that the sixth equation in (4.5) implies $\frac{dE}{d\tau} = 0$.

4.3.4 The Levi-Civita regularization and numerical integration

Regularization facilitates numerical investigation: attempting to integrate the standard CR3BP equations of motion in the vicinity of the singularity often causes the algorithm to fail or become prohibitively slow as the step size becomes too small.

Throughout the remainder of this paper, we numerically integrate trajectories that pass near the singularity by converting standard trajectories to Levi-Civita form using the inverse forms of (4.2) and (4.3), integrating within the regularized system, and then converting back to standard coordinates.

4.4 Preliminary Numerical Experiments on the Stable and Unstable Manifolds to the Secondary Singularity

In this section, we demonstrate the connection between the unstable and stable manifolds to the singularity of mass m_2 and the arches of chaos using several numerical experiments. All numerical experiments will occur within the context of the Sun-Jupiter PCR3BP, in which $\mu \approx 9.537 \times 10^{-4}$.

4.4.1 Global geometry of the stable and unstable manifolds

Generating initial conditions for trajectories along the stable and unstable manifolds to the m_2 singularity is very straightforward in standard coordinates. The stable manifold is comprised of trajectories that collide with the singularity in forward time, and the unstable manifold is comprised of trajectories that collide with the singularity in backward time. In what follows, we consider the phase space represented in terms of polar coordinates (r, θ) with origin at m_2 and the corresponding velocities $(\dot{r}, \dot{\theta})$. Trajectories with completely radial initial conditions $(r, \theta, -\dot{r}, 0)$ and $(r, \theta, \dot{r}, 0)$ for $0 < r < \varepsilon \ll 1$, $\dot{r} \gg 1$, and $\theta \in S^1$ therefore shadow the stable (incoming) and unstable (outgoing) manifolds, respectively. For fixed $r < \varepsilon$ and θ , an initial condition can have an \dot{r} with arbitrarily large magnitude and still lie on the manifolds, and so the stable and unstable manifolds are parameterized by the

Hamiltonian energy. The stable manifold and the unstable manifold with a chosen fixed energy are diffeomorphic to $\mathcal{C} = S^1 \times \mathbb{R}$ (a cylinder), and the full topology of each manifold is diffeomorphic to $\mathcal{C} \times \mathbb{R}$ (the Cartesian product of a cylinder and the real line, where the real line corresponds to the energy interval).

Trajectories along the globalized stable and unstable manifolds are obtained by numerically integrating these initial conditions backwards and forwards, respectively, using the procedure described in Subsection 4.3.4.

The intersections of the manifolds with a fixed energy surface are straightforward to visualize. Fix $H_{CR3BP} = E$. Select a large number of initial conditions, linearly spaced in θ , calculate the corresponding $\dot{\theta}$ at the chosen energy, and integrate. The resulting two-dimensional surface, which is embedded in the four-dimensional phase space, can be projected into three phase space dimensions for visualization; see Figures 4.5 and 4.6 where the 2-dimensional stable manifold to the singularity is shown in its (x, y, p_x) projection.

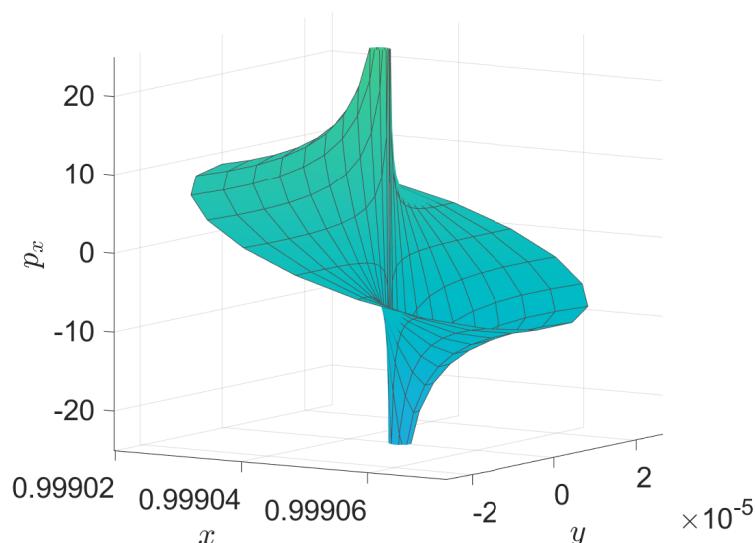


Figure 4.5: A projection of the portion of the stable manifold with $E = -1.3$ onto x - y - p_x space. Integration has been truncated while the trajectories are still close to the singularity in order to make the depiction of the geometry clearer. For a rotating view of the stable and unstable manifolds, see the video attached in the supplemental files to this dissertation.

4.4.2 Quantifying the consequences of close encounters

We demonstrate, using a numerical experiment, that trajectories *on either side* of the stable and unstable manifolds to the singularity undergo large phase space divergence. Consider the following construction, and refer to the schematic Figure 4.7:

1. Define two circles in position space centered at m_2 : a close encounter radius r_{ce} which is very small, and a detection radius r_d which is large, i.e., multiples of the Hill radius, $r_h = \left(\frac{\mu}{3}\right)^{1/3}$.
2. Generate initial conditions corresponding to trajectories which have their closest approaches to the singularity at $r = r_{ce}$. As discussed in Subsection 4.4.1, trajectories with initial conditions $(r_{ce}, \theta_{ce}, -\dot{r}, 0)$ for $\dot{r} \gg 1$ and $\theta_{ce} \in S^1$ lie on the stable manifold to the singularity. Now consider trajectories which have their *closest encounter* to the singularity at the radius r_{ce} . Such trajectories, at $r = r_{ce}$, have velocity vectors tangent

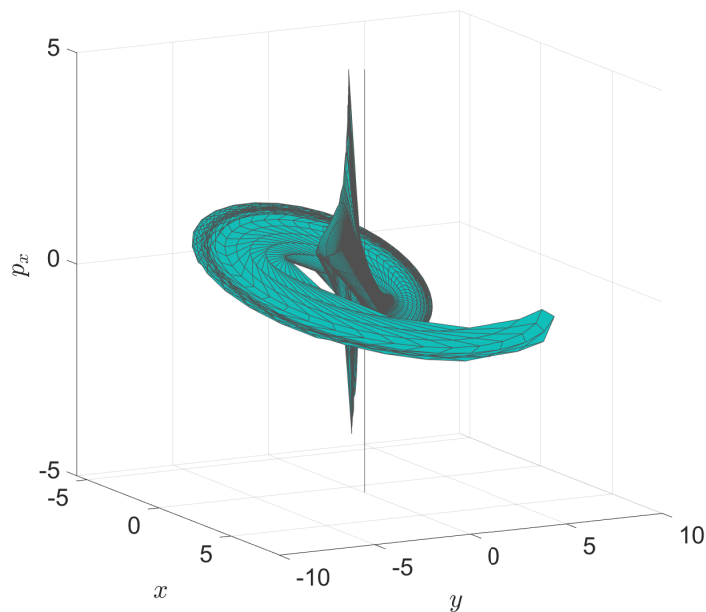


Figure 4.6: A projection of the portion of the stable manifold with $E = -1.3$ onto x - y - p_x space. Integration has been truncated much further from the singularity than in Figure 4.5.

to the circle, $r = r_{ce}$, that is $\dot{r} = 0$ and $\dot{\theta} \neq 0$. This requirement translates to the initial conditions $(r_{ce}, \theta_{ce}, 0, \dot{\theta}_{\pm})$ for $\dot{\theta}_{+} > 0$, $\dot{\theta}_{-} < 0$, and $\theta_{ce} \in S^1$. Notice that at each fixed

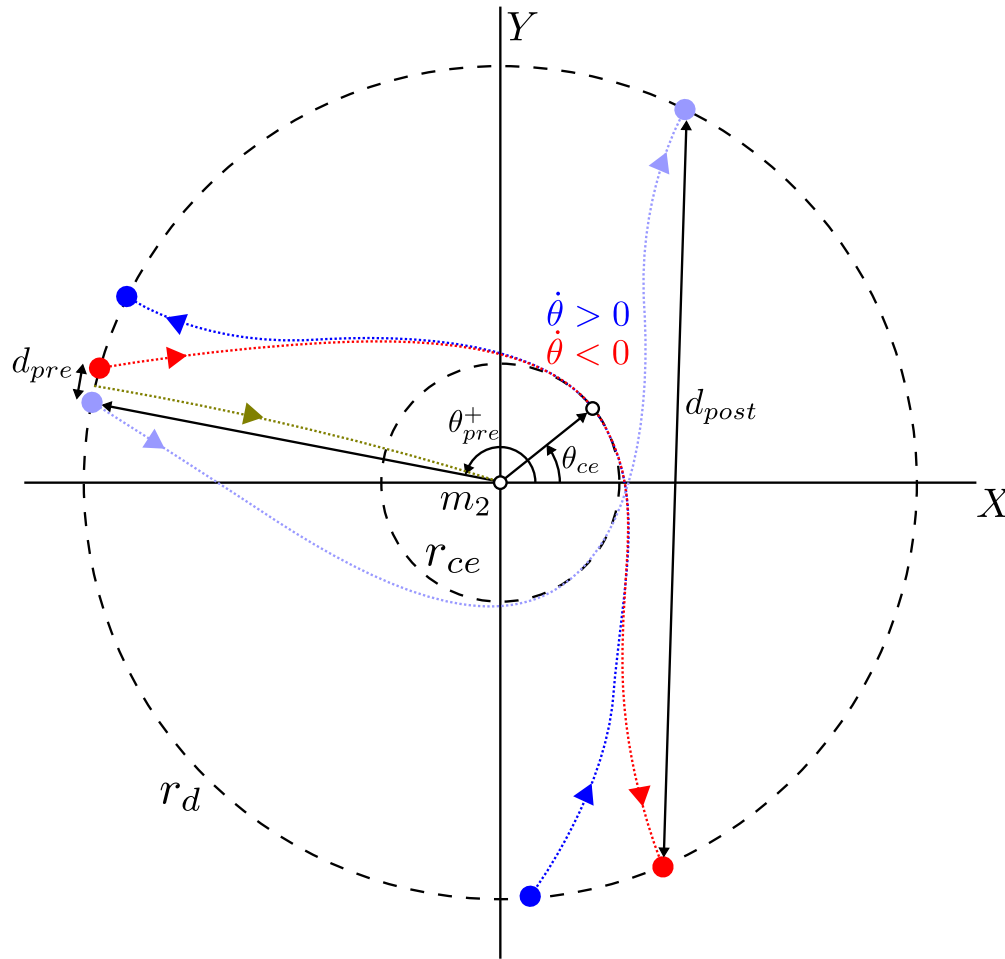


Figure 4.7: A schematic of the numerical experiment for examining how trajectories on either side of the stable manifold to the singularity move throughout phase space. The red and dark blue trajectories are generated at an initial radius r_{ce} but have $\dot{\theta} < 0$ and $\dot{\theta} > 0$, respectively. They reflect one choice of θ_{ce} , but a whole family of trajectories for different values of θ_{ce} must be generated in order to match + and - pairs along the detection radius r_d . We integrate forwards and backwards and then match those + and - trajectories whose final position in backwards time was nearest to each other; in the schematic, the red - trajectory has been matched with a light blue + trajectory, generated in the same way as the dark blue trajectory for a different value of θ_{ce} . Observe that the matched trajectories are on either side of a stable manifold trajectory, which is depicted in green. We then compare the pre-encounter, four-dimensional phase space distance d_{pre} with the post-encounter distance d_{post} for each matched pair, parameterizing by θ_{pre}^+ , the pre-encounter angle of the + trajectory (see Figure 4.8).

θ_{ce} and E there are two choices of $\dot{\theta}$, which we designate $\dot{\theta}_+$ and $\dot{\theta}_-$, satisfying the construction. Distinguish close encounter trajectories of the forms $(r_{ce}, \theta_{ce}, 0, \dot{\theta}_+)$ and $(r_{ce}, \theta_{ce}, 0, \dot{\theta}_-)$ by the terms *+ trajectories* and *- trajectories*, respectively, or prograde and retrograde, respectively.

3. Fix E and select a large number of initial conditions, linearly spaced in θ_{ce} , calculate their corresponding *+ trajectories* and *- trajectories*, and then integrate forwards and backwards using the procedure described in Subsection 4.3.4 until the trajectory intersects the detection radius, r_d .
4. Match each *- trajectory* with the *+ trajectory* whose backward-time intersection point with the r_d circle is closest to that of the *- trajectory*. This *+ trajectory* will not generally be the *+ trajectory* that was generated alongside the *- trajectory* under consideration. The *+ and - trajectories* in the matched pair will encounter the singularity from different sides and therefore lie on *either side of the stable manifold*.
5. Once each matched pair of *+ and - trajectories* has been determined, calculate the phase space distance d_{pre} between their backward-time intersection points with r_d and the phase space distance d_{post} between their forward-time intersection points with r_d , as in Figure 4.7.

Plotting d_{pre} and d_{post} as functions of the post-encounter angle of each *+ trajectory*, we discover that although the trajectories lying on either side of the stable manifold start out extremely close together, they diverge markedly post-encounter, as shown in Figure 4.8. The maximum difference in velocity between matched pre-encounter trajectories is less than 28 m/s , whereas the minimum difference in velocity between matched post-encounter trajectories is more than 3,100 m/s .

In addition, the two-body orbital elements of the matched pairs of *+ and - trajectories* with

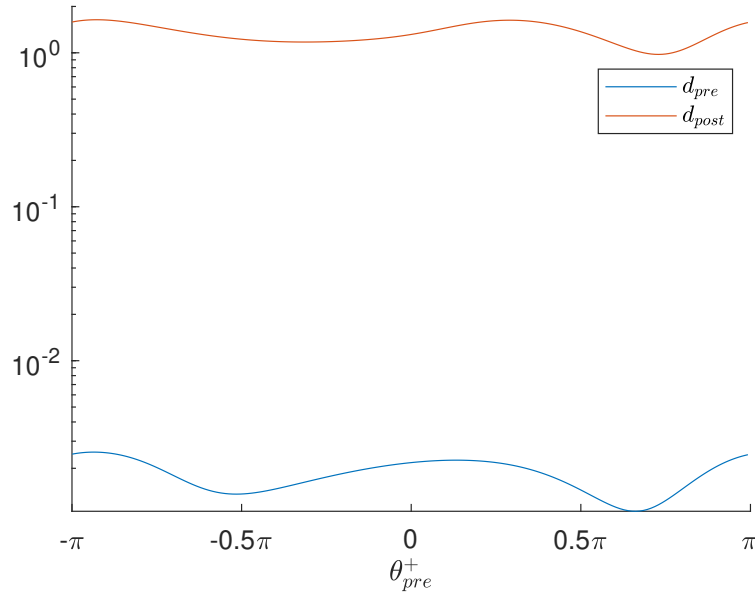


Figure 4.8: The chosen + and - trajectories have a very small initial separation pre-encounter, but post-encounter their separation significantly increases regardless of angle along the detection circle (in this case, we use θ_{pre}^+ , the pre-encounter angle of each + trajectory, as the angle for identifying and sorting matched pairs of + and - trajectories).

respect to m_1 can be calculated for the forward-time and backward-time intersections with the detection circle. We can then plot these orbital elements, such as the Keplerian energy K and the argument of perigee ω , as a function of the pre-encounter angle of each + trajectory (see Figure 4.9).

4.4.3 Close encounters and patched conics

The close encounter behavior described in the previous subsection converges to that predicted by patched conics as $r_{ce} \rightarrow 0$ and $r_d \rightarrow 0$. As a numerical experiment to verify and explore this statement, we use the Keplerian equations with respect to m_2 to find orbital elements for the initial conditions generated according to the scheme in Figure 4.7. For varying choices of r_d and r_{ce} , we build initial conditions and compute the Keplerian energies and argument of perigee values at the points where each trajectory intersects the r_d circle.

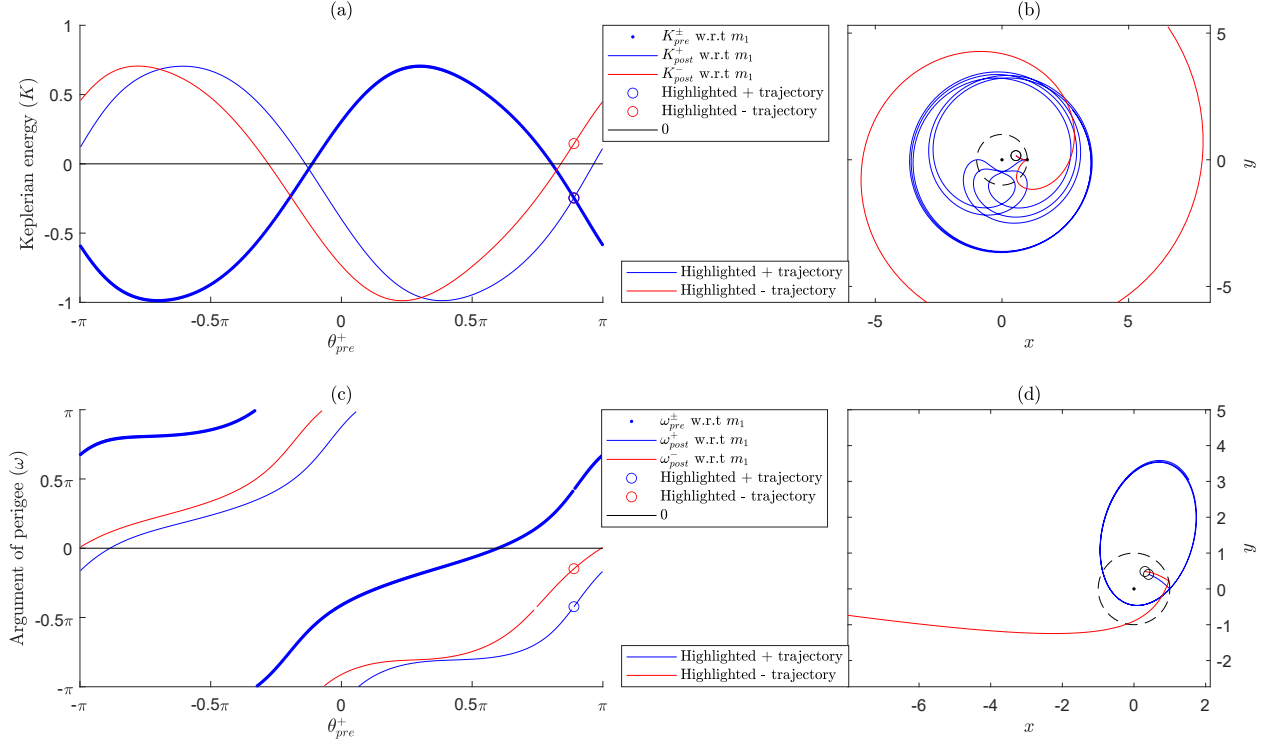


Figure 4.9: For all computations in this figure, trajectories were generated such that $r_d = 7r_h \approx 0.4774$ and $r_{ce} = 0.1R_{\mathcal{J}}$, where $R_{\mathcal{J}}$ is the radius of Jupiter in non-dimensionalized units. (a) A comparison of the Keplerian energies of the + and - trajectories as a function of the pre-encounter angle θ_{pre}^+ . K_{pre}^{\pm} denotes the pre-encounter Keplerian energies of the + and - trajectories, which approximately coincide. K_{post}^+ and K_{post}^- denote the post-encounter Keplerian energies of the + and - trajectories, respectively. The energy values of an example pair of matched + and - trajectories are highlighted. The + trajectory has negative Keplerian energy after the encounter, which predicts that it will be a bound elliptical orbit around m_1 ; the - trajectory has positive Keplerian energy after the encounter, which predicts that it will be an unbound hyperbolic orbit. (b) The highlighted pair of + and - trajectories integrated in the rotating frame, demonstrating the predicted divergence in their post-encounter fates. (c) A comparison of the argument of periapee values of the + and - trajectories as a function of the pre-encounter angle θ_{pre}^+ . ω_{pre}^{\pm} denotes the pre-encounter argument of perigee values of the + and - trajectories, which approximately coincide. ω_{post}^+ and ω_{post}^- denote the post-encounter argument of perigee values of the + and - trajectories, respectively. The values of the example trajectories are highlighted. (d) The highlighted pair of + and - trajectories integrated in the inertial frame.

Suppose r_{ce} and r_d are sufficiently small. We take $r_{ce} = \frac{R_{\mathcal{J}}}{180}$ and $r_d = r_h$, where r_h is the Hill radius. For these parameters, the orbital elements propagated via patched conics and the orbital elements calculated in the full three-body regime closely agree (see Figure 4.10). Increase r_{ce} and fix r_d so that $r_{ce} = \frac{R_{\mathcal{J}}}{10}$ and $r_d = r_h$. Then we notice, by comparison with

Figure 4.10, that the + and - trajectory values converge to the patched conics values as $r_{ce} \rightarrow 0$ (see Figure 4.11). The Keplerian energies and arguments of perigee of + and - trajectories generated along the detection circle at the same θ and then propagated with patched conics are in fact identical.

What if we instead increase r_d and fix r_{ce} so that $r_{ce} = \frac{R\gamma_L}{180}$ and $r_d = 7r_h$? Then we notice, by comparison with Figure 4.10, that the patched conics curve matches phase and shape with the + and - trajectory values as $r_d \rightarrow 0$ (see Figure 4.12).

Computing the maximum distance between the relevant curves permits quantifying the error

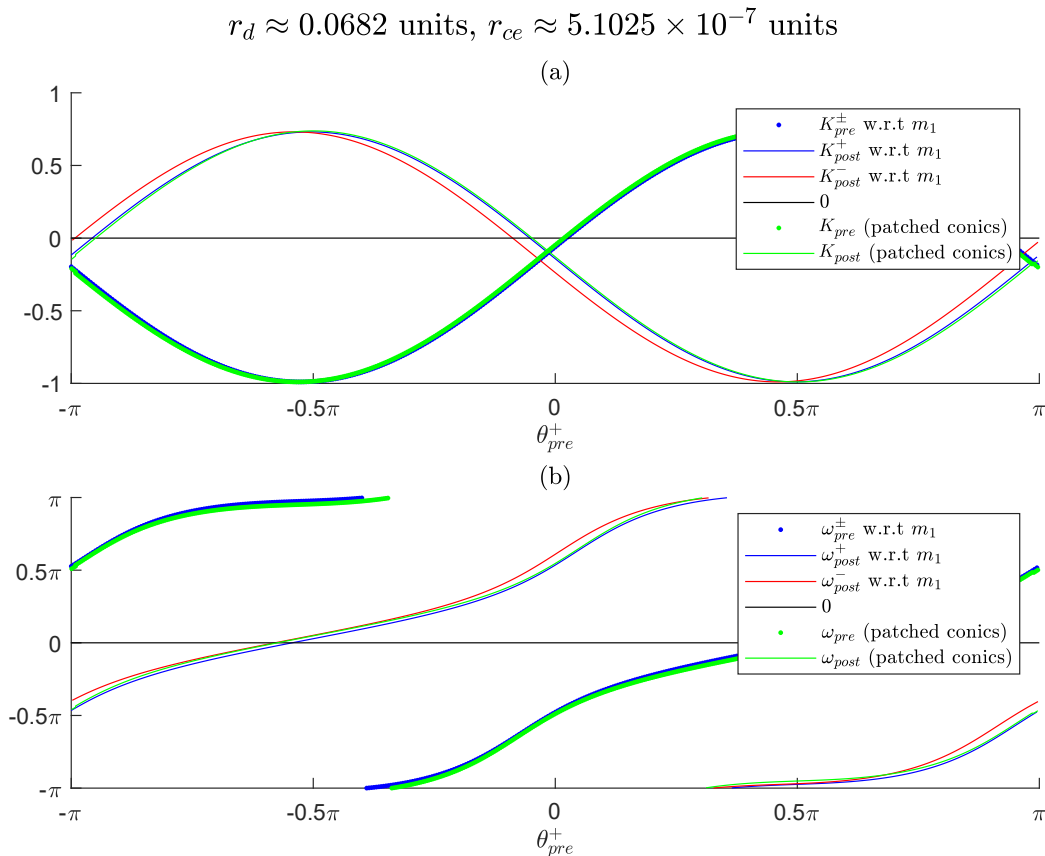


Figure 4.10: A comparison of selected orbital elements of the families of + and - trajectories integrated in the full PCR3BP equations with orbital elements ascertained through patched conics propagation. Both r_d and r_{ce} are small enough that close agreement is seen with the Keplerian case.

between the patched conics and CR3BP cases. By holding one radius constant and continuously varying the other, visualizing how the error converges to zero as the radii decrease is straightforward. Vary r_d and set $r_{ce} = \frac{R_4}{180}$. We let $r_d = nr_h$, $n > 0$. Calculating the errors in the Keplerian energy and argument of perigee over a range of n results in the behavior seen in Figure 4.13, in which the error decreases with n .

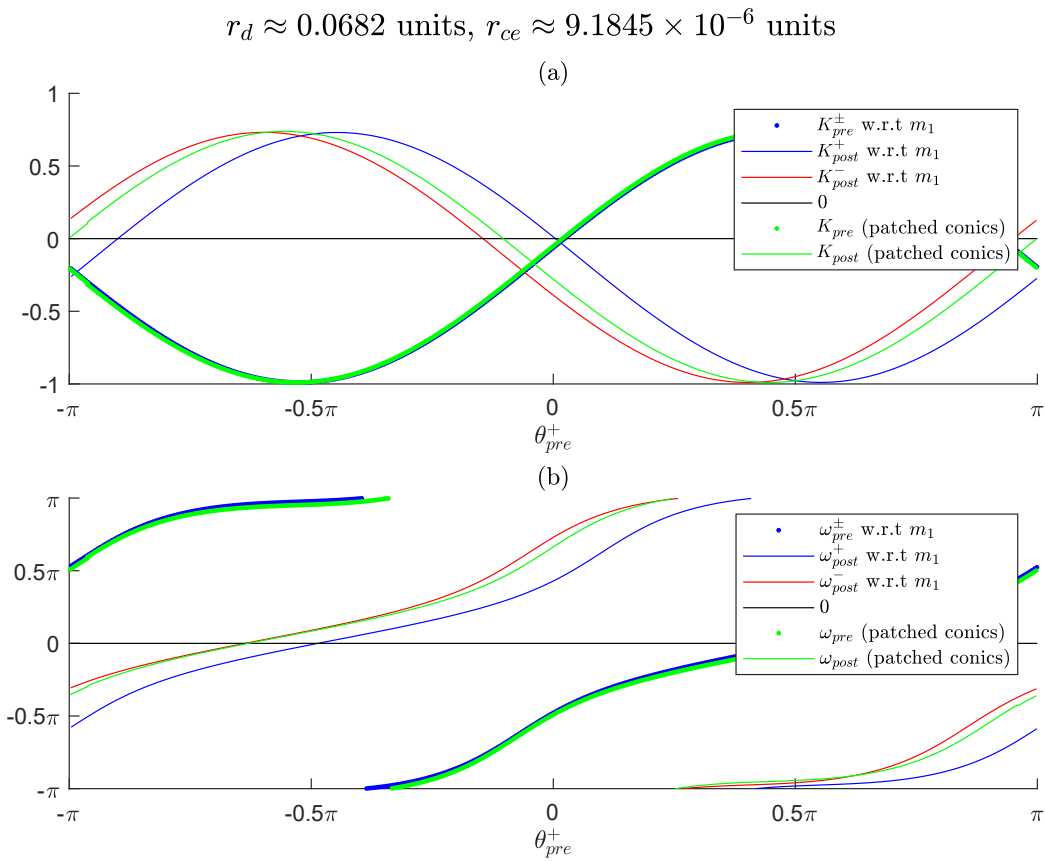


Figure 4.11: Similar to Figure 4.10, but r_{ce} has been increased.

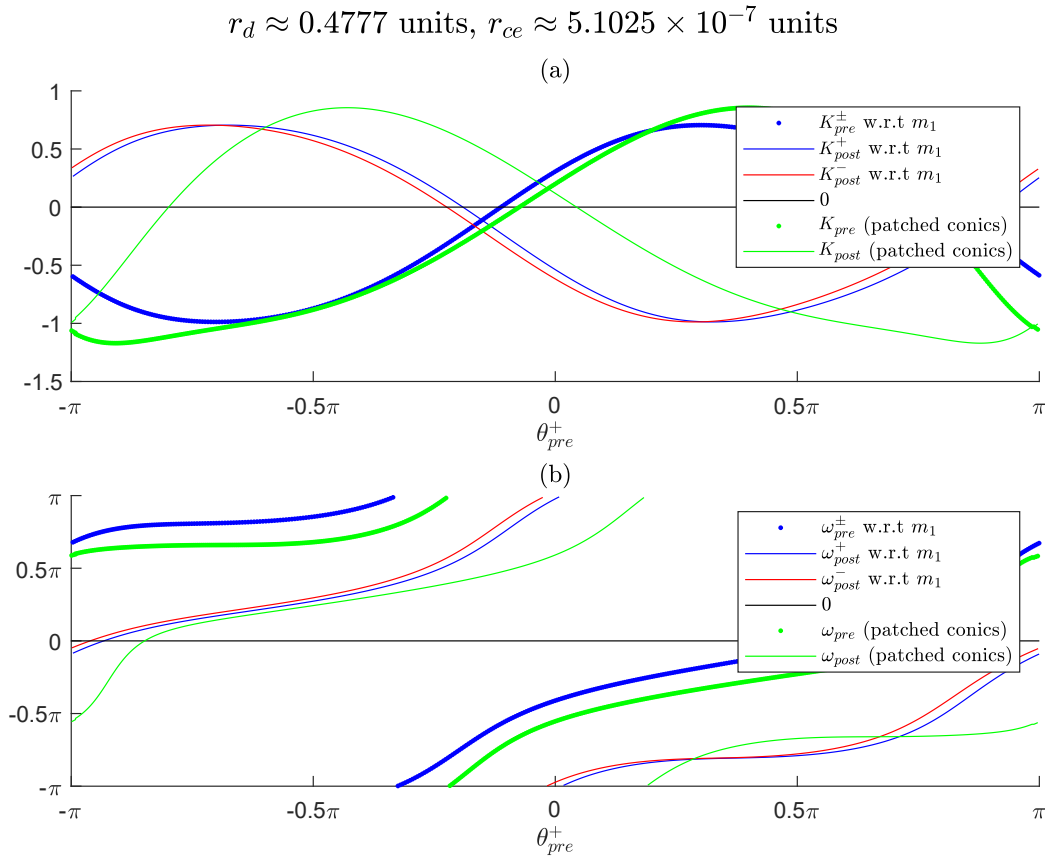


Figure 4.12: Similar to Figure 4.10, but r_d has been increased.

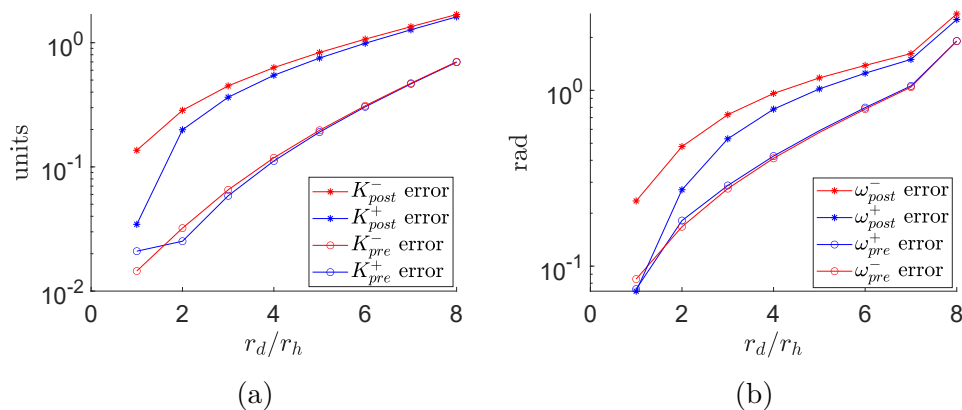


Figure 4.13: A comparison of the maximum errors between the three-body and patched conics orbital element curves. $n = r_d/r_h$. The error is computed with respect to the corresponding patched conics curve: for example, K_{pre} for K_{pre}^\pm and K_{post} for K_{post}^\pm . (a) The Keplerian energy errors. (b) The argument of perigee errors.

4.5 Numerically Linking the Arches of Chaos and the Stable and Unstable Manifolds

It is straightforward to demonstrate the geometric linkage between trajectories lying along the arches of chaos and the stable and unstable manifolds to the singularities. By globalizing the stable manifold to the m_2 singularity backwards until it reaches the section used to create the arches of chaos (see Subsection 4.2.2 for a specification of this section), we can determine whether the intersection of the stable manifold with this surface replicates the arch pattern in Figure 4.1. Previous work suggested that the connection holds in the other direction: all trajectories that have initial conditions on the section and that belong to the arch structure have close encounters with Jupiter [74].

In order to generate initial conditions along the stable manifold, we use the approach described in Subsection 4.4.1 for a cylindrical grid of θ and E values. We then integrate backwards until we reach the surface of section or until the trajectory meets one of several failure criteria, namely escaping from the vicinities of m_1 and m_2 , colliding with m_1 , or running out of integration time.

Only a very small percentage of the trajectories forming the stable manifold reach the surface of section, but those that do reach the section form a pattern that coincides with the arches of chaos, as shown in Figure 4.14. Thus, the connection between the arches of chaos and the stable manifold to the m_2 singularity is apparent.

4.6 Discussion and Conclusion

We demonstrate, using the Levi-Civita regularization as a numerical tool, that the arches of chaos can be identified with the stable and unstable manifolds emanating from the singularities in the circular restricted three-body problem. Trajectories whose initial conditions lie

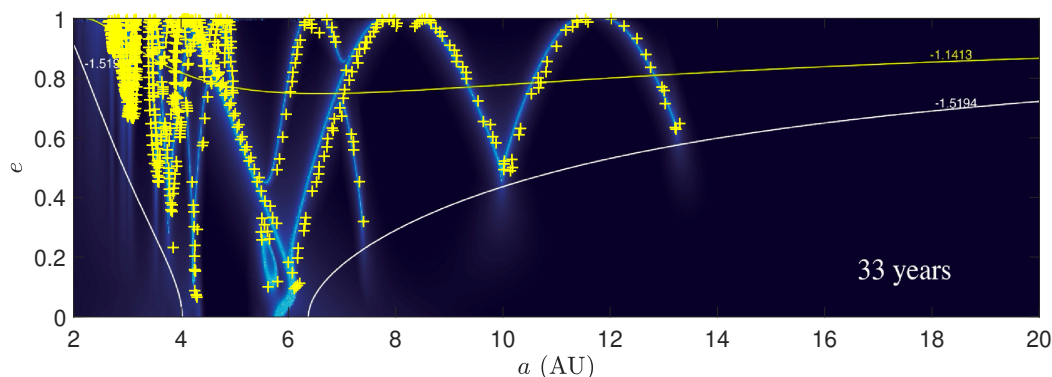


Figure 4.14: The intersection of an approximation of the stable manifold originally consisting of 40,000 trajectories with the arches of chaos section, viewed in semi-major axis/eccentricity space. Yellow crosses represent stable manifold trajectories, which have been superimposed onto a plot of the arches of chaos in the Sun-Jupiter-Spacecraft restricted three-body problem adapted from Todorović, Wu, and Rosengren [74]. The stable manifold closely shadows the arches even though only a small percentage of the trajectories intercept the section.

near either side of the manifolds experience dramatic amounts of phase space stretching, and this implication is consistent with the construction of the original FLI plots. Plotting the orbital elements of these trajectories before and after close encounters demonstrates how the manifolds affect capture/escape behavior and how the manifolds connect to patched conics flyby theory. The numerical linkage between the arches of chaos and the stable and unstable manifolds to the singularity is uncovered by globalizing the manifolds to the proper section. As an explanation of the nature of the arches of chaos, we believe that our work represents a significant contribution to the literature. In addition, it unifies several related concepts: the arches of chaos, the stable and unstable manifolds to the singularities, and patched conics flyby theory.

One interesting implication of our work is that the shape of the arches of chaos is not intrinsic to their function; rather, it arises from the specific choice of section with which the manifolds are intersected. The manifolds are three-dimensional objects embedded in a four-dimensional space. The choice of section used by Todorović et al. happens to depict these three-dimensional objects as a series of one-dimensional “arches” embedded in a two-

dimensional orbital elements space, but the manifolds could be depicted in other ways with equal validity.

Another interesting implication of our work is that Figure 4.9 implies a method for designing pairs of high-energy three-body orbits whose initial conditions lie very close to each other but whose fates are very dissimilar: one will be captured by the primary and the other will escape the system. Using a Keplerian energy plot similar to the one in the figure, a θ_{pre}^+ can be selected such that one trajectory has positive Keplerian energy with respect to the primary after encounter and the other trajectory has negative Keplerian energy with respect to the primary after encounter. This technique might facilitate the design of multi-payload missions in which the primary payload is destined for interplanetary space and the secondary payload must remain within the Earth-Moon system.

There are several potential topics for further research. Homoclinic and heteroclinic trajectories that connect Lyapunov orbits around the Lagrange points are key to understanding the global transit structure predicted by the low-energy manifold dynamics theory [122]. Analyzing heteroclinic and homoclinic connections between the singularities and other dynamical objects of interest as in Paez and Guzzo [73], particularly when perturbations capable of altering the CR3BP energy are added to the system, could facilitate the construction of an all-energy global transit structure theory. Additionally, although our work explored the arches of chaos from a purely three-body perspective, they were also introduced within a solar system model containing all major planets [74], and recent work has confirmed using Keplerian maps that transfers between different solar system planets are possible within the low-energy regime [140]. The possibility of constructing a theory that unifies low-energy interplanetary transfers and the full, high-energy arches of chaos should be explored further. It should be possible to analytically approximate the three-body Keplerian energy and argument of perigee curves found in Figures 4.9-4.12 via small displacements from the patched conics case. This idea suggests that perhaps each point on each three-body close-encounter

trajectory could be represented as a linear combination of the basis vectors of the tangent and cotangent spaces of the corresponding point on the corresponding patched conics trajectory. The resulting curvilinear coordinate system would be similar to using a state transition matrix to describe the state of a displacement trajectory in terms of a reference trajectory in the CR3BP, but it differs in the use of one model to describe another. We leave this construction for future work.

Acknowledgments

J.F. was supported by a Virginia Space Grant Consortium Graduate Research Fellowship. J.F. would like to thank Bhanu Kumar and Di Wu for helpful feedback during conceptual discussions.

Chapter 5

Assorted Results

5.1 Attribution

The current chapter describes miscellaneous minor results and so is not in manuscript form. CMDS was entirely designed and coded by Fitzgerald with minimal input from Ross in order to support the research results described elsewhere in this dissertation. The methodology for solving quadratic Lagrange manifolds was jointly developed by Ross and Fitzgerald but was entirely investigated and implemented by Fitzgerald. This chapter was written by Fitzgerald and submitted to Ross for revision.

5.2 CMDS

5.2.1 Introduction

The Context Manager for Dynamical Systems (CMDS) is a comprehensive MATLAB framework for facilitating the analysis of Hamiltonian systems. Written to support the research described in the current dissertation, CMDS automates a variety of numerical and analytical tasks, such as converting vectors between coordinate systems, generating integrable function handles representing equations of motion from symbolic kinetic and potential energy, and integrating state transition tensors up to quadratic order. For links to CMDS and the other codebases underlying the current work, refer to [Appendix A](#).

5.2.2 Architecture

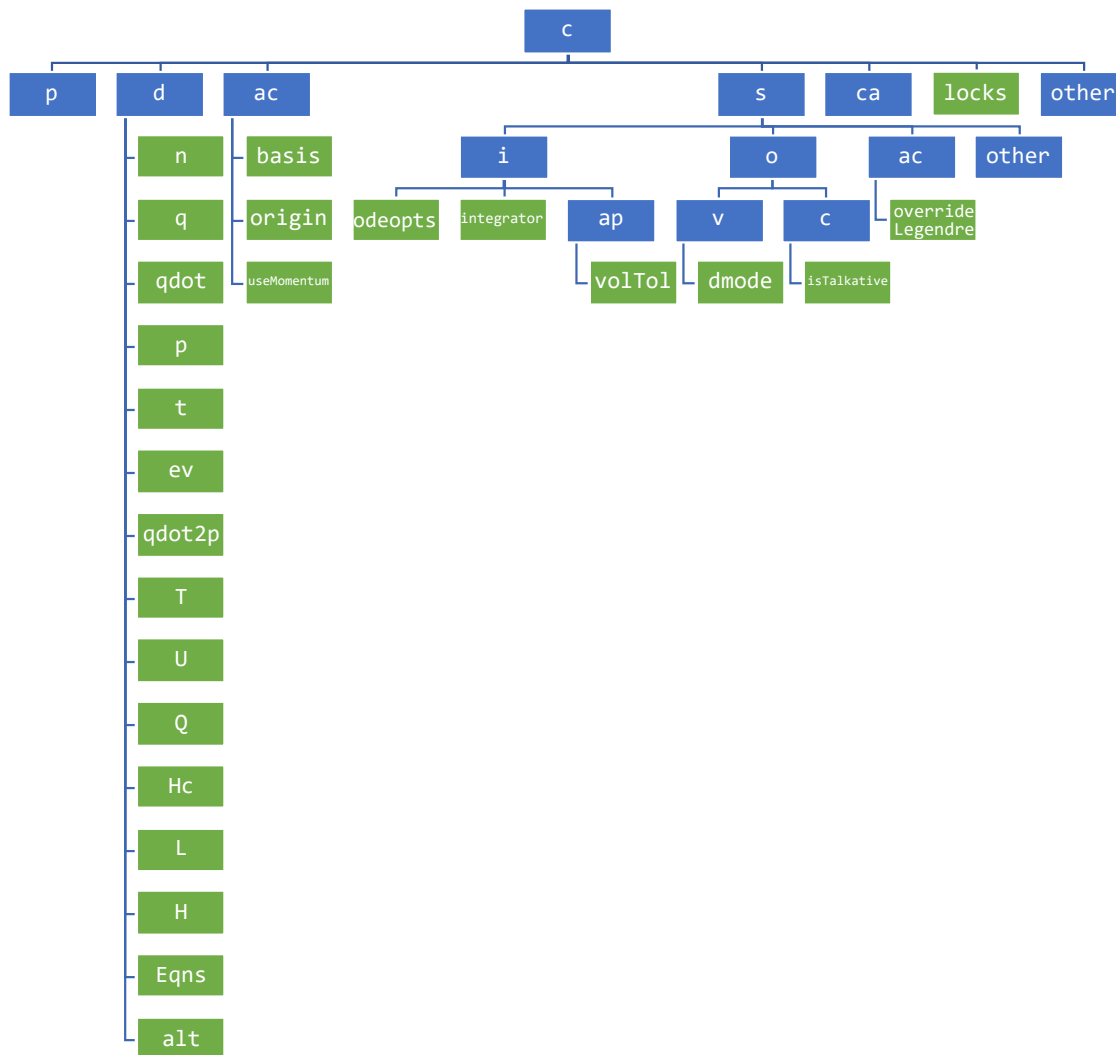


Figure 5.1: The structure of a context object c before it is modified by any other functions. Context objects store data as a series of nested structs, which are usually assigned terse names so that code that accesses context objects can be written more compactly. Blue boxes represent namespaces and green boxes represent properties. Additional namespaces and properties typically need to be added to the context object after creation.

CMDS introduces a design pattern based upon *context objects*, which store required settings, parameters, and other data required for the analysis of a particular Hamiltonian system. A context object is passed by value between various CMDS functions, which may read and/or write from the context object. Thus, code can be written as a series of operations upon the

context object.

A context object is implemented as a nested MATLAB structure (see Figure 5.1). Each context object is comprised of *properties*, structs which contain data, and *namespaces*, structs which can organize properties or other namespaces. Properties consist of two fields: `value`, which contains data, and `transformType`, which specifies how the data transform (as a vector, as a matrix, or not at all) under changes of coordinate system.

The correct way to access data from a context object is to use the getter and setter functions `cg` and `cs`. Users can specify that they prefer to work in an *active coordinate system* by setting the properties of the `ac` namespace of the context object. An active coordinate system can specify new basis vectors and origin location relative to some “standard” coordinate system and that allows users to select between velocity and momentum coordinates. CMDS stores data in the context object using standard coordinates. `cg` retrieves it in the active coordinate system, automatically converting from standard coordinates to active coordinates, whereas `cs` stores it while accounting for the active coordinate system, automatically converting from active coordinates to standard coordinates. This framework is very powerful, because CMDS supports conversion of both numerical and symbolic values. CMDS also has functionality that permits automatic derivation of the function handles for equations of motion, and so users can switch between active coordinate systems and immediately start performing numerical analysis.

5.2.3 Functionality

CMDS can automatically calculate equations of motion, Legendre transformations, and other dynamical properties of systems of interest (see Figure 5.2). CMDS contains functions for numerical integration which automatically translate symbolic equations of motion and energy functions to function handles appropriate for the active coordinate system. The CMDS

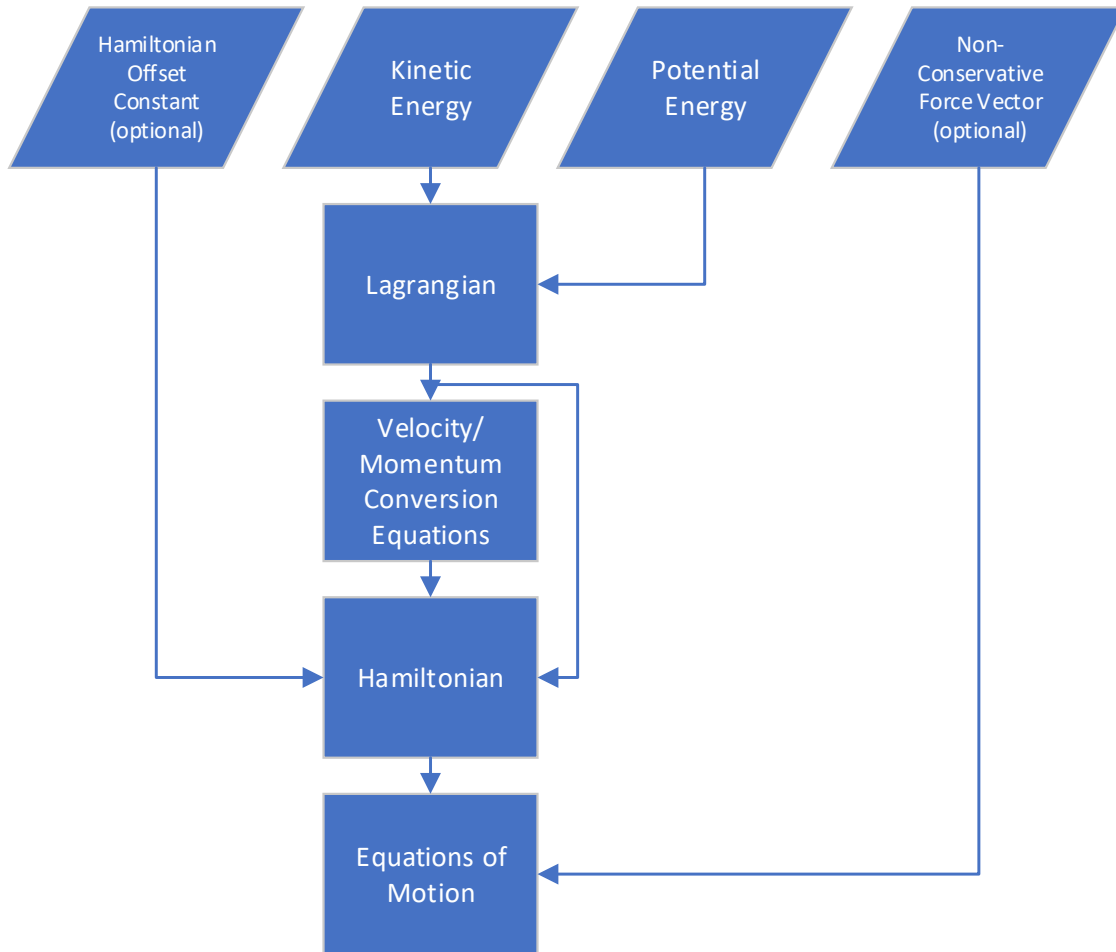


Figure 5.2: The process by which CMDS derives symbolic equations of motion and other useful characteristics of the dynamics from expressions for the kinetic and potential energies. CMDS also supports deriving the equations of motion directly from the Hamiltonian.

numerical integration handler, `integ`, contains functionality for switching between equations of motion while a trajectory is being integrated, and is compatible with any integrator that presents the same interface as the MATLAB `ode113` function, which is its default backend. In addition, there are built-in functions to compute state transition tensors (up to quadratic order), plot or animate a trajectory, and plot the energy over a trajectory.

CMDS ordinarily recomputes the function handles used in numerical integration whenever they are needed, in order to automatically deal with changes of coordinate system or parameter values. However, this process can be slow when many trajectories are being integrated.

CMDS tackles this issue via a caching system that safely “locks” part of the context object from editing while disabling function handle recomputation. This system prevents internal inconsistencies between function handles and the other parts of the context object from emerging that could be extremely confusing to the user.

5.2.4 Examples

CMDS comes with several examples, which are located within the `examples` subfolder of the repository. `examples/harmonic_oscillator` is an introductory example to the MATLAB package that demonstrates a wide variety of useful, basic functions.

`examples/cubic_hamiltonian` tests the quadratic state transition tensor calculator against a simple, analytically verified example. If it functions properly, it should output a computed third order tensor $\Phi^{(2)}$ such that

$$\Phi_{i,a1}(1) \begin{bmatrix} 0 \\ 0 \end{bmatrix} \mathbf{e}_i \otimes \mathbf{e}_a \otimes \mathbf{e}_1 = \begin{bmatrix} 40 & 10 \\ -6 & -40 \end{bmatrix} \quad (5.1)$$

and

$$\Phi_{i,a2}(1) \begin{bmatrix} 0 \\ 0 \end{bmatrix} \mathbf{e}_i \otimes \mathbf{e}_a \otimes \mathbf{e}_2 = \begin{bmatrix} 10 & 48 \\ -40 & -10 \end{bmatrix}. \quad (5.2)$$

`examples/ross_dynamics` demonstrates compatibility with Parallel Computing Toolbox `parfor` loops by integrating and animating a collection of initial conditions.

`examples/uc_harmonic_oscillators_context` is an example of a context object for a two degree-of-freedom system.

5.2.5 Dependencies and compatibilities

CMDS is written in MATLAB and requires the Symbolic Computation Toolbox and the Tensor Toolbox supported by Sandia National Labs [142]. It is compatible with the Parallel Computing Toolbox and the Advanpix Multiprecision Computing Toolbox [125].

5.3 Computing quadratic Hamiltonians for linear symplectic maps

5.3.1 Introduction

In Chapter 2, we stated that the linear symplectic map

$$\Lambda = \begin{bmatrix} \sigma & 0 & 0 & 0 \\ 0 & \sigma^{-1} & 0 & 0 \\ 0 & 0 & \cos \psi & \sin \psi \\ 0 & 0 & -\sin \psi & \cos \psi \end{bmatrix} \quad (5.3)$$

conserves a Hamiltonian function

$$\tilde{H}_2(\mathbf{x}) = \tilde{H}_2(q_1, p_1, q_2, p_2) = \tilde{\lambda}q_1p_1 + \frac{1}{2}\tilde{\nu}(q_2^2 + p_2^2). \quad (5.4)$$

Appendix C proves this assertion by demonstrating that the time- T stroboscopic map of the linear—and therefore analytically solvable—equations of motion associated with (5.4) equals the right hand side of 5.3. However, the creating this proof was only feasible after the form of the correct quadratic Hamiltonian had been fortuitously guessed.

While investigating the properties of the quadratic map (3.23), we discovered a mathematically rigorous technique for computing the subspace of quadratic conserved quantities of a

linear symplectic map; that is, the sets of quadratic multivariate polynomials whose values stay constant when the map is iterated. Our technique, which is described in the current section, could be useful for future geometric analyses of the phase space structure of discrete dynamical systems.

5.3.2 Mathematical preliminaries

Consider a discrete dynamical system $(\mathbb{Z}, \mathbb{R}^{2n}, \mathbf{\Lambda})$ where $\mathbf{\Lambda} \in \text{Sp}(2n, \mathbb{R})$ is an element of the symplectic group $\text{Sp}(2n, \mathbb{R}) \subset \text{GL}(2n, \mathbb{R})$ and $n \in \mathbb{N}$. Let $\mathbf{x} \in \mathbb{R}^{2n}$.

We define a *conserved quantity of $\mathbf{\Lambda}$* as $H : \mathbb{R}^{2n} \rightarrow \mathbb{R}$ where

$$H(\mathbf{\Lambda}(x)) = H(x). \quad (5.5)$$

For the remainder of this analysis, we restrict to $H \in \mathbb{R}_d[\mathbf{x}]$, where $\mathbb{R}_d[\mathbf{x}]$ is the set of polynomials of degree less than or equal to d . This set is a vector space: each element of this space is comprised of a linear combination of all monomials which are in terms of the $2n$ phase space variables and which have degree less than or equal to d [143, 144]. The coefficients of this linear combination are drawn from \mathbb{R} .

For presentational clarity, we use the notation H to refer to a conserved quantity as a function and the notation \vec{H} to refer to a conserved quantity as a vector in $\mathbb{R}_d[\mathbf{x}]$, but either notation refers to the same object. In general, arrows over variable names refer to vectors in $\mathbb{R}_d[\mathbf{x}]$. We also draw a distinction between tensors operating on vectors in \mathbb{R}^{2n} , which are bolded as in \mathbf{X} , versus tensors operating on vectors in $\mathbb{R}_d[\mathbf{x}]$, which are underlined as in \underline{X} .

5.3.3 2D example of method

Consider a one degree-of-freedom system such that

$$\mathbf{x} = \begin{bmatrix} q \\ p \end{bmatrix}.$$

Let

$$\Lambda(\mathbf{x}) = \begin{bmatrix} \Phi_{11} & \Phi_{12} \\ \Phi_{21} & \Phi_{22} \end{bmatrix} \begin{bmatrix} q \\ p \end{bmatrix} = \begin{bmatrix} \Phi_{11}q + \Phi_{12}p \\ \Phi_{21}q + \Phi_{22}p \end{bmatrix}$$

and suppose that the Hamiltonian we seek, which must satisfy

$$H(\Lambda(\mathbf{x})) = H(\mathbf{x}),$$

has the quadratic form $H(\mathbf{x}) = aq + bp + cq^2 + dp^2 + eqp$.

Then

$$H(\Lambda(\mathbf{x})) = a(\Phi_{11}q + \Phi_{12}p) + b(\Phi_{21}q + \Phi_{22}p) + c(\Phi_{11}q + \Phi_{12}p)^2 + d(\Phi_{21}q + \Phi_{22}p)^2 + e(\Phi_{11}q + \Phi_{12}p)(\Phi_{21}q + \Phi_{22}p) \quad (5.6)$$

$$\begin{aligned} &= (a\Phi_{11} + b\Phi_{21})q + (a\Phi_{12} + b\Phi_{22})p + (c\Phi_{11}^2 + d\Phi_{21}^2 + e\Phi_{11}\Phi_{21})q^2 + \\ &(c\Phi_{12}^2 + d\Phi_{22}^2 + e\Phi_{12}\Phi_{22})p^2 + (2c\Phi_{11}\Phi_{12} + 2d\Phi_{21}\Phi_{22} + e\Phi_{11}\Phi_{22} + e\Phi_{12}\Phi_{21})pq. \end{aligned} \quad (5.7)$$

So, we require a, b, c, d, e satisfying the following system of linear equations:

$$\begin{aligned}
a &= a\Phi_{11} + b\Phi_{21} \\
b &= a\Phi_{12} + b\Phi_{22} \\
c &= c\Phi_{11}^2 + d\Phi_{21}^2 + e\Phi_{11}\Phi_{21} \\
d &= c\Phi_{12}^2 + d\Phi_{22}^2 + e\Phi_{12}\Phi_{22} \\
e &= 2c\Phi_{11}\Phi_{12} + 2d\Phi_{21}\Phi_{22} + e\Phi_{11}\Phi_{22} + e\Phi_{12}\Phi_{21}
\end{aligned} \tag{5.8}$$

which can be rewritten, for $\vec{H} = \begin{bmatrix} a & b & c & d & e \end{bmatrix}^T$, as

$$\begin{bmatrix}
\Phi_{11} - 1 & \Phi_{21} & 0 & 0 & 0 \\
\Phi_{12} & \Phi_{22} - 1 & 0 & 0 & 0 \\
0 & 0 & \Phi_{11}^2 - 1 & \Phi_{21}^2 & \Phi_{11}\Phi_{21} \\
0 & 0 & \Phi_{12}^2 & \Phi_{22}^2 - 1 & \Phi_{12}\Phi_{22} \\
0 & 0 & 2\Phi_{11}\Phi_{12} & 2\Phi_{21}\Phi_{22} & \Phi_{11}\Phi_{22} + \Phi_{12}\Phi_{21} - 1
\end{bmatrix} \vec{H} = \vec{0}. \tag{5.9}$$

Let

$$\underline{A} = \begin{bmatrix}
\Phi_{11} & \Phi_{21} & 0 & 0 & 0 \\
\Phi_{12} & \Phi_{22} & 0 & 0 & 0 \\
0 & 0 & \Phi_{11}^2 & \Phi_{21}^2 & \Phi_{11}\Phi_{21} \\
0 & 0 & \Phi_{12}^2 & \Phi_{22}^2 & \Phi_{12}\Phi_{22} \\
0 & 0 & 2\Phi_{11}\Phi_{12} & 2\Phi_{21}\Phi_{22} & \Phi_{11}\Phi_{22} + \Phi_{12}\Phi_{21}
\end{bmatrix}. \tag{5.10}$$

Then, the equation reduces to

$$(\underline{A} - \underline{1})\vec{H} = \vec{0},$$

which can be solved using symbolic or numerical computation software.

5.3.4 Application to the elliptic-hyperbolic map

The linear map (5.3) can be written as

$$\mathbf{\Lambda}(\mathbf{x}) = \begin{bmatrix} \sigma q_1 \\ \sigma^{-1} p_1 \\ \cos \psi q_2 + \sin \psi p_2 \\ -\sin \psi q_2 + \cos \psi p_2 \end{bmatrix}. \quad (5.11)$$

The quadratic Hamiltonian must have the form $H(\mathbf{x}) = aq_1 + bp_1 + cq_2 + dp_2 + eq_1^2 + fp_1^2 + gq_2^2 + hp_2^2 + iq_1p_1 + jq_1q_2 + kq_1p_2 + lp_1q_2 + mp_1p_2 + nq_2p_2$ and so

$$\begin{aligned} H(\mathbf{\Lambda}(\mathbf{x})) &= a\sigma q_1 + b\sigma^{-1} p_1 + c(\cos \psi q_2 + \sin \psi p_2) + d(-\sin \psi q_2 + \cos \psi p_2) + e\sigma^2 q_1^2 + f\sigma^{-2} p_1^2 \\ &\quad + g(\cos \psi q_2 + \sin \psi p_2)^2 + h(-\sin \psi q_2 + \cos \psi p_2)^2 + iq_1 p_1 + j\sigma q_1(\cos \psi q_2 + \sin \psi p_2) \\ &\quad \quad \quad + k\sigma q_1(-\sin \psi q_2 + \cos \psi p_2) + l\sigma^{-1} p_1(\cos \psi q_2 + \sin \psi p_2) \\ &\quad \quad \quad + m\sigma^{-1} p_1(-\sin \psi q_2 + \cos \psi p_2) + n(\cos \psi q_2 + \sin \psi p_2)(-\sin \psi q_2 + \cos \psi p_2) \end{aligned} \quad (5.12)$$

$$\begin{aligned} &= a\sigma q_1 + b\sigma^{-1} p_1 + (c \cos \psi - d \sin \psi)q_2 + (c \sin \psi + d \cos \psi)p_2 + e\sigma^2 q_1^2 + f\sigma^{-2} p_1^2 \\ &\quad + (g \cos^2 \psi + h \sin^2 \psi - n \sin \psi \cos \psi)q_2^2 + (g \sin^2 \psi + h \cos^2 \psi + n \sin \psi \cos \psi)p_2^2 \\ &\quad \quad \quad + iq_1 p_1 + (j\sigma \cos \psi - k\sigma \sin \psi)q_1 q_2 + (j\sigma \sin \psi + k\sigma \cos \psi)q_1 p_2 \\ &\quad \quad \quad + (l\sigma^{-1} \cos \psi - m\sigma^{-1} \sin \psi)p_1 q_2 + (l\sigma^{-1} \sin \psi + m\sigma^{-1} \cos \psi)p_1 p_2 \\ &\quad \quad \quad + (2g \cos \psi \sin \psi - 2h \sin \psi \cos \psi + n \cos^2 \psi - \sin^2 \psi)q_2 p_2 \end{aligned} \quad (5.13)$$

which implies that we must simultaneously solve the equations

$$\begin{aligned}
a &= a\sigma \\
b &= b\sigma^{-1} \\
c &= (c \cos \psi - d \sin \psi) \\
d &= (c \sin \psi + d \cos \psi) \\
e &= e\sigma^2 \\
f &= f\sigma^{-2} \\
g &= (g \cos^2 \psi + h \sin^2 \psi - n \sin \psi \cos \psi) \\
h &= (g \sin^2 \psi + h \cos^2 \psi + n \sin \psi \cos \psi) \\
i &= i \\
j &= (j\sigma \cos \psi - k\sigma \sin \psi) \\
k &= (j\sigma \sin \psi + k\sigma \cos \psi) \\
l &= (l\sigma^{-1} \cos \psi - m\sigma^{-1} \sin \psi) \\
m &= (l\sigma^{-1} \sin \psi + m\sigma^{-1} \cos \psi) \\
n &= (2g \cos \psi \sin \psi - 2h \sin \psi \cos \psi + n \cos^2 \psi - n \sin^2 \psi).
\end{aligned} \tag{5.14}$$

These equations may be written as

$$(\underline{A} - \underline{1})\vec{H} = \vec{0}. \tag{5.15}$$

where

$$\mathbf{A} = \begin{bmatrix}
\sigma & 0 & 0 & 0 & 0 & 0 & 0 & 0 & 0 & 0 & 0 & 0 & 0 & 0 & 0 \\
0 & \sigma^{-1} & 0 & 0 & 0 & 0 & 0 & 0 & 0 & 0 & 0 & 0 & 0 & 0 & 0 \\
0 & 0 & \cos \psi & -\sin \psi & 0 & 0 & 0 & 0 & 0 & 0 & 0 & 0 & 0 & 0 & 0 \\
0 & 0 & \sin \psi & \cos \psi & 0 & 0 & 0 & 0 & 0 & 0 & 0 & 0 & 0 & 0 & 0 \\
0 & 0 & 0 & 0 & \sigma^2 & 0 & 0 & 0 & 0 & 0 & 0 & 0 & 0 & 0 & 0 \\
0 & 0 & 0 & 0 & 0 & \sigma^{-2} & 0 & 0 & 0 & 0 & 0 & 0 & 0 & 0 & 0 \\
0 & 0 & 0 & 0 & 0 & 0 & \cos^2 \psi & \sin^2 \psi & 0 & 0 & 0 & 0 & 0 & 0 & -\sin \psi \cos \psi \\
0 & 0 & 0 & 0 & 0 & 0 & \sin^2 \psi & \cos^2 \psi & 0 & 0 & 0 & 0 & 0 & 0 & \sin \psi \cos \psi \\
0 & 0 & 0 & 0 & 0 & 0 & 0 & 0 & 1 & 0 & 0 & 0 & 0 & 0 & 0 \\
0 & 0 & 0 & 0 & 0 & 0 & 0 & 0 & 0 & \sigma \cos \psi & -\sigma \sin \psi & 0 & 0 & 0 & 0 \\
0 & 0 & 0 & 0 & 0 & 0 & 0 & 0 & 0 & \sigma \sin \psi & \sigma \cos \psi & 0 & 0 & 0 & 0 \\
0 & 0 & 0 & 0 & 0 & 0 & 0 & 0 & 0 & 0 & 0 & \sigma^{-1} \cos \psi & -\sigma^{-1} \sin \psi & 0 & 0 \\
0 & 0 & 0 & 0 & 0 & 0 & 0 & 0 & 0 & 0 & 0 & \sigma^{-1} \sin \psi & \sigma^{-1} \cos \psi & 0 & 0 \\
0 & 0 & 0 & 0 & 0 & 0 & 2 \sin \psi \cos \psi & -2 \sin \psi \cos \psi & 0 & 0 & 0 & 0 & 0 & 0 & (\cos^2 \psi - \sin^2 \psi)
\end{bmatrix} \quad (5.16)$$

With Mathematica, it can be shown that the nullspace corresponding to the solutions of (5.15) is spanned by

$$\left\{ \begin{bmatrix} 0 & 0 & 0 & 0 & 0 & 0 & 0 & 0 & 1 & 0 & 0 & 0 & 0 & 0 & 0 \end{bmatrix}^T, \right. \\
\left. \begin{bmatrix} 0 & 0 & 0 & 0 & 0 & 0 & 1 & 1 & 0 & 0 & 0 & 0 & 0 & 0 & 0 \end{bmatrix}^T \right\} \quad (5.17)$$

which implies that any Hamiltonian of the form

$$H(\mathbf{x}) = c_1 q_1 p_1 + c_2 (q_2^2 + p_2^2)$$

with $c_1, c_2 \in \mathbb{R}$ is conserved.

But we showed in the previous paper that the quadratic Hamiltonian is

$$\tilde{H}_2(\mathbf{x}) = \tilde{\lambda} q_1 p_1 + \frac{1}{2} \tilde{\nu} (q_2^2 + p_2^2) \quad (5.18)$$

with $\tilde{\lambda}, \tilde{\nu} \in \mathbb{R}$. This example shows that the method seems to work as intended.

Chapter 6

Conclusions

6.1 Summary and discussion

This dissertation generalized low-energy transit theory to perturbed models, demonstrated the dynamical geometry creating the arches of chaos, outlined a numerical method for predicting low-energy transit using nonlinear approximations of perturbed models, introduced a MATLAB framework for dynamical systems analysis, and demonstrated a method for automatically calculating conserved quantities of linear symplectic maps.

The chapters explore disparate directions, although Chapter 3 extends Chapter 2. Chapter 1 introduces the classical theory of CR3BP phase space transport, discusses historical applications of the theory to spaceflight, introduces periodically-perturbed models, and discusses recent trends in the literature pertaining to CR3BP manifold dynamics. Chapters 2 and 3 transport low-energy transport theory to contexts with even more delicate dynamics, whereas Chapter 4 concerns the high-energy physics of a model typically applied in a low-energy regime. Chapter 5 discusses material that is foundational to the other three chapters.

A common thread ties all three primary topics together: the application of isomorphism to celestial mechanics. Each topic necessitates transforming the perturbed or unperturbed CR3BP into another system that is isomorphic at least locally. In the first topic, the perturbed CR3BP is discretized via stroboscopic map, which is approximated to first order in sufficiently small neighborhoods of a Lagrange periodic orbit and then transformed into

different coordinates. This simplified eigenbasis map is itself matched with a continuous system generated by a quadratic Hamiltonian.

In the second topic, the unperturbed CR3BP is recast as the equivalent Levi-Civita regularization, which facilitates analysis near the singularities. In addition, the behavior of the arches of chaos is linked with patched conics in the two-body limit.

In the third topic, a very similar series of transformations to that of the first topic is used, except the stroboscopic map is simplified to higher order and the continuous system with simplified Hamiltonian is not found. The linear eigenbasis is still used, for the nonlinear case is treated as a perturbation of the linear case.

6.2 Engineering applications

The work contained in this dissertation is directly applicable for mission planning for a few reasons.

The Lagrange manifold transit theory introduced in Chapter 2 and extended in Chapter 3 is an entirely new paradigm for designing low-energy trajectories. It transfers the predictive geometric power of the unperturbed transport theory to dynamical models which are closer to the full ephemeris. Because low-energy trajectories rely on dynamically delicate phenomena which are disturbed in the full ephemeris, designing trajectories with Lagrange manifolds could reduce stationkeeping costs for low-energy missions and could introduce entirely new trajectories for spacecraft to utilize.

The transit/nontransit discrimination theory described in Chapter 3 could be a useful tool for designing missions that require low energy trajectories based on larger displacements from the Lagrange manifolds. The technique of using an approximate map based on state transition tensors could speed up low-energy mission design tools dramatically by negating the need for full numerical integration yet accounting for nonlinear effects.

Chapter 4 demonstrated a connection between three important concepts: the arches of chaos, the stable and unstable manifolds to the singularities, and patched conics flybys. Being aware of this linkage is very useful for mission design. Consider a rideshare arrangement in which two spacecraft are launching from a single rocket, but one spacecraft is destined for cislunar space and one spacecraft is destined for a heliocentric orbit. Using a plot like Figure 4.9, a trajectory for the rideshare rocket could be designed to follow the stable manifold to the lunar singularity; then, the two spacecraft could use very small impulsive burns to position themselves on either side of the manifold trajectory such that one spacecraft would escape the Earth-Moon system after encounter and one spacecraft would persist within the system. In addition, the rideshare rocket could be fitted with small scientific payloads and repurposed as a lunar impactor, permitting three very different missions to be launched along the same trajectory in an extremely efficient way.

The material in Chapter 5 is very useful for dynamical systems analysis. CMDS automates common tasks, enabling MATLAB code that is faster to write and better-organized. The mathematical method for computing conserved quantities of linear symplectic maps is a foundational result that could be very useful for generalizations of the analysis in Chapter 2 to periodic orbits with other stability types, such as saddle \times spiral sink points.

6.3 Future Work

While this dissertation advances the state of astrodynamical knowledge in several directions, it simultaneously raises many opportunities for further study.

Chapters 2 and 3 introduce Lagrange manifolds as the dynamical objects controlling low-energy phase space transport in perturbed models. However, these chapters only account for the topological transition from Lagrange points to Lagrange periodic orbits, but other types of Lagrange manifolds are theoretically possible; for example, the Lagrange periodic orbits

are themselves expected to bifurcate into tori as additional time-periodic perturbations are added into the system. Thus, more work should be done on analyzing phase space transit structure in cases where Lagrange manifolds possess other topologies.

Chapter 4 demonstrates the connection between the basic structure of the arches of chaos and the singularities of the CR3BP. However, the arches of chaos were also originally presented in an approximation of the full ephemeris [74]. Additional investigation could investigate their nature within the context of higher-fidelity models, like periodically perturbed CR3BP's, in order to solidify the theory.

Chapter 3 introduces a numerical method for using nonlinear approximations to the stroboscopic map to efficiently construct a “diagram” of the predicted transit geometry in the linear eigenbasis. However, further work could investigate the feasibility of using esoteric mathematical methods for analytically describing the transit geometry of these models.

The methodology for computing conserved quantities of linear maps described in Chapter 5 could be generalized to certain classes of nonlinear symplectic maps whose constants of motion would lie in vector spaces of functions other than quadratic polynomials. In addition, the coordinate system conversion functionality built into CMDS could be extended to support rotating and inertial coordinate frames, as well as a variety of other new features.

Bibliography

- [1] Y. Guo and R. W. Farquhar. “New Horizons mission design”. In: *Space Science Reviews* 140 (2008), pp. 49–74.
- [2] C. Kohlhase and P. Penzo. “Voyager mission description”. In: *Space Science Reviews* 21.2 (1977), pp. 77–101.
- [3] W. S. Koon et al. *Dynamical Systems, the Three-Body Problem and Space Mission Design*. Marsden Books, ISBN 978-0-615-24095-4, 2011. ISBN: 978-0-615-24095-4.
- [4] V. Szebehely. *Theory of Orbits: The Restricted Problem of Three Bodies*. New York: Academic, 1967.
- [5] G. Gómez et al. *Dynamics and Mission Design Near Libration Points – Volume 1: Fundamentals: The Case of Collinear Libration Points*. Singapore: World Scientific, 2001.
- [6] K. C. Howell and H. J. Pernicka. “Numerical determination of Lissajous trajectories in the restricted three-body problem”. In: *Celestial mechanics* 41.1-4 (1987), pp. 107–124.
- [7] S. Cuevas del Valle, H. Urrutxua, and P. Solano-López. “Optimal Floquet Station-keeping under the Relative Dynamics of the Three-Body Problem”. In: *Aerospace* 10.5 (2023), p. 393.
- [8] A. Farrés et al. “Geometrical Analysis of Station-Keeping Strategies About Libration Point Orbits”. In: *Journal of Guidance, Control, and Dynamics* 45.6 (2022), pp. 1108–1125.

- [9] A. Jorba and B. Nicolás. “Transport and invariant manifolds near L3 in the Earth-Moon Bicircular model”. In: *Communications in Nonlinear Science and Numerical Simulation* 89 (2020), p. 105327.
- [10] J. Llibre, R. Martínez, and C. Simó. “Tranversality of the invariant manifolds associated to the Lyapunov family of periodic orbits near L2 in the restricted three-body problem”. In: *Journal of Differential Equations* 58.1 (1985), pp. 104–156.
- [11] J. Llibre, R. Martinez, and C. Simó. “Transversality of the invariant manifolds associated to the Lyapunov family of periodic orbits near L2 in the restricted three-body problem”. In: *J. Diff. Eqns.* 58 (1985), pp. 104–156.
- [12] C. D. Murray and S. F. Dermott. *Solar System Dynamics*. Cambridge: Cambridge University Press, 1999.
- [13] T. Greenspan. “Stability of the Lagrange Points, L4 and L5”. PhD thesis. Thesis paper, Cornell University (January 2014), 2014.
- [14] J. Moser. “On the generalization of a theorem of Liapunov”. In: *Comm. Pure Appl. Math.* 11 (1958), pp. 257–271.
- [15] C. C. Conley. “On the ultimate behavior of orbits with respect to an unstable critical point. I. Oscillating, asymptotic, and capture orbits”. In: *J. Differential Equations* 5 (1969), pp. 136–158.
- [16] G. Tsirogiannis, C. Douskos, and E. Perdios. “Computation of the Liapunov orbits in the photogravitational RTBP with oblateness”. In: *Astrophysics and Space Science* 305 (2006), pp. 389–398.
- [17] C. C. Conley. “Low energy transit orbits in the restricted three-body problem”. In: *SIAM J. Appl. Math.* 16 (1968), pp. 732–746.

- [18] A. A. Siddiqi. *Beyond Earth: A chronicle of deep space exploration, 1958-2016*. Vol. 4041. National Aeronautics & Space Administration, 2018.
- [19] R. W. Farquhar et al. “Trajectories and Orbital Maneuvers for the First Libration-Point Satellite”. In: *Journal of Guidance and Control* 3 (1980), pp. 549–554.
- [20] R. W. Farquhar. “The Flight of ISEE-3/ICE: Origins, Mission History, and a Legacy”. In: *The Journal of the Astronautical Sciences* 49 (2001), pp. 23–73.
- [21] L. Burlaga, K. Ogilvie, and W. Feldman. *Interplanetary Physics Laboratory (IPL): A concept for an interplanetary mission in the mid-eighties*. Tech. rep. 1977.
- [22] H. Franz et al. “WIND nominal mission performance and extended mission design”. In: *The Journal of the Astronautical Sciences* 49 (2001), pp. 145–167.
- [23] C. E. Roberts. “Long term missions at the Sun-Earth Libration Point L1: ACE, SOHO, and WIND”. In: *AAS/AIAA Astrodynamics Specialist Conference*. GSFC. CP. 4786.2011. 2011.
- [24] C. Roberts et al. “Early mission maneuver operations for the deep space climate observatory Sun-Earth L1 libration point mission”. In: *AIAA/AAS Astrodynamics Specialist Conference*. GSFC-E-DAA-TN25055. 2015.
- [25] J. Brown and J. Petersen. “Applying dynamical systems theory to optimize libration point orbit stationkeeping maneuvers for WIND”. In: *AIAA/AAS Astrodynamics Specialist Conference*. 2014, p. 4304.
- [26] L. B. Wilson III et al. *A quarter century of wind spacecraft discoveries*. 2021.
- [27] W. S. Koon et al. “Low energy transfer to the Moon”. In: *Celestial Mechanics and Dynamical Astronomy* 81 (2001), pp. 63–73.

- [28] E. A. Belbruno and J. K. Miller. “Sun-perturbed Earth-to-Moon transfers with ballistic capture”. In: *Journal of Guidance, Control and Dynamics* 16 (1993), pp. 770–775.
- [29] W. S. Koon et al. “Shoot the moon”. In: (2000).
- [30] M. Lo et al. “Genesis Mission Design”. In: *The Journal of the Astronautical Sciences* 49 (2001), pp. 169–184.
- [31] W. S. Koon et al. “The Genesis Trajectory and Heteroclinic Connections”. In: *AAS/AIAA Astrodynamics Specialist Conference*. Paper No. AAS 99-451. Girdwood, Alaska, 1999.
- [32] J. Benkhoff et al. “BepiColombo-mission overview and science goals”. In: *Space science reviews* 217.8 (2021), p. 90.
- [33] S. Campagnola and M. Lo. “BepiColombo gravitational capture and the elliptic restricted three-body problem”. In: *PAMM: Proceedings in Applied Mathematics and Mechanics*. Vol. 7. 1. Wiley Online Library. 2007, pp. 1030905–1030906.
- [34] R. Jehn et al. “Low-thrust approach and gravitational capture at Mercury”. In: *18th International Symposium on Space Flight Dynamics*. Vol. 548. 2004, p. 487.
- [35] K. Richon, J. Peterson, and A. Nicholson. “Flight Dynamics Planning and Operations Support for the JWST Mission”. In: *2022 AAS/AIAA Astrodynamics Specialist Conference*. AAS 22-611. 2022.
- [36] E. Kolemen, N. J. Kasdin, and P. Gurfil. “Quasi-Periodic Orbits of the Restricted Three-Body Problem Made Easy”. In: *AIP Conference Proceedings*. Vol. 886. 1. American Institute of Physics. 2007, pp. 68–77.

- [37] W. H. Yu and K. Richon. “Launch window trade analysis for the james webb space telescope”. In: *International Symposium on Space Flight Dynamics*. GSFC-E-DAA-TN14126. 2014.
- [38] J. Cronin, P. Richards, and L. Russell. “Some periodic solutions of a four-body problem”. In: *Icarus* 3 (1964), pp. 423–428.
- [39] C. Simó et al. “The Bicircular Model near the Triangular Libration Points”. In: *From Newton to Chaos*. Ed. by A. E. Roy and B. A. Steves. New York: Plenum Press, 1995, pp. 343–370.
- [40] R. Broucke. “Stability of periodic orbits in the elliptic, restricted three-body problem”. In: *AIAA Journal* 7.6 (1969), pp. 1003–1009.
- [41] J. Zhong and S. D. Ross. “Geometry of escape and transition dynamics in the presence of dissipative and gyroscopic forces in two degree of freedom systems”. In: *Communications in Nonlinear Science and Numerical Simulation* 82 (2020), p. 105033.
- [42] J. Zhong, L. N. Virgin, and S. D. Ross. “A tube dynamics perspective governing stability transitions: An example based on snap-through buckling”. In: *International Journal of Mechanical Sciences* (2017). ISSN: 0020-7403. DOI: <https://doi.org/10.1016/j.ijmecsci.2017.10.040>. URL: <http://www.sciencedirect.com/science/article/pii/S0020740317312596>.
- [43] J. Zhong and S. D. Ross. “Global invariant manifolds delineating transition and escape dynamics in dissipative systems: an application to snap-through buckling”. In: *Nonlinear Dynamics* 104 (2021), pp. 3109–3137.
- [44] J. Zhong, L. N. Virgin, and S. D. Ross. “A tube dynamics perspective governing stability transitions: An example based on snap-through buckling”. In: *International Journal of Mechanical Sciences* 149 (2018), pp. 413–428.

- [45] G. Franzini. “Relative motion dynamics and control in the two-body and in the restricted three-body problems”. In: (2018).
- [46] D. Zuehlke et al. “Relative Motion Models for the Elliptical Restricted Three Body Problem”. In: *Proceedings of the 2022 AAS/AIAA Astrodynamics Specialist Conference, AIAA*. 2022.
- [47] J. J. Rosales, À. Jorba, and M. Jorba-Cuscó. “Families of Halo-like invariant tori around L_2 in the Earth-Moon Bicircular Problem”. In: *Celestial Mechanics and Dynamical Astronomy* 133.4 (2021), p. 16.
- [48] B. Kumar et al. “Investigations of Relations Between Jupiter-Europa and Jupiter-Ganymede Resonant Tori in the Planar Bicircular Restricted 4-Body Problem”. In: (2021).
- [49] B. Kumar, R. L. Anderson, and R. de la Llave. “Rapid and accurate methods for computing whiskered tori and their manifolds in periodically perturbed planar circular restricted 3-body problems”. In: *Celestial Mechanics and Dynamical Astronomy* 134.1 (2022), p. 3.
- [50] B. McCarthy and K. Howell. “Quasi-Periodic Orbits in the Sun-Earth-Moon Bicircular Restricted Four-Body Problem”. In: *31st AAS/AIAA Space Flight Mechanics Meeting, virtual*. 2021.
- [51] E. Castella and À. Jorba. “On the vertical families of two-dimensional tori near the triangular points of the bicircular problem”. In: *Celestial Mechanics and Dynamical Astronomy* 76 (2000), pp. 35–54.
- [52] A. Jorba, M. Jorba-Cuscó, and J. J. Rosales. “The vicinity of the Earth–Moon L_1 point in the bicircular problem”. In: *Celestial Mechanics and Dynamical Astronomy* 132.2 (2020).

- [53] B. Kumar, R. L. Anderson, and R. de la Llave. “Using GPUs and the parameterization method for rapid search and refinement of connections between tori in periodically perturbed planar circular restricted 3-body problems”. In: *arXiv preprint arXiv:2109.14814* (2021).
- [54] A. Jorba and B. Nicolás. “Using invariant manifolds to capture an asteroid near the L3 point of the Earth-Moon Bicircular model”. In: *Communications in Nonlinear Science and Numerical Simulation* 102 (2021), p. 105948.
- [55] J. J. Rosales, À. Jorba, and M. Jorba-Cuscó. “Transfers from the Earth to L 2 Halo orbits in the Earth–Moon bicircular problem”. In: *Celestial Mechanics and Dynamical Astronomy* 133.11-12 (2021), p. 55.
- [56] E. S. Gawlik et al. “Lagrangian coherent structures in the planar elliptic restricted three-body problem”. In: *Celestial Mechanics and Dynamical Astronomy* 103 (2009), pp. 227–249.
- [57] H. Baoyin and C. R. McInnes. “Solar sail equilibria in the elliptical restricted three-body problem”. In: *Journal of Guidance, Control, and Dynamics* 29.3 (2006), pp. 538–543.
- [58] P. Gurfil and D. Meltzer. “Stationkeeping on unstable orbits: generalization to the elliptic restricted three-body problem”. In: *The Journal of the Astronautical Sciences* 54.1 (2006), pp. 29–51.
- [59] M. Delva. “Integration of the elliptic restricted three-body problem with Lie series”. In: *Celestial mechanics* 34.1-4 (1984), pp. 145–154.
- [60] J. F. Palacián et al. “Searching for periodic orbits of the spatial elliptic restricted three-body problem by double averaging”. In: *Physica D: Nonlinear Phenomena* 213.1 (2006), pp. 15–24.

- [61] E. Lakin. “Coordinate systems used to study the elliptic restricted three body problem”. MA thesis. Universitat Politècnica de Catalunya, 2019.
- [62] X. Xu and Y. Fu. “A new class of symmetric periodic solutions of the spatial elliptic restricted three-body problem”. In: *Science in China Series G: Physics, Mechanics and Astronomy* 52.9 (2009), pp. 1404–1413.
- [63] R. I. Paez and M. Guzzo. “On the analytical construction of halo orbits and halo tubes in the elliptic restricted three-body problem”. In: *arXiv preprint arXiv:2203.16315* (2022).
- [64] R. I. Paez and M. Guzzo. “Transits close to the Lagrangian solutions L_1 , L_2 in the elliptic restricted three-body problem”. In: *Nonlinearity* 34.9 (2021), pp. 6417–6449. DOI: [10.1088/1361-6544/ac13be](https://doi.org/10.1088/1361-6544/ac13be).
- [65] A. K. de Almeida Junior and A. F. B. de Almeida Prado. “Comparisons between the circular restricted three-body and bi-circular four body problems for transfers between the two smaller primaries”. In: *Scientific Reports* 12.1 (2022), p. 4148.
- [66] R. Castelli. “On the relation between the bicircular model and the coupled circular restricted three-body problem approximation”. In: *Nonlinear and Complex Dynamics* (2011), pp. 53–68.
- [67] G. Gómez et al. “Connecting orbits and invariant manifolds in the spatial three-body problem”. In: *Nonlinearity* 17 (2004), pp. 1571–1606.
- [68] R. Qi et al. “Earth-to-Moon low energy transfer using time-dependent invariant manifolds”. In: *AIAA/AAS Astrodynamics Specialist Conference*. 2012, p. 4431.
- [69] R. Qi and S. J. Xu. “Applications of lagrangian coherent structures to expression of invariant manifolds in astrodynamics”. In: *Astrophysics and Space Science* 351 (2014), pp. 125–133.

- [70] R. Qi and B. Huang. “Numerical investigation of transport mechanism in four-body problem using Lagrangian coherent structure”. In: *Astrophysics and Space Science* 361 (2016), pp. 1–9.
- [71] C. Circi. “Properties of transit trajectory in the restricted three and four-body problem”. In: *Advances in Space Research* 49.10 (2012), pp. 1506–1519.
- [72] K. Oshima. “Linking low-to high-energy dynamics of invariant manifolds, transit orbits, and singular collision orbits in the planar circular restricted three-body problem”. In: *Celestial Mechanics and Dynamical Astronomy* 131.11 (2019), p. 53.
- [73] R. I. Paez and M. Guzzo. “A study of temporary captures and collisions in the Circular Restricted Three-Body Problem with normalizations of the Levi-Civita Hamiltonian”. In: *International Journal of Non-Linear Mechanics* 120 (2020), p. 103417.
- [74] N. Todorović, D. Wu, and A. J. Rosengren. “The arches of chaos in the Solar System”. In: *Science Advances* 6.48 (2020), eabd1313.
- [75] F. Cardin and M. Guzzo. “Integrability of close encounters in the spatial restricted three-body problem”. In: *Communications in Contemporary Mathematics* 24.06 (2021). DOI: [10.1142/s0219199721500401](https://doi.org/10.1142/s0219199721500401).
- [76] A. Chenciner and J. Llibre. “A note on the existence of invariant punctured tori in the planar circular restricted three-body problem”. In: *Ergodic Theory Dynam. Systems* 8 (1988), pp. 63–72.
- [77] L. Zhao. “Quasi-Periodic Almost-Collision Orbits in the Spatial Three-Body Problem”. In: *Communications on Pure and Applied Mathematics* 68.12 (2015), pp. 2144–2176.

- [78] D. L. Maranhão and J. Llibre. “EJECTION–COLLISION ORBITS AND INVARIANT PUNCTURED TORI IN A RESTRICTED FOUR-BODY PROBLEM”. In: *Celestial Mechanics and Dynamical Astronomy* 71 (1998), pp. 1–14.
- [79] J. Llibre and C. Simó. “Some homoclinic phenomena in the three-body problem”. In: *Journal of Differential Equations* 37.3 (1980), pp. 444–465.
- [80] S. D. Ross. “The interplanetary transport network”. In: *American Scientist* 94 (2006), pp. 230–237.
- [81] S. D. Ross and D. J. Scheeres. “Multiple gravity assists, capture, and escape in the restricted three-body problem”. In: *SIAM Journal on Applied Dynamical Systems* 6.3 (2007), pp. 576–596. DOI: [10.1137/060663374](https://doi.org/10.1137/060663374).
- [82] F. Reddy. “How scientists discovered a solar system “superhighway””. In: *Astronomy* 36 (2008), pp. 38–43.
- [83] F. Topputo. “On optimal two-impulse Earth–Moon transfers in a four-body model”. In: *Celestial Mechanics and Dynamical Astronomy* 117.3 (2013), pp. 279–313.
- [84] K. Oshima and T. Yanao. “Applications of gravity assists in the bi-circular and bi-elliptic restricted four-body problem”. In: *AAS/AIAA Space Flight Mechanics Meeting*. Paper No. AAS 14–234. Santa Fe, New Mexico, 2014.
- [85] K. Onozaki, H. Yoshimura, and S. D. Ross. “Tube dynamics and low energy Earth–Moon transfers in the 4-body system”. In: *Advances in Space Research* 60.10 (2017), pp. 2117–2132.
- [86] Y. Ren and J. Shan. “Numerical study of the three-dimensional transit orbits in the circular restricted three-body problem”. In: *Celestial Mechanics and Dynamical Astronomy* 114.4 (2012), pp. 415–428.

- [87] R. McGehee. “Some homoclinic orbits for the restricted three-body problem”. PhD thesis. University of Wisconsin, Madison, 1969.
- [88] W. S. Koon et al. “Resonance and capture of Jupiter comets”. In: *Celestial Mechanics and Dynamical Astronomy* 81 (2001), pp. 27–38.
- [89] C. Jaffé et al. “Theory of asteroid escape rates”. In: *Physical Review Letters* 89 (2002), p. 011101.
- [90] S. A. Astakhov and D. Farrelly. “Capture and escape in the elliptic restricted three-body problem”. In: *Monthly Notices of the Royal Astronomical Society* 354.4 (2004), pp. 971–979.
- [91] M. Dellnitz et al. “Transport of Mars-crossing asteroids from the quasi-Hilda region”. In: *Physical Review Letters* 94 (2005), p. 231102.
- [92] S. Wiggins. *Introduction to Applied Nonlinear Dynamical Systems and Chaos*. 2nd. Vol. 2. Texts in Applied Mathematics Science. Berlin: Springer-Verlag, 2003.
- [93] J. Guckenheimer and P. Holmes. *Nonlinear oscillations, dynamical systems, and bifurcations of vector fields*. Vol. 42. Springer Science & Business Media, 2013.
- [94] G. Gómez, J. Masdemont, and J. Mondelo. “Dynamical substitutes of the libration points for simplified solar system models”. In: *Libration point orbits and applications*. World Scientific, 2003, pp. 373–397.
- [95] J. Moser. *Stable and Random Motions in Dynamical Systems with Special Emphasis on Celestial Mechanics*. Princeton University Press, 1973.
- [96] G. L. Condon and D. P. Pearson. “The Role of Humans in Libration Point Missions with Specific Application to an Earth-Moon Libration Point Gateway Station”. In: *AAS/AIAA Astrodynamics Specialist Conference*. Paper No. AAS 01-307. Quebec City, Canada, 2001.

- [97] M. W. Lo and S. D. Ross. “The lunar L1 gateway: portal to the stars and beyond”. In: *AIAA Space 2001 Conference and Exposition*. 2001, p. 4768.
- [98] E. M. Alessi, J. Masdemont, and A. Rossi. “The Earth–Moon System As a Dynamical Laboratory”. In: *Frontiers in Astronomy and Space Sciences* 6 (2019), p. 43.
- [99] J. E. Marsden and T. S. Ratiu. *Introduction to Mechanics and Symmetry*. Vol. 17. Texts in Applied Mathematics. New York: Springer-Verlag, 1999.
- [100] D. W. Jordan and P. Smith. *Nonlinear ordinary differential equations: an introduction for scientists and engineers*. Vol. 10. Oxford University Press, 2007.
- [101] A. J. Lichtenberg and M. A. Leiberman. *Regular and Chaotic Dynamics*. 2nd. Vol. 38. Springer, 1992.
- [102] R. P. McGehee. *Some homoclinic orbits for the restricted three-body problem*. The University of Wisconsin-Madison, 1969.
- [103] R. S. MacKay. “Flux over a saddle”. In: *Physics Letters A* 145 (1990), pp. 425–427.
- [104] W. S. Koon et al. “Heteroclinic connections between periodic orbits and resonance transitions in celestial mechanics”. In: *Chaos* 10 (2000), pp. 427–469.
- [105] H. Waalkens and S. Wiggins. “Direct construction of a dividing surface of minimal flux for multi-degree-of-freedom systems that cannot be recrossed”. In: *Journal of Physics A: Mathematical and General* 37.35 (2004), p. L435.
- [106] V. Krajňák and H. Waalkens. “The phase space geometry underlying roaming reaction dynamics”. In: *Journal of Mathematical Chemistry* 56.8 (2018), pp. 2341–2378.
- [107] T. S. Parker and L. O. Chua. *Practical Numerical Algorithms for Chaotic Systems*. New York: Springer-Verlag, 1989.

- [108] V. M. de Oliveira, P. A. Sousa-Silva, and I. L. Caldas. “Order-chaos-order and invariant manifolds in the bounded planar Earth–Moon system”. In: *Celestial Mechanics and Dynamical Astronomy* 132.11 (2020), pp. 1–17.
- [109] B. P. McCarthy and K. C. Howell. “Cislunar Transfer Design Exploiting Periodic and Quasi-Periodic Orbital Structures in the Four-Body Problem”. In: *71st International Astronautical Congress, Virtual*. 2020.
- [110] K. Oshima et al. “Analysis of medium-energy transfers to the Moon”. In: *Celestial Mechanics and Dynamical Astronomy* 127.3 (2017), pp. 285–300.
- [111] N. Assadian and S. H. Pourtakdoust. “Multiobjective genetic optimization of Earth–Moon trajectories in the restricted four-body problem”. In: *Advances in Space Research* 45.3 (2010), pp. 398–409. issn: 0273-1177.
- [112] Q. Guo and H. Lei. “Families of Earth–Moon trajectories with applications to transfers towards Sun–Earth libration point orbits”. In: *Astrophysics and Space Science* 364.3 (2019), pp. 1–9.
- [113] B. L. Bihan et al. “Invariant manifolds of a non-autonomous quasi-bicircular problem computed via the parameterization method”. In: *Nonlinearity* 30.8 (2017), pp. 3040–3075.
- [114] T. Bartsch et al. “Time-dependent transition state theory”. In: *Advances in Chemical Physics*. Ed. by S. A. Rice. Vol. 140. John Wiley & Sons, Inc., 2008, p. 191.
- [115] S. Naik and S. D. Ross. “Geometry of escaping dynamics in nonlinear ship motion”. In: *Communications in Nonlinear Science and Numerical Simulation* 47 (2017), pp. 48–70. issn: 1007-5704.

- [116] W. Wu and L. McCue. “Application of the extended Melnikov’s method for single-degree-of-freedom vessel roll motion”. In: *Ocean Engineering* 35.17-18 (2008), pp. 1739–1746.
- [117] E. J. Doedel et al. “Elemental periodic orbits associated with the libration points in the circular restricted 3-body problem”. In: *International Journal of Bifurcation and Chaos* 17.08 (2007), pp. 2625–2677.
- [118] K. Oshima. “Multiple families of synodic resonant periodic orbits in the bicircular restricted four–body problem”. In: *Advances in Space Research* 70.5 (2022), pp. 1325–1335.
- [119] X.-B. Xu and Y.-Z. Song. “Continuation of some nearly circular symmetric periodic orbits in the elliptic restricted three-body problem”. In: *Astrophysics and Space Science* 368.3 (2023), p. 13.
- [120] J. Fitzgerald and S. D. Ross. “Geometry of transit orbits in the periodically-perturbed restricted three-body problem”. In: *Advances in Space Research* (2022).
- [121] R. S. Park and D. J. Scheeres. “Nonlinear mapping of Gaussian statistics: theory and applications to spacecraft trajectory design”. In: *Journal of guidance, Control, and Dynamics* 29.6 (2006), pp. 1367–1375.
- [122] W. S. Koon et al. “Dynamical systems, the three-body problem and space mission design”. In: *Equadiff 99: (In 2 Volumes)*. World Scientific, 2022, pp. 1167–1181.
- [123] P. Gurfil and D. Meltzer. “Semi-analytical method for calculating the elliptic restricted three-body problem monodromy matrix”. In: *Journal of guidance, control, and dynamics* 30.1 (2007), pp. 266–271.

- [124] S. Ershkov, D. Leshchenko, and A. Rachinskaya. “Semi-analytical findings for rotational trapped motion of satellite in the vicinity of collinear points $\{L_1, L_2\}$ in planar ER3BP”. In: *Archive of Applied Mechanics* 92.10 (2022), pp. 3005–3012.
- [125] M. C. T. for MATLAB 4.9.2.14905. Yokohama, Japan: Advanpix LLC.
- [126] H. Abou-Kandil et al. *Matrix Riccati equations in control and systems theory*. Birkhäuser, 2012.
- [127] L. Markus. “VIII. Quadratic differential equations and non-associative algebra”. In: *Contributions to the Theory of Nonlinear Oscillations* 5 (1960), p. 185.
- [128] J. C. Artes, J. Llibre, and D. Schlomiuk. “The geometry of quadratic differential systems with a weak focus of second order”. In: *International Journal of Bifurcation and Chaos* 16.11 (2006), pp. 3127–3194.
- [129] J. Reyn. *Phase portraits of planar quadratic systems*. Vol. 583. Springer Science & Business Media, 2007.
- [130] S. Creech, J. Guidi, and D. Elburn. “Artemis: An overview of NASA’S activities to return humans to the Moon”. In: *2022 IEEE Aerospace Conference (AERO)*. IEEE. 2022, pp. 1–7.
- [131] S. Bhadauria and C. Frueh. “Optical Observation Regions in Cislunar Space Using the Bi-Circular Restricted Four Body Problem Geometry”. In: (2022).
- [132] J. J. Rosales, À. Jorba, and M. Jorba-Cuscó. “Invariant manifolds near L_1 and L_2 in the quasi-bicircular problem”. In: *Celestial Mechanics and Dynamical Astronomy* 135.2 (2023), p. 15.
- [133] B. P. McCarthy and K. C. Howell. “Four-body cislunar quasi-periodic orbits and their application to ballistic lunar transfer design”. In: *Advances in Space Research* 71.1 (2023), pp. 556–584.

- [134] A. P. Wilmer and R. A. Bettinger. “Lagrangian dynamics and the discovery of cislunar periodic orbits”. In: *Nonlinear Dynamics* 111.1 (2023), pp. 155–178.
- [135] C. Du, O. Starinova, and Y. Liu. “Low-thrust transfer trajectory planning and tracking in the Earth–Moon elliptic restricted three-body problem”. In: *Nonlinear Dynamics* (2023), pp. 1–16.
- [136] W. Wu et al. “Pre-LOI trajectory maneuvers of the CHANG E-2 libration point mission”. In: *Science China Information Sciences* 55.6 (2012), pp. 1249–1258.
- [137] C. Froeschlé, E. Lega, and R. Gonczi. “Fast Lyapunov indicators. Application to asteroidal motion”. In: *Celestial Mechanics and Dynamical Astronomy* 67.1 (1997), pp. 41–62.
- [138] C. Froeschlé, R. Gonczi, and E. Lega. “The fast Lyapunov indicator: a simple tool to detect weak chaos. Application to the structure of the main asteroidal belt”. In: *Planetary and Space Science* 45.7 (1997), pp. 881–886.
- [139] B. Gladman et al. “The exchange of impact ejecta between terrestrial planets”. In: *Science* 271 (1996), pp. 1387–1392.
- [140] M. A. Werner. “Multiple Gravity Assists for Low Energy Transport in the Planar Circular Restricted 3-Body Problem”. PhD thesis. Virginia Tech, 2022.
- [141] J. Llibre. “On the restricted three-body problem when the mass parameter is small”. In: *Celestial Mechanics* 28.1 (1982), pp. 83–105.
- [142] B. W. Bader, T. G. Kolda, et al. *Tensor Toolbox for MATLAB*.
- [143] S. Axler. *Linear algebra done right*. Springer Science & Business Media, 1997.
- [144] P. R. Halmos. *Finite-dimensional vector spaces*. Courier Dover Publications, 2017.

Appendices

Appendix A

GitHub repositories

The MATLAB software frameworks created to generate the results in this dissertation are available at <https://github.com/RossDynamics/CMDS>, <https://github.com/RossDynamics/FILM>, and <https://github.com/RossDynamics/AOCI>.

Appendix B

Initial conditions

In the BCP as described in Section 2.5, the Lagrange periodic orbit replacing the Earth-Moon L_1 point has initial condition,

$$\bar{\mathbf{x}} = \begin{bmatrix} \bar{x} \\ \bar{y} \\ \bar{p}_x \\ \bar{p}_y \end{bmatrix} = \begin{bmatrix} 0.837595408485656 \\ 0 \\ 0 \\ 0.827678389393936 \end{bmatrix}$$

in the four-dimensional position-momentum phase space at phase $\theta = 0$.

In the ER3BP as described in Section 2.6, the Lagrange periodic orbit replacing the Earth-Moon L_1 point has initial condition,

$$\bar{\mathbf{x}} = \begin{bmatrix} \bar{x} \\ \bar{y} \\ \bar{p}_x \\ \bar{p}_y \end{bmatrix} = \begin{bmatrix} 0.792718947200736 \\ 0 \\ 0.000001145970495 \\ 0.886145419995798 \end{bmatrix}$$

in the four-dimensional position-momentum phase space at phase $\theta = 0$. We suspect that $\bar{p}_x \neq 0$ is a numerical artifact.

Appendix C

Proof of Proposition 2.1

Proof. The assumed quadratic Hamiltonian function is,

$$\tilde{H}_2(\mathbf{x}) = \tilde{H}_2(q_1, p_1, q_2, p_2) = \tilde{\lambda}q_1p_1 + \frac{1}{2}\tilde{\nu}(q_2^2 + p_2^2). \quad (\text{C.1})$$

Hamilton's canonical equations generated by this Hamiltonian are linear,

$$\begin{aligned} \dot{\mathbf{x}} = J\nabla\tilde{H}_2(\mathbf{x}) &= \begin{bmatrix} 0 & 1 & 0 & 0 \\ -1 & 0 & 0 & 0 \\ 0 & 0 & 0 & 1 \\ 0 & 0 & -1 & 0 \end{bmatrix} \begin{bmatrix} \tilde{\lambda}p_1 \\ \tilde{\lambda}q_1 \\ \tilde{\nu}q_2 \\ \tilde{\nu}p_2 \end{bmatrix} \\ &= \underbrace{\begin{bmatrix} \tilde{\lambda} & 0 & 0 & 0 \\ 0 & -\tilde{\lambda} & 0 & 0 \\ 0 & 0 & 0 & \tilde{\nu} \\ 0 & 0 & -\tilde{\nu} & 0 \end{bmatrix}}_{\mathbf{A}} \mathbf{x}. \end{aligned} \quad (\text{C.2})$$

which is of the form (2.3) with $\lambda = \tilde{\lambda}$, $\nu = \tilde{\nu}$, where $\mathbf{x} = (q_1, p_1, q_2, p_2)^T$.

It is straightforward to show analytically that the solution to the linear differential

equation (C.2) is,

$$\mathbf{x}(t) = e^{\mathbf{A}t} \mathbf{x}(0) = \begin{bmatrix} e^{\tilde{\lambda}t} & 0 & 0 & 0 \\ 0 & e^{-\tilde{\lambda}t} & 0 & 0 \\ 0 & 0 & \cos(\tilde{\nu}t) & \sin(\tilde{\nu}t) \\ 0 & 0 & -\sin(\tilde{\nu}t) & \cos(\tilde{\nu}t) \end{bmatrix} \mathbf{x}(0), \quad (\text{C.3})$$

$$\text{where } \mathbf{x}(0) = \begin{bmatrix} q_{1_0} \\ p_{1_0} \\ q_{2_0} \\ p_{2_0} \end{bmatrix}.$$

We note that $e^{\mathbf{A}T}$ is of the form $\mathbf{\Lambda}$ from (2.13) with

$$\sigma = e^{\tilde{\lambda}T}, \quad \psi = \tilde{\nu}T, \quad (\text{C.4})$$

which is equivalent to (2.15). Therefore,

$$\mathbf{x}(T) = \mathbf{\Lambda} \mathbf{x}(0) \quad (\text{C.5})$$

And thus $\tilde{H}_2(\mathbf{x})$ generates the linear symplectic map $\mathbf{x} \mapsto \mathbf{\Lambda} \mathbf{x}$, with $\mathbf{\Lambda}$ as in (2.13). \square

Appendix D

Continuation visualization for the ER3BP L_1 Lagrange periodic orbit

The ER3BP L_1 Lagrange periodic orbit can be obtained through continuation using the methodology described in Section 3.4. Let the true eccentricity of the system be e . A rescaled eccentricity is given by $e\epsilon_e$ where $\epsilon_e = 0$ for 0 eccentricity and $\epsilon_e = 1$ for the true eccentricity. Substituting $e\epsilon_e$ into the equations of motion and slowly increasing ϵ_e while refining the Lagrange periodic orbit for each perturbation of the parameter demonstrates continuity between the Lagrange point and the full eccentricity Lagrange periodic orbit (see Figure [D.1](#)).

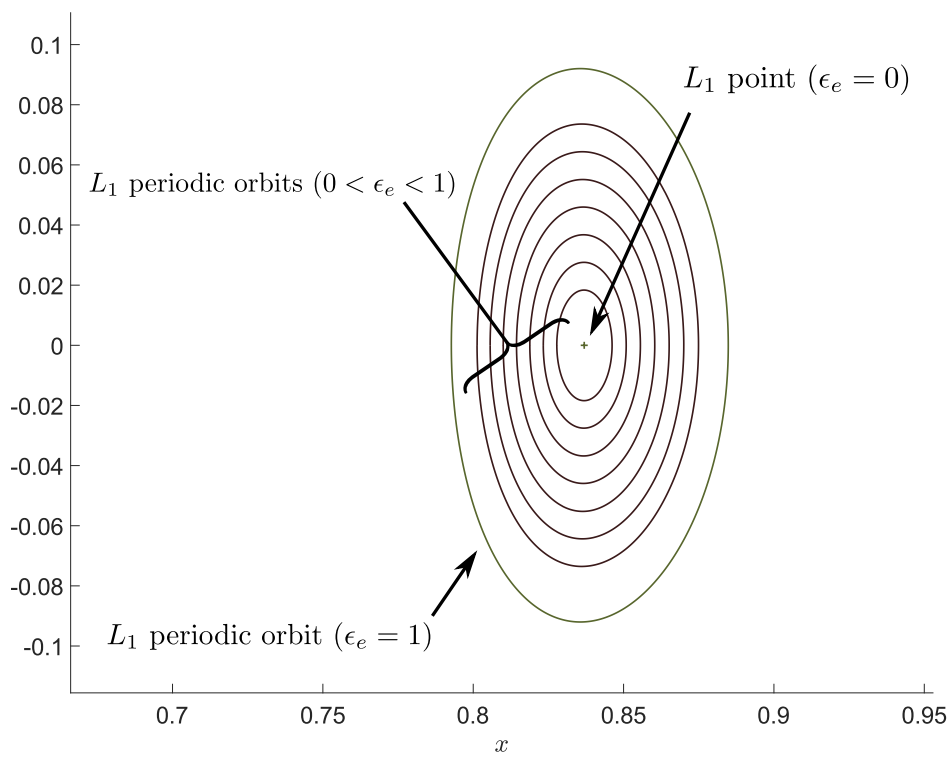


Figure D.1: A family of periodic orbits for different eccentricities emanating from the unperturbed L_1 point in the ER3BP.